



Wave Flume Experiments on Permeable Structures

The effect of arrays of cylinders on wave reflection, dissipation and transmission

S.S. Haage

Wave Flume Experiments on Permeable Structures

The effect of arrays of cylinders on wave reflection, dissipation and transmission

by

S.S. Haage

in partial fulfilment of the requirements for the degree of

Master of Science
in Hydraulic Engineering

at the Delft University of Technology,
to be defended publicly on Wednesday October 31, 2018 at 13:00 PM

Student number: 4268660

Thesis committee:	Ir. A. Gijón Mancheño,	Delft University of Technology, Supervisor
	Ir. E.E. Sirks,	Witteveen + Bos, Supervisor
	Prof. dr. ir. W. S. J. Uijttewaai,	Delft University of Technology, Chairman
	Ing. C. Kuiper,	Delft University of Technology
	Dr. ir. B. Hofland,	Delft University of Technology
	Prof. dr. ir. J.C. Winterwerp,	Delft University of Technology

An electronic version of this thesis is available at <http://repository.tudelft.nl/>.

Cover: Walaba poles intended to trap sediment (Paramaribo, Suriname). Photography by C. Çete.



Acknowledgements

This thesis work concludes the Master of Science program in Hydraulic Engineering at the Delft University of Technology. The research is part of the Building with Nature project *BioManCo* in Indonesia and was conducted at engineering consultancy Witteveen + Bos. The wave flume experiments took place at the Environmental Fluid Mechanics Laboratory at TU Delft.

I would like to express my gratitude towards my thesis committee, Wim Uijttewaalt, Coen Kuiper, Bas Hofland, Alejandra Gijón Mancheño, Emma Sirks and Han Winterwerp. I appreciate your thoughts, critical feedback and helpful advice during our meetings. Special thanks goes out to my daily supervisors Alejandra and Emma. Thank you Alejandra, your patience, support and guidance have done me very well throughout the process. I learned a lot from your profound knowledge on the brushwood structures. Your work ethic is very inspiring and I wish you all the best for the remaining part of your research. Thanks Emma for welcoming me and showing me around at the company. You made me feel like part of the team, as you always involved me in the activities that took place. Also, your precision and critical remarks brought my thesis to a higher level, which I am grateful for.

Furthermore, I wish to thank the lab personnel for helping me with my work in the wave flume. Thanks Sander for your patience and concern about my safety. Staying with me during after office hours and weekends, especially in the hot summer period, is much appreciated. Thanks Pieter for never backing down from the high demands that came with the design of the physical scale model. You always found ways to make it happen. Rob, thank you for facing the challenges with me that came with testing the model. The practical solutions that you thought of were very sharp.

This achievement, of finalising my journey in terms of studying, would not have been possible without the support of my family and friends. I want to thank my parents, Mientje Jhinnoe and Peter Haage, for their unconditional love and support. Sudarshini, Ceylan, Gaby and D'tasha, the journey as an engineering student wouldn't be as much fun without you guys. I will forever miss it. Finally, I would like to thank my zumba girls: Yadira, Atia, Marta, Leonie and Elise. The countless hours of dancing and good times with you have helped me grow in ways I could only dream of.

*Samantha Haage
October, 2018*

Summary

Due to the removal of mangrove forests, coastal zones can suffer from severe erosion. One of the proposed solutions is the construction of permeable structures. This study aims to optimise the design of permeable (brushwood) structures in order to restore the sediment balance and encourage mangrove re-establishment on tropical mud coasts. Preferably wave transmission should be low in order to create a calmer climate behind the structure. In that way sediment is able to settle down, which could lead to a recovery of the mud profile. It is also preferred that reflection by the structure is low. High reflection rates cause scour holes that lead to instability of the structure. Furthermore, scour holes could hinder future mangrove re-establishment. Aiming to achieve low reflection and transmission rates, the dissipation inside the structure has to be as high as possible.

Experiments were conducted in the 40 meter wave flume at the Environmental Fluid Mechanics Laboratory at TU Delft. The permeable structure was schematized as an array of cylinders. With the physical scale model various effects could be tested, including the porosity, structure width, arrangement, orientation, etc. The tests were done for 5 different wave cases, from which the wave energy distribution over reflection, dissipation and transmission was determined.

The existing brushwood structures require intensive maintenance. This is partly due to the sinking of the material into the soft mud. Also, the brushwood material washes away often as it is lighter than water and difficult to constrain in vertical direction. An alternative design that requires less maintenance would be preferred. Therefore, it was interesting to see whether a comparable amount of wave dissipation could be achieved by using vertical elements only. One important finding is that in more shallow water regions, vertical and horizontal orientations have similar dissipation rates. In water regions that go more towards deep water, the horizontal structures have higher dissipation rates. This can be explained by the relative importance of the horizontal and vertical velocities due to the wave motion. In deep water vertical velocities are relatively high. As the horizontal elements have more exposure to this component in comparison to the vertical elements, they provide more dissipation. In shallow water the relative importance of the vertical velocities is lower, which explains the similar dissipation rates of the two orientations.

The analytical model of Dalrymple (1984) was used to describe the energy dissipation through the structures. Drag coefficients were derived by using the calibration method. For $KC < 15$ the drag coefficients start increasing. This is possibly due to the relative importance of the inertia force. Comparing the drag coefficients to the ones derived from direct force and velocity measurements in previous studies showed relative high values. This could be due to an underestimation of the horizontal velocity due to the wave motion. The velocity that is used is the undisturbed velocity in front of the structure. However, the velocity inside the structure might be higher as the flow accelerates in between the gaps of the elements. Furthermore, the wave cases in this research are in the Stokes 2nd and 3rd order region, indicating that the waves cannot be fully described by linear wave theory. The inertia, permeability and non-linear effects among other possible effects are not included in the analytical model of Dalrymple. Therefore, the drag coefficients do not only represent drag forces, but also other processes. To gain more insight on the physical mechanisms that affect the wave energy dissipation, it is recommended to test the same scale model with direct force and velocity measurements.

Contents

Acknowledgements	5
Summary	7
List of Symbols	12
1. Introduction	15
1.1 Problem description	15
1.2 Research goal	20
1.3 Research questions	21
1.4 Research scope	22
1.5 Research approach	22
2. Literature Review	24
2.1 Waves	24
2.1.1 Wave generation and dispersion	24
2.1.2 Definition of deep, intermediate and shallow water regions	26
2.1.3 Wave transformation	27
2.1.4 Wave-induced flow	28
2.1.5 Flow describing parameters	30
2.2 Wave-structure interaction	31
2.2.1 Translation of incoming wave energy into reflection, dissipation and transmission	31
2.2.2 Previous research on wave-structure interaction	32
2.3 Parameterization of wave energy dissipation through permeable structures	35
2.3.1 Wave energy dissipation through granular structures	35
2.3.2 Wave energy dissipation through vegetation	36
3. Set-up of experiments	44
3.1 Description of the set-up	44
3.2 Design of physical scale model	46

3.3 Scaling.....	49
3.3.1 Scaling rules.....	49
3.3.2 Field conditions	50
3.3.3 Scaled conditions.....	52
3.4 Setup of wave gauges.....	55
3.5 Description of configurations	57
4. Results of experiments.....	61
4.1 Data processing.....	61
4.2 Measured reflection, dissipation and transmission.....	62
4.3 Correlation wave dissipation and dimensionless wave parameters.....	63
4.4 Wave dissipation for different configurations.....	66
4.4.1 Porosity effect	66
4.4.2 Effect of spreading out the same number of elements over a larger area.....	68
4.4.3 Effect of arrangement between the elements and width	68
5. Analysis of results.....	73
5.1 Calibrated drag coefficients for different configurations.....	73
5.1.1 Orientation effect (horizontal vs. vertical elements)	74
5.1.2 Porosity effect	77
5.1.3 Arrangement effect	80
5.1.4 Effect of spreading out the same number of elements over a larger area.....	82
5.1.5 Width effect	82
5.2 Comparison drag coefficients with previous studies	86
5.3 Relationship with prototype	89
6. Conclusions and recommendations	93
6.1 Conclusions	93
6.2 Recommendations.....	96
Bibliography	99
Appendix A: Morison's equation and method	103

Appendix B: Wave measurements in Demak	106
Appendix C: Method of Goda and Suzuki	110
Appendix D: Reference sheet wave gauge	113
Appendix E: Tables of Results	116
Appendix F: Results correlation wave dissipation and dimensionless wave parameters	125

List of Symbols

α	Slope angle (°)
a	Amplitude wave (m)
A	The cross-sectional area perpendicular to the flow (m ²)
β_i	Measure for permeability breakwaters (-)
B	Crest width (m)
c_g	Wave group velocity (m/s)
C_d	Drag coefficient (-)
\bar{C}_D	Bulk drag coefficient (-)
C_{diss}	Dissipation coefficient (-)
C_M	Inertia coefficient (-)
C_r	Reflection coefficient (-)
C_t	Transmission coefficient (-)
d	Water depth (m)
D	Cylinder diameter (m)
ξ	Iribarren parameter (-)
E_{diss}	Dissipated wave energy (J/m ²)
E_r	Reflected wave energy (J/m ²)
E_t	Transmitted wave energy (J/m ²)
F_d	Drag force (N)
F_I	Inertia force (N)
Fr	Froude number (-)
g	Gravitational constant (m/s ²)
H	Wave height (m)
H_i	Incoming wave height (m)
H_o	Deep water wave height (m)
H_r	Reflected wave height (m)
H_s	Significant wave height (m)
H_t	Transmitted wave height (m)
k	Wave number (rad/m)
KC	Keulegan Carpenter number (-)
L	Wave length (m)
L_c	Characteristic length scale
L_i	Wave length in intermediate water (m)
L_o	Wave length in deep water (m)
L_{sw}	Wave length in shallow water (m)
n	Porosity
N	Number of elements per unit area (m ⁻²)
μ	Dynamic viscosity (Pa·s)
R_c	Freeboard (m)
Re	Reynolds number (-)
ρ_w	Water density (kg/m ³)
t	Time (s)
T	Wave period (s)
T_p	Peak period (s)

u	Horizontal component orbital velocity (m/s)
\dot{u}	Horizontal component orbital acceleration (m ² /s)
u_f	Filter velocity (m/s)
\hat{u}	Amplitude horizontal component orbital velocity (m/s)
U	Depth averaged horizontal component orbital velocity (m/s)
ν	Kinematic viscosity (m ² /s)
\hat{v}	Amplitude vertical component orbital velocity (m/s)
V	Depth averaged vertical component orbital velocity (m/s)
ω	Angular frequency (rad/s)
w	Width of the structure (m)

1. Introduction

In Section 1.1 the problem description is given. The section starts with a general description of the problem, after which more specifications are given. Some explanations of physical processes and examples from practice at different locations are described as well. The section ends with the conclusion of the literature that is still missing. The main research goal is described in Section 1.2. The main research question with the additional sub questions are formulated in Section 1.3. The main research question is split up into parts with elaborations of the different terms to have a better understanding. In Section 1.4 the research scope is defined. Finally, in Section 1.5 the research approach is given.

1.1 Problem description

Mangrove ecosystems are present at multiple tropical mud coasts all over the world (e.g. Indonesia, Suriname and Vietnam), provided that the biological and physical conditions for establishment are met. Mangrove forests enhance coastal resilience, by both attenuating waves and currents and by trapping sediment, subsequently mitigating erosion. However, in some areas, the size of the mangrove forests is reducing. An impression is shown in Figure 1.1. The reduction could either be caused by enhanced wave action or by human activities.



Figure 1.1 Impression of mangrove that is left at Paramaribo, Suriname (Çete, 2017)

The enhanced wave action, meaning increased wave heights, is caused by periodic absence of foreshores (cheniers or mud banks that propagate along the coast). When the foreshores are absent (and the wave action is enhanced), the number of mangroves decreases as mangroves can only handle a limited amount of wave action. When the foreshores are present again and more wave energy can be dissipated, mangroves start to grow back. Thus, this natural phenomenon does not necessarily have to be a problem. This is, for instance, the case on the Surinamese coast.

Furthermore, there are human activities that cause a decrease in the number of mangroves. The human activities include the removal of mangroves for purposes as fishery. Also, land subsidence for farming purposes contributes to the decrease. Changing the human activities is a quite a challenging task as coastal protection is not always a top priority in some countries. Therefore, there is a lack in awareness about the function of mangroves and coastal protection in general. An example of what could happen due this lack in awareness is the application of impermeable structures (e.g. vertical concrete wall). However, applying impermeable structures makes the coastal erosion problem worse. This is because of two reasons. The first one is that the input of sediment is blocked which means that there is no or small sediment input towards the coast and that mangroves can no longer trap it. The second reason is that wave action is enhanced even further. This is because the impermeable structures cause reflection. When waves are reflected, they interact with new incoming waves, which results in higher waves. These higher waves have larger orbital velocities at the bottom, which cause scour in front of the structure, increasing the water depth. The larger water depth results in even higher waves that are able to reach the same location. These higher waves cause more sediment output. An example of an application of an impermeable structure is shown in Figure 1.2. The structure has stability issues, as scour holes developed in front of it.



Figure 1.2 Example of failure of impermeable structure on mud coast Paramaribo, Suriname

The loss of mangrove vegetation and the application of impermeable structures cause a disruption in the sediment balance, shown in Figure 1.3. The figure also shows that big waves stir up fine sediment from the bed, the tide brings the sediment towards the coast and big and small waves erode the coast. When there is less sediment transport towards the coast (caused by tidal filling) or more erosion (caused by waves), the coast retreats. This changes the mud flat profile from convex to concave, which is illustrated in Figure 1.4.



Figure 1.3 Sediment balance mangrove-mud coastline (Winterwerp, 2014)

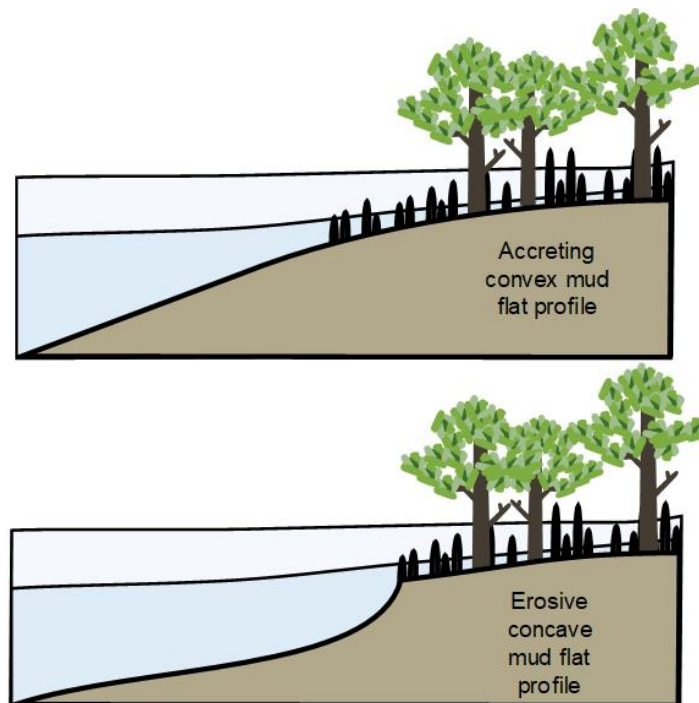


Figure 1.4 Mud profile change from convex to concave (Gijón Mancheño, 2017)

A disruption in the sediment balance of mud coasts is a problem in many tropical places in the world. In an attempt to restore the sediment balance (and therefore allow for mangrove development), permeable structures have been applied in places such as Demak (Indonesia), Paramaribo (Suriname) and the Mekong Delta (Vietnam). The structures emulate the function of mangrove roots as they also attenuate waves and currents (shown in Figure 1.5). Since they are permeable, water can penetrate through them, which reduces the amount of reflection in front of the structure in comparison to the case with impermeable structures. This is favourable for the mitigation of scour holes as scour would cause instability of the structure leading to more regular maintenance. Furthermore scour in front of the structure would hinder mangrove forest expansion in future stages of colonization, as the water depth would be too large for new mangroves to establish.

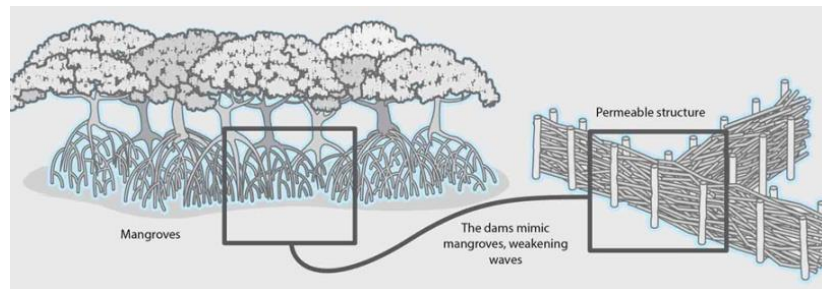


Figure 1.5 Permeable structure and its function (Smith, 2016)

Looking at a larger (structural) scale, there are openings in between the permeable structures, which is shown in Figure 1.6. It is very likely that most of the sediment is transported through these openings rather than through the structure. This is because the tidal currents (which transport sediment) tend to deflect and go along the structure, rather than through it, as the currents prefer the path of less resistance.



Figure 1.6 Openings between permeable structures in Demak, Indonesia (Nanang Sujana, n.d.)

As the permeable structures attenuate waves, a calmer wave climate is created behind the structure. The tide can now bring in sediment (through the openings) and because of the calmer wave climate behind the structure, the sediment is able to settle down. This can lead to a recovery of the mud profile, which is illustrated in Figure 1.7.

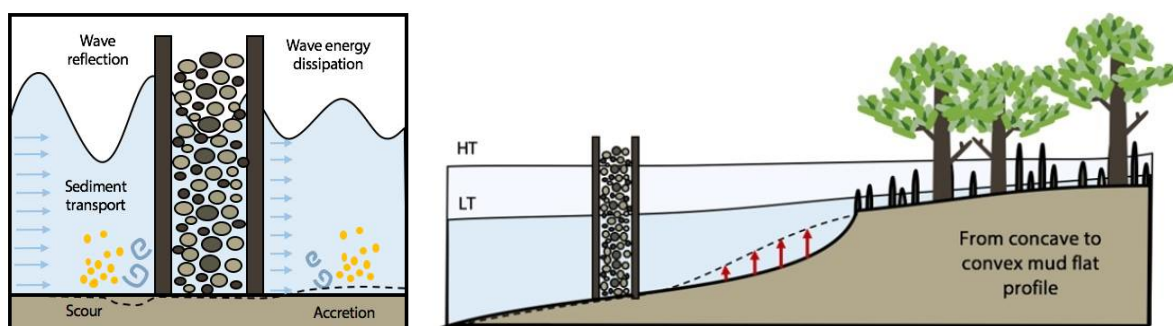


Figure 1.7 Permeable structure and mud profile recovery (Gijón Mancheño, 2017)

Permeable structures have been applied successfully in various parts of the world. Demak (Indonesia) is one example. The structures are shown in Figures 1.8 (a) and (b). A first pilot was carried out in 2013. The structures attenuated waves, favouring sedimentation behind them and providing the physical conditions for mangroves to grow. Up to 0.5 m of sedimentation was measured and natural recruitment of *Avicennia Marina* was observed. In 2015 a large-scale project started with a consortium of Dutch companies (including Witteveen + Bos) in cooperation with the Indonesian Ministry of Marine Affairs and Fisheries. The purpose of the project is to protect 20 km of coastline by a buffering mangrove belt.



Figure 1.8 (a) Close up brushwood structure in Demak (Gijón Mancheño, 2017) (b) Overview brushwood structure in Demak (Gijón Mancheño, 2017)



Figure 1.9 (a) Overview PVC poles in Demak (Gijón Mancheño, 2017) (b) Close up PVC poles with concrete filling inside (Gijón Mancheño, 2017)

During the project several problems have been encountered. The horizontal fill material of the structures (usually brushwood) often requires regular maintenance. This is partly due to the sinking of the fill material into the soft mud. Also, the fill material washes away often as it is lighter than water and difficult to constrain in vertical direction. Because of these problems, PVC poles without horizontal fill material have been applied in a later stage in the project in Demak. At some locations there are also poles with horizontal brushwood filling and at other locations extra bamboo structures have been applied to ensure stability. This is shown in Figures 1.9(a) and (b).

Different configurations have been applied in the field: vertical poles with and without horizontal filling. However, their designs are based on engineering judgement as there are no specific design rules. The relationship between the design parameters of the brushwood structures and their hydrodynamic performance (reflection and dissipation of waves) has not been studied in detail yet.

Literature exists on the parameterization of wave dissipation through granular breakwater structures and through arrays of vertical cylinders. Between these types of structures and the brushwood structures there are some differences such as geometry, orientation and material. Due to these differences the flow is affected differently. The existing literature can therefore not directly be linked to the performance of brushwood structures.

Mai et. al. (1999), Sayah (2006) and Lucas (2017) have studied wave transformation through brushwood structures before by doing physical scale model tests. As in the field, brushwood structures with high densities have been used. In order to improve the hydrodynamic performance (lower reflection and higher dissipation) it might be better to use models with lower densities. Furthermore, the physical processes that dissipate the wave energy have not been identified yet and therefore the parameterization of the dissipation is still missing.

Moreover, it is preferable that only vertical elements are used in practice, as the brushwood material requires intensive maintenance. More research is therefore needed to see whether it is possible to achieve a comparable amount of wave dissipation by using vertical elements only.

1.2 Research goal

The main goal of this research is to determine the effect of different design parameters of brushwood structures on the wave energy balance (reflection, dissipation and transmission) for different wave cases.

This research is part of a larger research: the BioManCO (bio-morphodynamic modelling of mangrove-mud coasts) project. The larger research aims to expand the scientific knowledge on mud-mangrove coastlines and develop a bio-morphodynamic landscape model that can be used to plan future restoration efforts. Three PhD students combine their efforts to develop this tool. Alejandra Gijón Mancheño, focuses on the parameterization of the physical processes occurring at a scale smaller than the grid resolution, of the order of tens of meters. This includes the effect of the brushwood structures on the morphodynamics and the flow-structure interaction at the scale of mangrove trees. The results obtained in this master thesis contribute to the latter part, as they can be used to provide a basis for the understanding of the physical processes that dissipate the waves. The ecologic aspects are studied by Celine van Bijsterveldt. The physical and biologic processes will be combined in a large scale model by Silke Tas.

1.3 Research questions

The main research question is:

*In what manner do **different design parameters** of brushwood structures affect the **wave energy balance** (reflection, dissipation and transmission) for **different wave cases**?*

Different design parameters

Examples are: orientation (horizontal and vertical elements), arrangement of elements, structure width, porosity, etc.

Wave energy balance

Incoming wave energy is translated into reflection, dissipation and transmission. Preferably reflection and transmission rates are low, following that high dissipation rates inside the structure are aimed for.

Different wave cases

The wave energy balance (reflection, dissipation, transmission) depends not only on the design parameters of the brushwood structure but also on the characteristics of the incoming waves. Therefore, different combinations of these are looked at.

Additionally, the following sub questions have been formulated:

- How representative are existing analytical models for the wave dissipation through the structures?
- What recommendations can be made for the practical design of brushwood structures?

1.4 Research scope

A simplified test case is used, which focusses on specific components relevant for the research questions. The occurring differences between reality and the simplified test case are addressed in Table 1.1. Furthermore, the wave cases are based on the wave conditions in Demak, Indonesia.

Table 1.1 Differences between reality and simplified test case

Reality	Simplified Test Case
Complex geometry of brushwood structures	Array of cylinders
Random placement of brushwood branches	Controlled placement of cylinders
Overtopping	No overtopping
Underflow	No underflow
Sediment	No sediment
No horizontal bottom	Horizontal bottom
Currents and waves	Waves only
Irregular waves with a spectrum and random direction	Regular waves
Large scale 3D effects (longshore currents, diffraction)	Wave flume with limited width
High Reynolds numbers	Laboratory scale with lower Reynolds numbers
Air entrainment	No air entrainment
Low surface tension	High surface tension
Waves break before structure	No wave breaking

1.5 Research approach

To have a better understanding of the brushwood structure and its effect on the wave energy balance, laboratory experiments are performed. This includes tests with a physical scale model of the brushwood structure in a wave flume. In these tests different structural design parameters and their effect on the wave energy balance are tested. The tests are performed for different wave cases.

For all the different structural parameters the horizontal and vertical orientation are tested. This is done for two reasons. One is to see whether it is possible to achieve a comparable amount of wave dissipation with the vertical elements as with the horizontal elements. The second reason is that the results of the vertical elements can be linked to existing literature on wave dissipation through vegetation, which is also modelled as an array of vertical cylinders.

Furthermore, the results provide a basis for the understanding of the physical processes that dissipate the wave energy and the parameterization of this. Moreover, an attempt is made to improve the hydrodynamic performance (lower reflection and higher dissipation) of the structures which recommendations for practical design are based upon.

2. Literature review

The present chapter provides an overview of the existing literature about wave hydrodynamics and its interaction with permeable structures. Basic theory on waves is presented first. As the brushwood structures are located near the coast, theory about different water regions (deep, intermediate and shallow) and wave transformation is presented. Furthermore, theory on flow induced by the wave motion is described, followed by dimensionless parameters that describe the wave-induced flow. These parameters allow scaling of the field conditions to the flume scale. Thereafter, a simplified description of wave-structure interaction is given. This section also includes previous research regarding this topic. In the final section formulations for wave dissipation through permeable structures are explained, including wave dissipation through granular structures and through vegetation schematized as an array of vertical cylinders.

2.1 Waves

2.1.1 Wave generation and dispersion

The following explanations are taken from Bosboom and Stive (2015) and are slightly altered for the purpose of this report. Waves are generated by local wind fields, which are schematized in Figure 2.1. The waves have a certain wave height, period and propagation direction, which are the wave characteristics. The wave characteristics are a function of the wind field, the fetch and the local water depth. The wind field includes the speed, duration and direction. The fetch is the maximum length of open water over which the wind blows, which is determined by meteorological and geographical conditions. It generally holds that the higher the wind speed and duration, the larger the wave height and period.

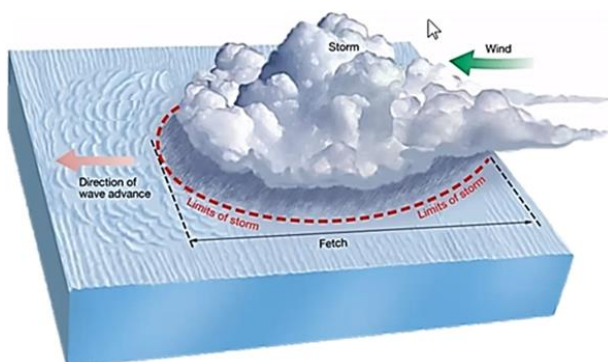


Figure 2.1 Wave generation in offshore water (Meldahl, 2011)

Wave fields disperse (spread out) since the different harmonic components travel at different speeds that depend on their frequency, which is referred to as the frequency dispersion. The dispersion relation for waves is given by:

$$\omega^2 = gk \tanh(kd) \quad [2.1]$$

or

$$L = \frac{g}{2\pi} T^2 \tanh\left(2\pi \frac{d}{L}\right) \quad [2.2]$$

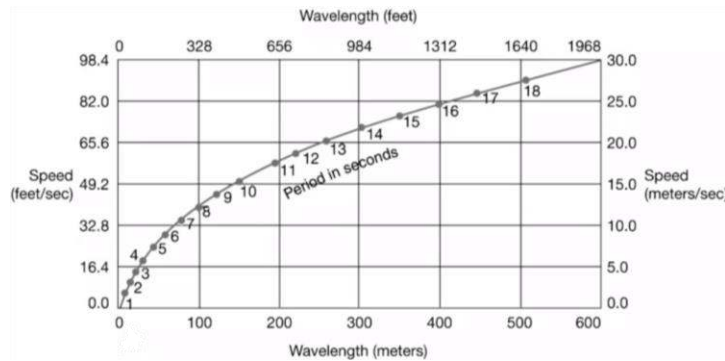


Figure 2.2 Wave length vs. wave propagation speed (Meldahl, 2011)

From the dispersion relation an example plot of wave propagation speed against the wave length is made, which can be seen in Figure 2.2. It becomes clear that longer waves travel faster than shorter waves. Looking from a coastal perspective, which is at a certain distance from the storm center, one would experience long travelling waves first. At a later stage the increasingly shorter waves appear. At long distances from the storm centre, the shorter waves are filtered out. This is because dissipation processes (due to currents, white-capping) more strongly affect the shorter waves. Therefore, only long and (fairly) regular swell waves remain. Furthermore, the swell waves are uni-directional crested because only waves travelling in a certain direction end up at a certain location away from the storm centre. The spreading due to different directions of propagation is called direction dispersion.

The spectrum of swell waves is narrow in both frequency and direction due to frequency and direction dispersion respectively. The swell waves are relatively low as a result of spreading and energy dissipation. Some coasts around the world experience mainly swell waves as storms are generated at a location far away. An example is the Australian coast. At other coasts storms are generated more locally and these wind-sea waves can dominate the wave climate. This is, for instance, the case for the Dutch coast. The waves are irregular and short crested. Most of the times, wave records of the Dutch coast show both swell waves as generated in distant storms and storm waves locally generated. Two distinct peaks can then be observed in the spectrum, as shown in Figure 2.3.

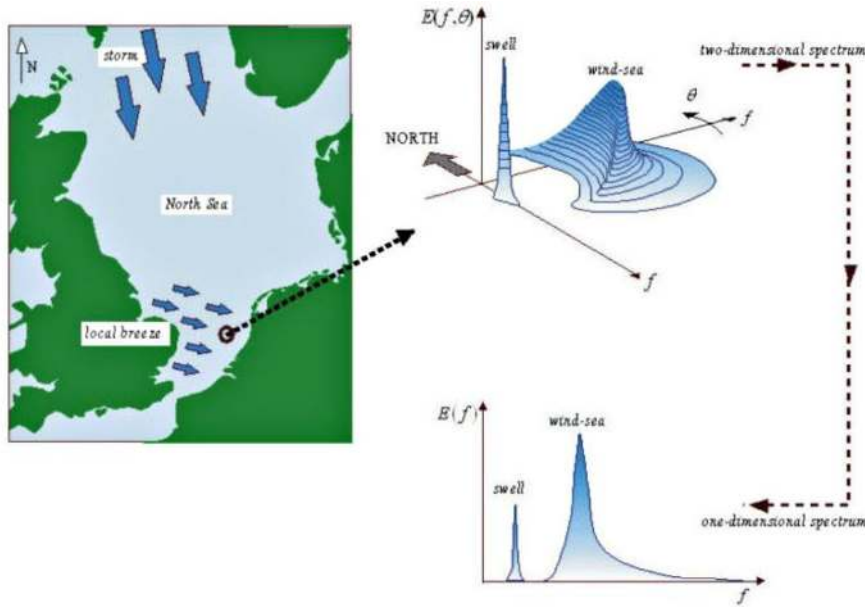


Figure 2.3 A wave spectrum of the Dutch coast (Holthuijsen, 2007)

2.1.2 Definition of deep, intermediate and shallow water regions

Waves propagate from their generation region to the region near the coast (nearshore region). The area of wave generation is usually located in deep water. The nearshore region is usually in shallow water. In between deep water and shallow water, there are intermediate water depths. The limits of these regions depend on the wave length and water depth. They are defined as follows (Ippen 1966):

For deep water:	$\frac{d}{L} > 0.5$
For intermediate water:	$0.05 < \frac{d}{L} < 0.5$
For shallow water:	$\frac{d}{L} < 0.05$

In terms of the wave number k , the different water regions are defined as follows:

For deep water:	$kd \gg 1$
For intermediate water:	$kd \approx O(1)$
For shallow water:	$kd \ll 1$

Using these definitions, the dispersion relation (Equation 2.2) can be simplified for deep water and shallow water cases:

For deep water:	$L_0 = \frac{gT^2}{2\pi}$
For intermediate water:	$L_i = \frac{g}{2\pi} T^2 \tanh(2\pi \frac{d}{L_i})$
For shallow water:	$L_{sw} = \sqrt{gd}T$

An overview of the different water regions is shown in Figure 2.4.

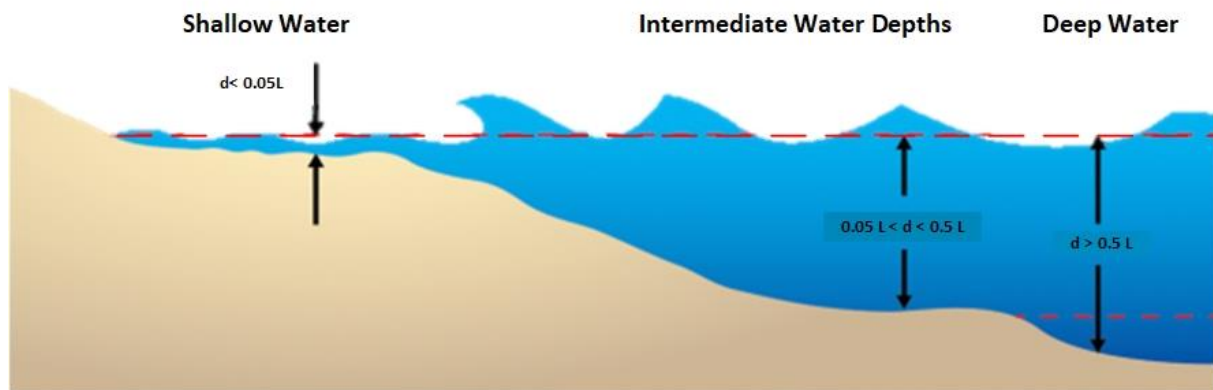


Figure 2.4 Overview different water regions. Adapted from: (Inouye, n.d.).

2.1.3 Wave transformation

When waves leave their area of generation and approach the coastal area, they are affected by the bottom and therefore transform. Different processes occur such as refraction, shoaling and wave-breaking. The latter could also occur in deep water due to the steepness limit of waves. If waves meet abrupt changes in the coastline such as a structure, diffraction occurs. These phenomena are explained further by using the definitions taken from Holthuijsen (2007).

Refraction is the turning of waves towards shallower water due to depth- or current induced changes in the phase speed along the wave crest.

Shoaling is the variation of waves in their direction of propagation due to depth-induced changes of the group velocity in that direction. When waves approach the shore, the wave celerity is reduced. The wave height increases in order to conserve the energy. Wave shoaling causes the wave height to increase to infinity in very shallow water. However, there is a physical limit due to the steepness of the waves (H/L). When this limit is exceeded, the *wave breaks* and dissipates its energy. Steepness limits of wave breaking are defined as follows:

For deep water: $\frac{H_0}{L_0} > 0.142$ (Michell, 1893)

For intermediate water: $\frac{H_0}{L_0} > \tanh\left(\frac{2\pi d}{L_i}\right)$ (Miche, 1944)

In shallow water, wave breaking can also occur due to depth-limitations. When the wave height becomes larger than a certain fraction of the water depth, waves start to break. This fraction is between 0.78 (for solitary wave theory) and 0.88 (for Stokes wave theory).

Diffraction is wave transformation due to sheltering by obstacles such as breakwaters.

2.1.4 Wave-induced flow

The following explanations are taken from Bosboom and Stive (2015) and are slightly altered for the purpose of this report. The waves generate an orbital motion underneath the wave surface, which is shown in Figure 2.5. In deep water the orbits are circular and in shallow water the orbits transform to an elliptical shape. The orbital velocity has a horizontal component u and a vertical component v . Looking at the vertical distribution, the vertical motion diminishes towards the bottom, while the horizontal motion remains (almost) constant. The two components of the orbital velocity for intermediate water are given as follows:

$$u(z, t) = \omega a \frac{\cosh k(z+d)}{\sinh kd} \cos(\omega t) \quad [2.3a]$$

$$v(z, t) = \omega a \frac{\sinh k(z+d)}{\sinh kd} \sin(\omega t) \quad [2.3b]$$

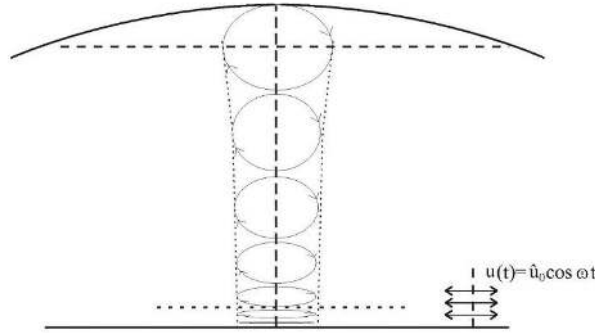


Figure 2.5 Water particle movement in intermediate to shallow water depth (Bosboom & Stive, 2015)

The amplitudes of the two velocity components are defined as follows:

$$\hat{u}(z) = \omega a \frac{\cosh k(z+d)}{\sinh kd} = \frac{2\pi}{T} \frac{H}{2} \frac{\cosh k(z+d)}{\sinh kd} \quad [2.4a]$$

$$\hat{v}(z) = \omega a \frac{\sinh k(z+d)}{\sinh kd} = \frac{2\pi}{T} \frac{H}{2} \frac{\sinh k(z+d)}{\sinh kd} \quad [2.4b]$$

A schematic drawing of the vertical profiles of the velocity amplitude \hat{u} is shown in Figure 2.6.

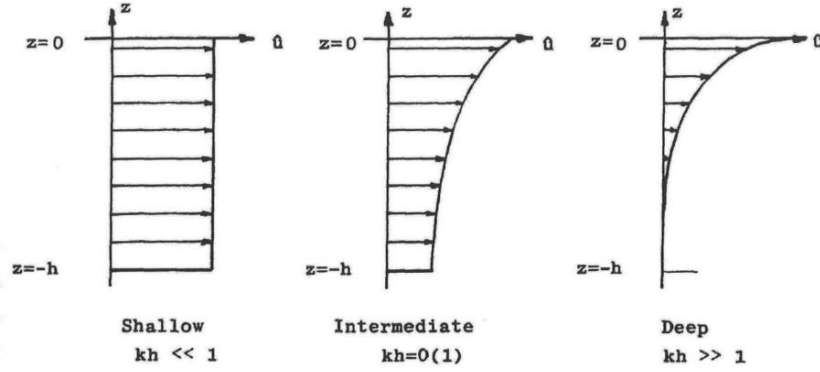


Figure 2.6 Vertical velocity profiles of velocity amplitude \hat{u} for three water regions (Battjes, 2006)

To be able to compute the depth averaged velocity amplitude \hat{u} , Equation 2.4a is first integrated over the water depth. The integration is performed for the part that depends on z , which is shown in Equation 2.5a. Thereafter, Equation 2.5a is multiplied by the remaining term in Equation 2.4a that is independent of z . The latter outcome is finally divided by the water depth, which is shown in Equation 2.6a. The same method is applied for the vertical component of the orbital motion, which is shown in Equations 2.5b and 2.6b.

$$\xi_1 = \int_{z=-d}^{z=0} \cosh k(z+d) \quad [2.5a]$$

$$\xi_2 = \int_{z=-d}^{z=0} \sinh k(z+d) \quad [2.5b]$$

$$U = \left(\frac{2\pi H}{T} \frac{1}{2 \sinh kd} \right) \frac{\xi_1}{d} \quad [2.6a]$$

$$V = \left(\frac{2\pi H}{T} \frac{1}{2 \sinh kd} \right) \frac{\xi_2}{d} \quad [2.6b]$$

2.1.5 Flow describing parameters

The wave-induced flow can be characterized by several dimensionless parameters. These include the Reynolds number, the Froude number and the Keulegan Carpenter number. Each of these parameters is further elaborated in this section.

The Reynolds number (Re) is a parameter which can be used to determine whether a flow is turbulent or laminar. It is the ratio of the inertial forces to the viscous forces of a fluid and is given by:

$$Re = \frac{\rho u L_c}{\mu} = \frac{u L_c}{\nu} \quad [2.7]$$

For low values of Re the flow is considered laminar and for high values it is considered turbulent. The transition point between laminar flow and turbulent flow is different for every geometry. For an isolated cylinder in uniform flow, the flow becomes turbulent when Re has a value higher than ~ 200 (Williamson, 1992). Within a cylinder array the flow becomes turbulent when Re has a value higher than $\sim 150-200$. This only holds for a certain density (ad) of cylinders, which is defined as the volume of the cylinders divided by the total volume. In this case, the density is equal to 0.008-0.07 (Nepf et al., 1997). However, as the array density decreases to zero ($ad \rightarrow 0$), the critical Re value returns to the value of an isolated cylinder (Nepf, 1999).

Another parameter that describes the flow is the Froude number (Fr), which describes the behaviour of the surface of a fluid. It is the ratio of the inertial forces to the gravity forces given by:

$$Fr = \frac{u}{\sqrt{gd}} \quad [2.8]$$

When Fr is equal to 1, the flow is called critical. However, a value of Fr exactly equal to 1 is rarely the case in reality. When Fr is larger than 1, the flow is called supercritical. This implies that the flow velocity is larger than the wave celerity. Therefore, downstream flow disturbances do not affect the upstream flow situation. When Fr is smaller than 1, the flow is called subcritical. This implies that the flow velocity is smaller than the wave celerity. In this case, downstream disturbances in the flow do affect the flow in the upstream situation.

The next dimensionless parameter is the Keulegan Carpenter number (KC). This parameter describes the importance of the drag forces relative to the inertia forces for objects in an oscillatory flow. The Keulegan Carpenter number is given by:

$$KC = \frac{uT}{L} \quad [2.9]$$

Small KC numbers (<10) suggest that inertia dominates, while large KC numbers ($>15-20$) suggest that drag forces are more important (Ozeren et al., 2014).

The dimensionless parameters that describe the wave-induced flow allow scaling field conditions to the flume scale. The scaling rules and application of these are explained in more detail in the set-up of the experiments in Section 3.3.

2.2 Wave-structure interaction

2.2.1 Translation of incoming wave energy into reflection, dissipation and transmission

The wave interaction with a structure is elaborated through the next simplified example, which is illustrated in Figure 2.7. When an incoming wave with wave energy E_i is approaching a permeable structure, the energy is translated into reflection, dissipation and transmission. The wave energy balance is described as follows (Thornton and Calhoun, 1972):

$$E_i = E_r + E_{diss} + E_t \quad [2.10]$$

From linear wave theory it can be stated that the wave energy is proportional to the wave height squared:

$$E = \frac{1}{8} \rho_w g H^2 \quad [2.11]$$

With ρ_w and g remaining constant, the translation from the incoming wave energy into reflection, dissipation and transmission can directly be derived from the change in wave height:

$$H_i^2 = H_r^2 + H_{diss}^2 + H_t^2 \quad [2.12]$$

Dividing Equation 2.12 by the incoming wave height squared results in:

$$1 = \left(\frac{H_r}{H_i}\right)^2 + \left(\frac{H_{diss}}{H_i}\right)^2 + \left(\frac{H_t}{H_i}\right)^2 \quad [2.13]$$

$$1 = C_r^2 + C_{diss}^2 + C_t^2 \quad [2.14]$$

where C_r is the reflection coefficient, C_{diss} is the dissipation coefficient and C_t is the transmission coefficient. The wave heights H_i , H_r and H_t are usually determined in experiments, from which the percentage of dissipated wave energy can be calculated:

$$C_{diss}^2 = 1 - \left(\frac{H_r}{H_i}\right)^2 - \left(\frac{H_t}{H_i}\right)^2 \quad [2.15]$$

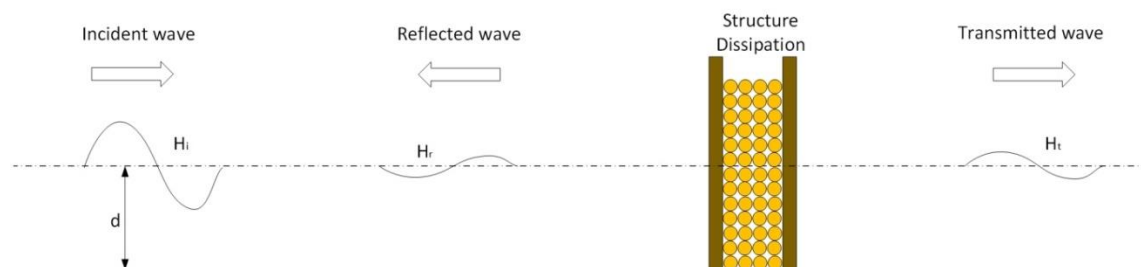


Figure 2.7 Simplified example of wave interaction with brushwood structure (not to scale)

2.2.2 Previous research on wave-structure interaction

Researchers have studied the effect of structures (including brushwood structures) on incoming waves. In these researches, empirical relationships for the transmission coefficient have been established.

Vertical seawall

In 1990, Van der Meer established a first formula for the transmission coefficient of vertical seawalls. For the range of $0.1 < C_t < 0.8$, the following holds:

$$C_t = 0.46 - 0.3 \cdot \frac{R_C}{H_s} \quad [2.16]$$

The formula shows that transmission depends on the ratio between the freeboard (R_C) and the significant wave height (H_s). The parameters are shown in Figure 2.8.

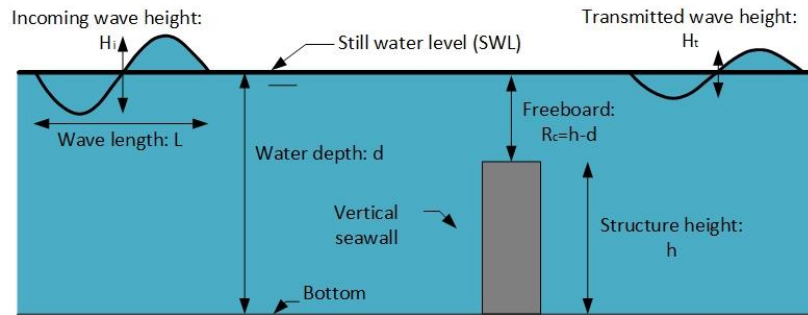


Figure 2.8 Sketch vertical seawall with geometric and wave parameters

Permeable and impermeable breakwaters under a slope

Further research was performed to modify this empirical relationship for the transmission coefficient by d'Angremond et. al. (1996). The difference with the vertical wall is that the wall is under a slope and that both permeable and impermeable breakwaters are used (shown in Figure 2.9). The tested parameters include:

- Relative freeboard: $\frac{R_C}{H_s}$
- Relative crest width: $\frac{B}{H_s}$
- Iribarren-parameter: $\xi = \frac{\tan(\alpha)}{\sqrt{\frac{H_s}{L}}}$

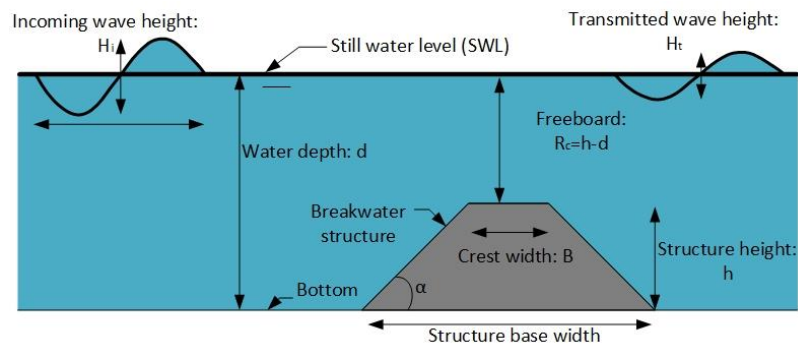


Figure 2.9 Sketch breakwater with geometric and wave parameters

This resulted in the following empirical relationship within the limits of $0.075 < C_t < 0.8$ and $\frac{B}{H_s} < 8$:

$$C_t = -\beta_1 \cdot \frac{R_c}{H_s} + w \quad [2.17]$$

$$\text{With } w = +\beta_2 \cdot \left(\frac{B}{H_s}\right)^{-\beta_3} \cdot (1 - e^{-\beta_4 \cdot \xi})$$

The parameter β_i is a measure for the permeability of the breakwater structure and it is calculated by the least squares fit method. An overview is given in Table 2.1.

Table 2.1 Beta values for permeable and impermeable breakwater structures

For permeable breakwaters	For impermeable breakwaters
$\beta_1 = 0.4$	$\beta_1 = 0.4$
$\beta_2 = 0.64$	$\beta_2 = 0.8$
$\beta_3 = 0.31$	$\beta_3 = 0.31$
$\beta_4 = 0.5$	$\beta_4 = 0.5$

Brushwood structures

In 1999, research was performed by Mai et. al. to modify Equation 2.17 for brushwood structures. The scale model of the brush fence consisted of timber poles with bundled brushwood in between. Various heights were used. Water level variations were measured in front and behind the fence with wave gauges. An overview of the set-up of experiments and the results are shown in Figures 2.10(a) and (b), respectively.

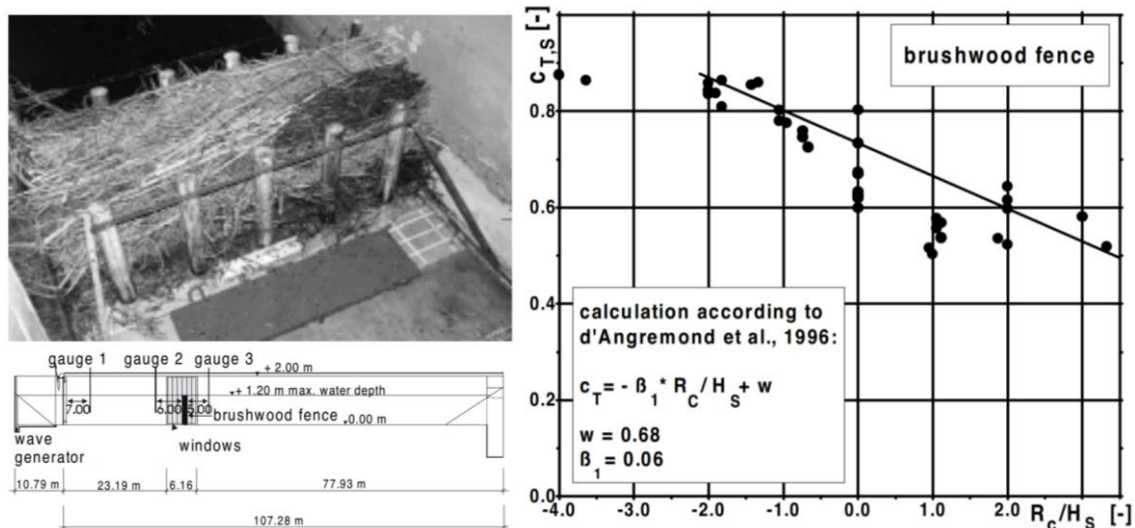


Figure 2.10 (a) Scale model of brushwood fence (b) Transmission of waves at brushwood fence (Mai et. al., 1999)

The following conclusions were drawn in this research from Figure 2.10(b):

- Damping in brushwood fences is more efficient when the structure is emerged compared to submerged conditions.

- The efficiency of the structure decreases linearly at the same rate when water levels vary at both emerged and submerged conditions. This result is quite unexpected, as brushwood fences are basically considered as porous structures, they should have similar trends to permeable breakwaters when they are submerged or emerged as proposed by Cross (1976) and Ting et. al. (2004).

Sayah (2006) performed additional experimental tests with brushwood fences on a fixed bed. An analysis of the following dimensionless variables on the transmission coefficient was provided:

- Freeboard of the structure, $\frac{R_C}{H_i}$
- Height of the structure, $\frac{h}{H_i}$
- Wave number, kd
- Wave steepness, $\frac{H_i}{gT^2}$
- Porosity, n

Regarding the above-mentioned variables, the following conclusions were drawn in this research:

- The response of the structure is different in relation to its immersion condition. It was shown that the efficiency of the brushwood fences decreases rapidly when they are totally submerged.
- The relative freeboard, the wave steepness and the porosity play a major role in the response of the structure regarding wave damping. The effect of the relative height and the wave number is not significant and can be disregarded.
- The effect of the relative freeboard and the porosity of the structure on the transmission coefficient are non-linear while the effect of the wave steepness could be considered as linear.

Next, a non-linear relationship between C_t and the dimensionless variables was proposed and tested:

$$C_t = 0.01 \left(\frac{R_C}{H_i} \right)^2 - 0.11 \frac{R_C}{H_i} + 0.69n^{-0.04} - 12.40 \frac{H_i}{gT^2} (\pm 0.24) \quad [2.18]$$

The method showed quite a good agreement with the physical results as 95% of the data is within a confidence interval for C_t of ± 0.24 . The empirical relationship can be applied within the following ranges:

$$\begin{aligned} -2 &\leq \frac{R_C}{H_i} \leq 2 \\ 0.001 &\leq \frac{H_i}{gT^2} \leq 0.008 \end{aligned}$$

Porosity (n) should be higher than zero. The closer to zero the more inaccurate the results of the equation become.

2.3 Parameterization of wave energy dissipation through permeable structures

This section provides an overview of the existing studies on the parameterization of wave energy dissipation through permeable structures. The permeable structures include granular structures (first sub-section) and vegetation, which is schematized as an array of vertical cylinders (second sub-section).

2.3.1 Wave energy dissipation through granular structures

A number of researchers have studied and parameterized the wave energy dissipation through granular structures. Darcy (1856) performed research on a homogeneous porous medium for laminar groundwater flow. Forcheimer (1901) represented the losses inside a structure with a linear term, associated to viscous losses and with a quadratic term, representative of the turbulent dissipation. Both researches are briefly described in this section.

When a structure is present in the flow field, the flow can no longer be considered as a free surface flow. This is due to the presence of structural elements and voids. The structural elements give resistance to the flow, which causes energy dissipation. The flow is now considered a porous flow. The filter velocity is described by:

$$u_f = nu \quad [2.19]$$

The porosity n is defined as the pore volume over the total volume. The flow velocity u is the actual velocity in the pores. Therefore, the filter velocity can be considered as the velocity averaged over the pores. Darcy discovered the following relationship for the filter velocity:

$$u_f = kI \quad [2.20]$$

in which k is the permeability and I is the pressure gradient. The latter is given by:

$$I = -\frac{1}{\rho g} \frac{\partial p}{\partial x} \quad [2.21]$$

Forcheimer expressed the pressure gradient with a linear and non-linear term. The linear term in the equation is associated with the laminar part of the flow. The nonlinear term in the equation of the pressure gradient is associated with the turbulent part of the flow. The equation is given by:

$$I = au_f + bu_f|u_f| \quad [2.22]$$

The constants a and b have to be determined experimentally. Opposed to granular structures, brushwood structures have an anisotropic character. Anisotropy is defined as the property of being directionally dependent, which implies different properties in different directions. Therefore, the void size differs in horizontal and vertical direction. Due to this difference, the flow is affected differently and the constants a and b derived in previous studies cannot be used for brushwood structures.

2.3.2 Wave energy dissipation through vegetation

Theoretical background

A number of researchers have studied and parameterized the wave energy dissipation through vegetation, schematizing aquatic plants as an array of vertical cylinders. When circular objects are in a flow field, a boundary layer develops along the surface. If the friction with the surface is high enough, the flow cannot follow the surface anymore. When this happens, the boundary layer separates. The wake (separation area) has different shapes depending on the Reynolds number, which can be seen in Figure 2.11(b). Flow separation results in a larger pressure in front of the object than behind the object. This pressure difference results in the drag force on the object and is defined as follows:

$$F_d = \frac{1}{2} \rho C_d A u |u| \quad [2.23]$$

F_d = the drag force (N)

C_d = the drag coefficient (-)

A = the cross-sectional area perpendicular to the flow (m²)

The drag coefficient depends on the shape of the structure and the Reynolds number (Re). For flat objects, the drag coefficient is more constant in comparison to circular objects for different Reynolds numbers, as illustrated in Figure 2.11(a). The drag coefficient of a single circular cylinder varies between 1-1.6 for $10^3 < Re < 10^5$ as shown in Figure 2.11(b).

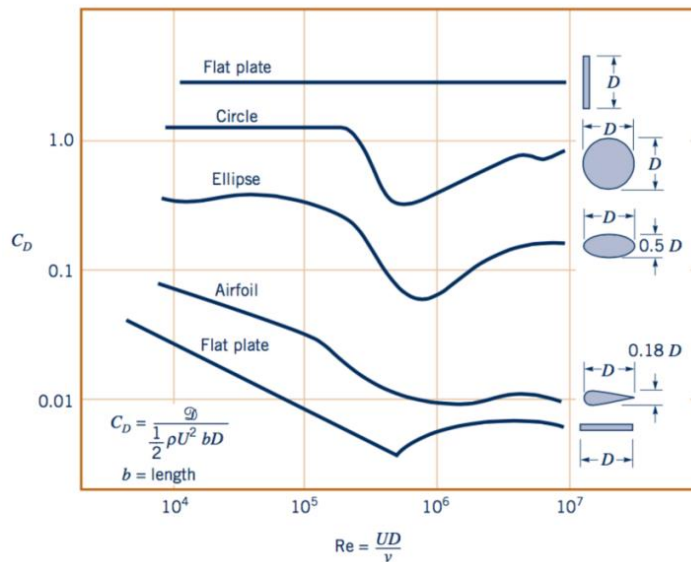


Figure 2.11 (a) Character of the drag coefficient as a function of Reynolds number for objects with various degrees of streamlining (Munson et al., 2013)

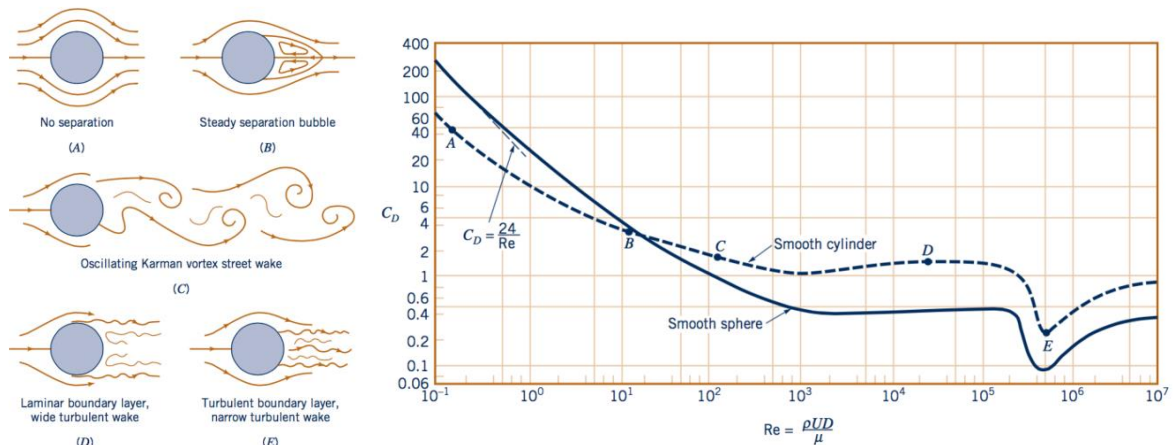


Figure 2.11 (b) Boundary layer and wake structure for different Reynolds numbers (c) Drag coefficient for a circular cross-section as a function of the Reynolds number (Munson et al., 2013)

The drag coefficients shown in Figure 2.11 are determined for single cylinders. When there are multiple cylinders, they may shelter each other. This sheltering effect has been studied by Bokaian and Geoola (1984). Two elements were tested with different lateral and longitudinal spacing in steady flow. In these tests, the drag coefficient of the trailing cylinder has been determined ($Re=2600$). Figure 2.12 shows that for decreasing lateral (T) and longitudinal spacing (L), the drag coefficient of the trailing cylinder decreases. This results from two properties of the wake. The first one is that the trailing cylinder experiences a lower velocity (due to the reduction in the wake). The second one is that the turbulence, which is contributed by the wake, delays the point of separation on the downstream cylinder. This results in a lower pressure difference along the trailing cylinder and therefore a lower drag coefficient. However, under oscillatory flow the results may be different as the flow reverses.

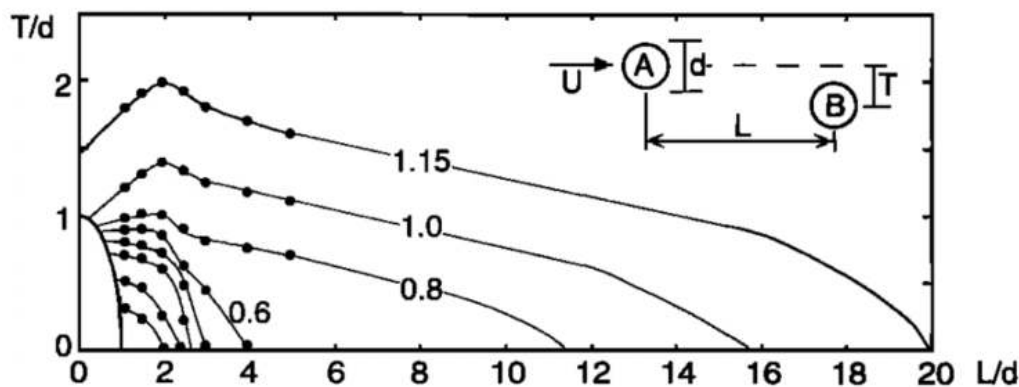


Figure 2.12 Drag coefficient cylinder B for varying lateral and longitudinal spacing between the two cylinders (Nepf, 1999)

Nepf (1999) also performed physical modelling tests for configurations with random arrays and staggered arrays. This has been performed in steady flow, rather than oscillatory flow. The results from the tests are shown in Figure 2.13. In this case the drag coefficient has been averaged over the number of cylinders, which is characterized by the bulk drag coefficient ($\overline{C_D}$). It shows that the bulk drag coefficient decreases with increasing density of the elements (ad). This holds for both random arrays (solid line) and staggered (dashed line) in which the Reynolds number is larger than 200.

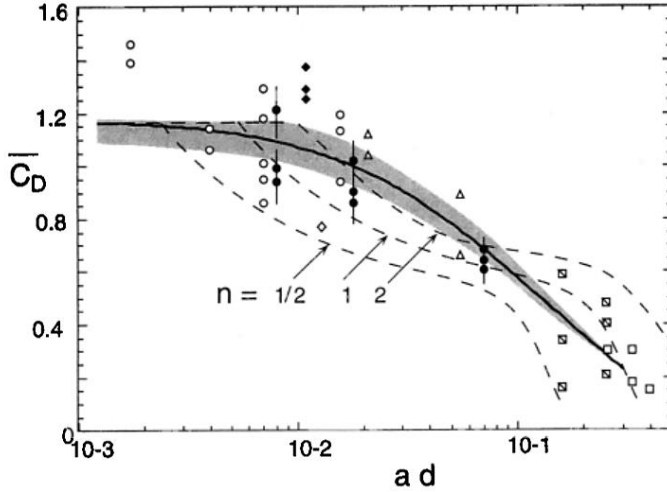


Figure 2.13 Bulk drag coefficient for different densities of elements (Nepf, 1999)

Suzuki and Arikawa (2010) performed numerical modelling tests for cylinders under oscillatory flow. Three different densities are tested, as shown in Figure 2.14. For the three different densities, the arrangement between the elements is the same. The tests are performed with $KC=5$, $Re=6250$ and one diameter of 5 cm. Whether the bulk drag coefficient deviates from the drag coefficient of a single element depends on the ratio $2a/S$, in which:

- $2a$ represents the stroke of motion of the waves
- S is the spacing between the elements

By using small amplitude theory, $2a$ is linearized by KC when the diameter (D) is fixed:

$$2a = \frac{KC}{\pi} D \quad [2.24]$$

Flume data from the first author with a higher KC number of 66 is added to the dataset. The results are shown in Figure 2.15. The blue triangles represent the results from the numerical modelling tests ($KC=5$) and the red dots represent the results from physical modelling tests ($KC=66$). It can be seen that the ratio between the bulk drag coefficient and the drag coefficient of a single element decreases when the stroke of motion of the waves becomes larger than the spacing between the elements.

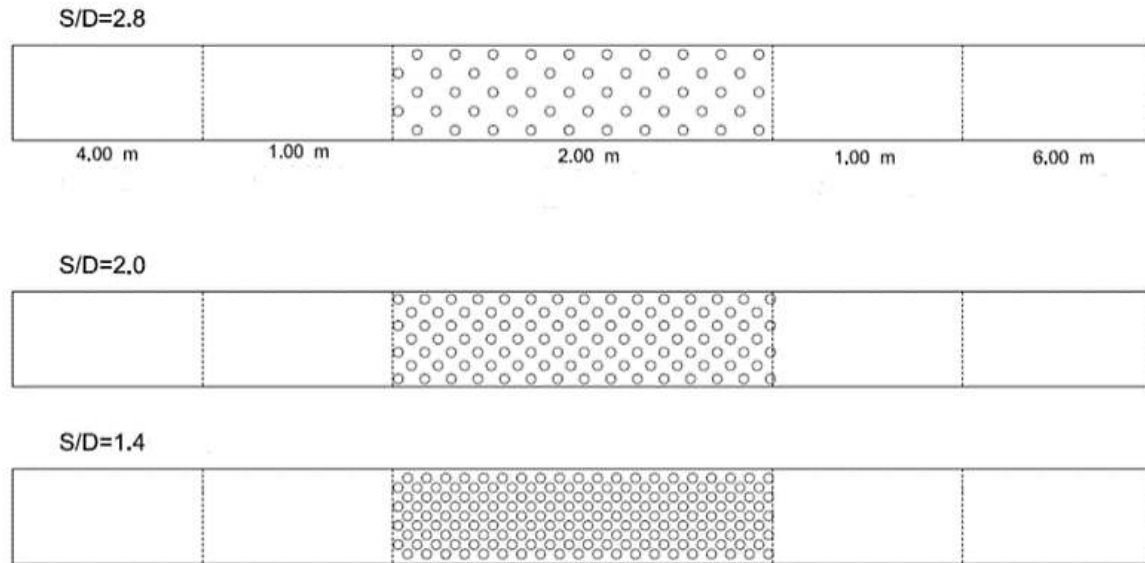


Table 4. Drag coefficient for a single cylinder and bulk drag coefficients in the different densities for multiple cylinders.

CASE	C_D or Bulk drag coefficient
Single cylinder	1.4
$S/D=2.8$ (N=50)	1.39
$S/D=2.0$ (N=100)	1.40
$S/D=1.4$ (N=200)	1.22

Figure 2.14 Vertical elements with three different values of the spacing (S) and their results (Suzuki and Arikawa, 2010)

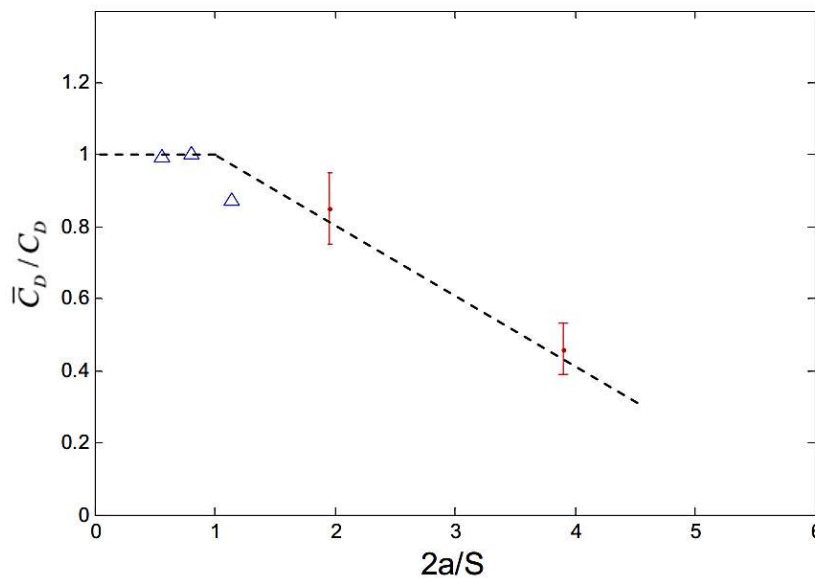


Figure 2.15 Ratio of bulk drag coefficient to drag coefficient versus $2a/S$ (Suzuki and Arikawa, 2010)

Morison (1950) found that in an oscillatory flow, not only the drag force plays a role, but also the inertia force:

$$F = F_I + F_d = C_m \rho \frac{\pi}{4} D^2 \ddot{u} + C_d \frac{1}{2} \rho D u |u| \quad [2.25]$$

F = the force on the cylinder (N)

F_I = the inertia force (N)

F_d = the drag force (N)

C_m = the inertia coefficient (-)

D = diameter of the cylinder (m)

\ddot{u} = the flow acceleration (m/s²)

C_d = the drag coefficient (-)

u = the horizontal velocity due to the wave motion (m/s)

The inertia force is defined by an empirical coefficient as well, which is the inertia coefficient (C_m). To see whether drag or inertia dominates, a direct measurement method can be used. In this method, the force and velocity are measured in time and the empirical coefficients are determined. In order to determine both coefficients, Morison's method can be applied. This method is further explained in Appendix A.

Analytical model wave energy dissipation through cylinders

Dalrymple (1984) derived the energy dissipation through a field of vegetation, which is schematized as an array of vertical cylinders. The wave energy dissipation is defined as the work done by the horizontal drag force:

$$E_{diss} = F_d \cdot u = \frac{1}{2} \rho C_d D u |u| N \cdot u \quad [2.26]$$

F_d = the drag force (N)

u = the horizontal velocity due to the wave motion (m/s)

C_d = the drag coefficient (-)

D = the diameter of the circular cylinder (m)

N = number of elements per unit area (m⁻²)

The horizontal velocity due to the wave motion is obtained by linear wave theory:

$$u = \omega a \frac{\cosh(k(z+d))}{\sinh(kd)} \cos(\omega t - kx) \quad [2.27]$$

Evaluating E_{diss} over the length of the cylinder (assuming that the cylinders are emerged) and u over the wave period T , leads to the following expression:

$$E_{diss} = \int_0^d \frac{1}{2} \rho C_d D u |u| N \cdot u \, dz \quad [2.28]$$

Combining Equation 2.28 and the dispersion relation from Equation 2.1, gives the following expression for wave dissipation:

$$E_{diss} = \frac{2}{3\pi} \rho C_d D \frac{N}{k} \cdot \frac{(\sinh(kd)^3 + 3\sinh(kd))}{3 \cosh(kd)^3} \left(\frac{gk}{\omega}\right)^3 a^3 \quad [2.29]$$

a = amplitude of the incoming wave (m)

k = the wave number (rad/m)

ω = the angular frequency (rad/s)

d = the water depth (m)

The energy conservation equation is given by:

$$\frac{\partial(Ec_g)}{\partial x} = -E_{diss} \quad [2.30]$$

E = wave energy per unit area (J/m²)

c_g = wave group velocity (m/s)

x = direction of wave propagation

Using the energy conservation equation, an expression for the transmission coefficient is found:

$$C_T = \frac{H_T}{H_i} = \frac{1}{1 + \alpha x} = \frac{1}{1 + \left(\frac{E_{diss}}{a^2 \rho g c_g}\right) w} \quad [2.31]$$

w = width of structure in direction of wave propagation (m)

Further vegetation studies have been performed using Dalrymple's model. The drag coefficients are either derived through a direct measurement method (as explained before) or by a calibration method. In the calibration method Equation 2.31 is used, in which the incoming and transmitted wave height are measured. From these measurements the drag coefficient can be determined. An overview of various studies is shown in Table 2.2. In these studies, the vegetation is schematized in various ways including flexible plant strips, flexible real vegetation and wooden rigid cylinders. The latter schematization is most similar to the brushwood structures.

Some limits of applying Dalrymple's model on the brushwood structures are pointed out. In Dalrymple's model the effect of reflection is not included. In the case of vegetation, high porosities are considered and therefore reflection is low. As reflection is low, especially in terms of wave energy, this effect is neglected. However, in some cases, for instance in the case of less porous brushwood structures, reflection can be high enough to have a significant influence on the wave energy dissipation. As reflection

increases, the dissipated wave energy in the structure becomes lower. Therefore, reflection cannot be neglected. Furthermore, the cylinders are vertically orientated. Looking at the brushwood structures, the elements are placed horizontally. In that case, the vertical drag force also acts on the structure, which might lead to an increase in wave dissipation. Moreover, the inertia effect is ignored in Dalrymple's model, which might become important for small KC numbers.

Table 2.2 Overview of vegetation studies on the drag coefficient with various schematizations

Study	Schematization	Flow	C_d relation	Deriving method
Kobayashi et al. (1993)	Flexible plastic strips	Waves	$C_d = 0.08 + \left(\frac{2200}{Re}\right)^{2.4}$ $2200 < Re < 18000$	Calibration method
Mendez et al. (1999)	Flexible plastic strips	Waves	$C_d = 0.08 + \left(\frac{2200}{Re}\right)^{2.2}$ $200 < Re < 15500$	Calibration method
Mendez and Losada (2004)	Flexible real vegetation	Waves	$C_d = 0.47 \exp(-0.052KC)$ $R^2 = 0.76$ $3 \leq KC \leq 59$	Calibration method
Bradley and Houser (2009)	Flexible real vegetation	Waves	$C_d = 253.9KC^{3.0}$ $R^2 = 0.95$ $0 < KC < 6$	Calibration method
Infantes et al. (2011)	Flexible real vegetation	Waves	$\log(C_d) = -0.6653 \log(Re) + 1.1886$ $R^2 = 0.77$	Direct measurement method
Jadhav et al. (2013)	Flexible real vegetation	Waves	$C_d = 70KC^{0.86}$ $R^2 = 0.95$ $25 < KC < 135$	Calibration method
Hu et al. (2014)	Rigid wooden cylinders	Waves + current	$C_d = 1.04 + \left(\frac{730}{Re}\right)^{1.37}$ $R^2 = 0.66$ $300 < Re < 4700$	Direct measurement method
Anderson and Smith (2014)	Flexible plastic strips	Waves	$C_d = 1.10 + \left(\frac{27.4}{KC}\right)^{3.08}$ $R^2 = 0.88$ $26 < KC < 112$	Calibration method
Ozeren et al. (2014)	Rigid wooden cylinders	Waves	$C_d = 1.5 + \left(\frac{6.785}{KC}\right)^{2.22}$ $R^2 = 0.21$	Calibration method
Losada et al. (2016)	Flexible real vegetation	Waves	$C_d = 0.08 + \left(\frac{50000}{Re}\right)^{2.2}$	Calibration method

3. Set-up of experiments

In this chapter a description of the set-up of experiments is presented. The different components of the set-up are described, including the wave generator, wave absorber and physical scale model. Thereafter, the design of the model is further elaborated. Next, a selection of different wave cases is made, after which a description of the set-up of the wave gauges is given. Finally, the configurations that are made with the model are presented.

3.1 Description of the set-up

The experiments are performed at the Environmental Fluid Mechanics Laboratory at TU Delft. For the experiments a wave flume is used. The flume has a wave generator at the beginning and a wave absorber at the end. The length of the wave flume is 39 m. The physical scale model is placed at a 20 m distance from the wave generator. An overview of the set-up is illustrated in Figure 3.1. The measuring equipment is not shown here, but is further described in Section 3.4.

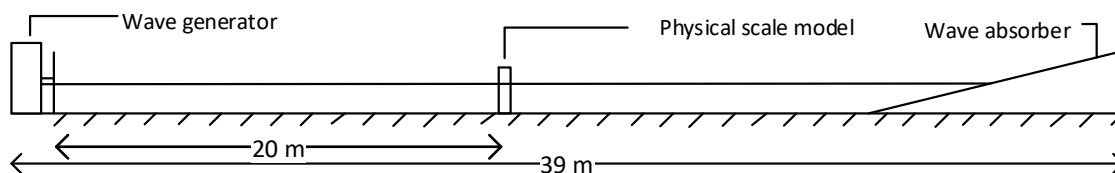


Figure 3.1 Sketch of set-up of experiments

The wave generator is capable of creating regular waves, where the user has to choose which combination of wave height, water depth and wave period is used. The capacity of the wave generator is shown in Figure 3.2. In this figure it becomes clear which combination of water depths, wave heights and wave periods can be generated without the occurrence of wave breaking, taking into account the steepness and depth limit of the waves. Furthermore, the wave generator has an automated reflection compensator in order to minimize reflection from the wave board.

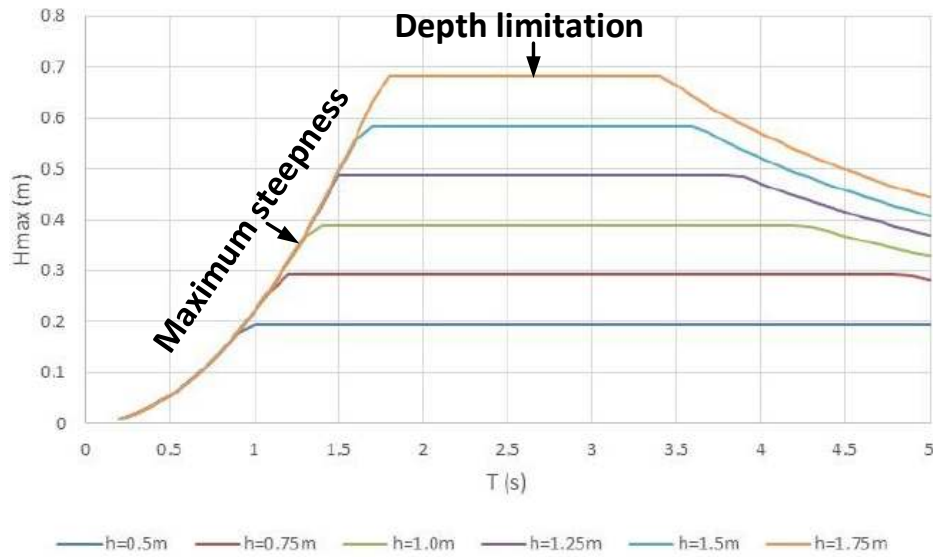


Figure 3.2 Capacity of the wave generator (van der Meer, 2010)

Figure 3.3 shows the wave absorber at the end of the flume. The wave absorber is placed in order to minimize the waves travelling back to the scale model. A slope of approximately 1:3 is used. An overview of the scale model is shown in Figure 3.4. The model is stabilized with two wooden bars in order to prevent it from moving.



Figure 3.3 Wave absorber at the end of the flume

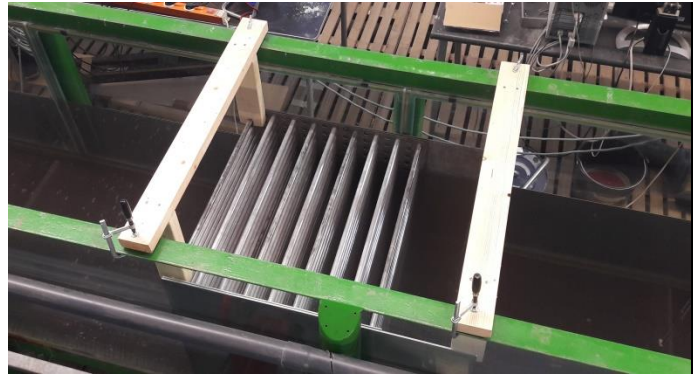


Figure 3.4 Top view physical scale model

3.2 Design of physical scale model

The design of the physical scale model is based on the full scale structures applied in the mangrove restoration project in Demak (2013). Therefore, information about the properties of the brushwood structures is provided first. The structures in Demak consist of vertical and horizontal elements. The vertical elements are either bamboo poles or PVC poles with diameters varying from 0.12-0.15 m. The horizontal elements consist of brushwood. These elements can be seen as filling material of the structure. Based on the study of Lucas (2017) the porosity of the brushwood is estimated to be $n=0.25-0.40$. The brushwood material is horizontally constrained by the vertical elements (bamboo or PVC poles) and vertically constrained by horizontal bamboo beams and nylon ropes. An impression of the structures is shown in Figure 1.8. The size of the brushwood material is determined from a sample taken at the project location in Demak, which can be seen in Figure 3.5. The diameter of the brushwood branches varies between 0.5-3.0 cm. The frequency of each of the diameters can be found in Table 3.1 and Figure 3.6.



Figure 3.5 Sample of the brushwood material used in Demak (Gijón Mancheño, 2017)

Table 3.1 Full range of brushwood diameters

Brushwood (total=24)	
Diameter	Frequency
0.5 cm	4%
1.0 cm	25%
1.5 cm	33%
2.0 cm	25%
2.5 cm	3%
3.0 cm	4%

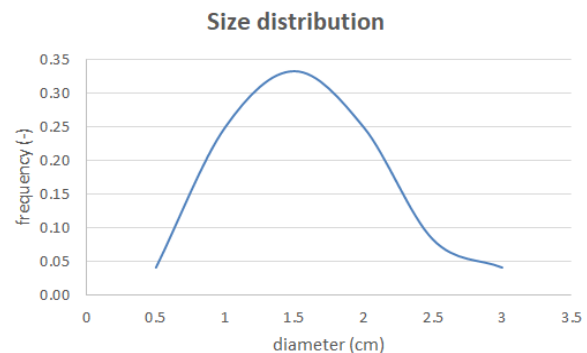


Figure 3.6 Size distribution of brushwood

In Section 2.3 formulations for wave dissipation through both granular structures and a group of vertical cylinders are shown. As the brushwood structures are formed by branches that are more similar to the shape of cylinders, it is chosen to model the brushwood in this (simplified) way. However, the brushwood branches are not vertically but horizontally orientated. In order to compare results with the existing literature mentioned in Section 2.3, both vertical and horizontal orientations are tested. This is also done to see whether it is possible to achieve a comparable amount of wave dissipation by using vertical elements only (as brushwood requires intensive

maintenance). Section 2.3 shows that the arrangement of elements and porosity have a significant influence on the drag coefficient and therefore the dissipation of the waves. Furthermore, Equation 2.29 shows that the width of the structure has a significant influence on the wave dissipation. Therefore, the effect of the arrangement, porosity and width are tested as well. For the design of the physical scale model it is convenient that multiple effects can be tested without needing a new model.

For the porosity of the structure it is chosen to be in the high porosity range ($n > 0.50$). The reasoning behind this is that low porosity cases lead to high reflection as the structure comes closer to an impermeable wall. This would hinder the stability of the structure and would enhance erosion in front of it. In addition, separating the elements leads to an increase in drag which leads to an increase in wave dissipation, as shown in Section 2.2.3. Furthermore, a high number of elements are needed for the low porosity cases. This is not preferred as it increases the costs of the model and changing configurations of the structure becomes quite time consuming. For this series of tests, a porosity of $n = 0.80$ is chosen as a lower limit. The choice for the size of the elements is based on the brushwood size that is used in the field. The brushwood size with the highest frequency is equal to 1.5 cm (shown in Figure 3.6). Having a cylinder size in the flume that is comparable with the brushwood size in the field, allows having more comparable KC and Re numbers as both parameters are a function of the element size. The available cylinder size that is closest to the size in the field is 2.0 cm and therefore this size is chosen. Furthermore, the cylinders are made out of aluminum.

The cylinders are fixed on both ends by two grids, which is shown in Figure 3.5 (c). The elements can be taken away and added to the grid. Therefore, different arrangements, porosities and widths can be reproduced. Taking into account a flume width of 80 cm and some tolerance for placing the model inside the flume, has led to the grid design shown in Figures 3.5(a) and (b). In this grid design a minimum porosity of $n = 0.80$ is used, which has led to a spacing of 21 mm between the elements. To be able to test the effect of the orientation with one scale model, the model is able to rotate 90 degrees, as illustrated in Figure 3.8. The frontal area of the scale model therefore has a square shape of 78x78 cm. The grey cylinders are the cylinders that can be taken away and added to the structure. The green cylinders are the cylinders that are always present in order to provide strength and stability of the structure, also during lifting it in and out of the flume. The green cylinders are part of the structure in most configurations. However, there are also some cylinders that provide strength and stability without being part of the structure. These are represented in red.

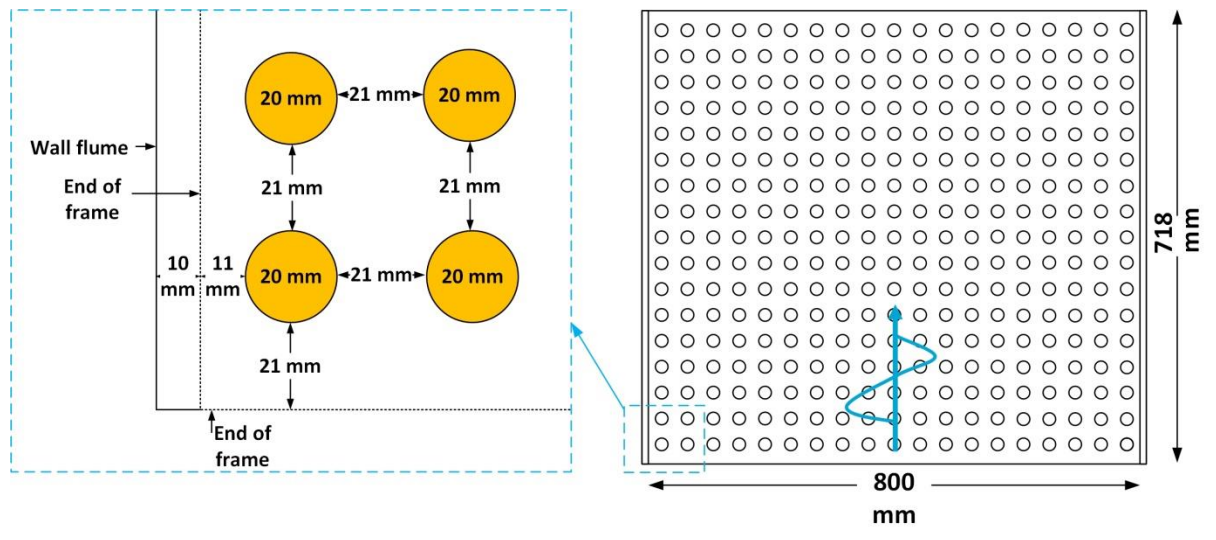


Figure 3.7 (a) Top view of design of the grid for both ends of the cylinders (b) Actual grid (c) Grids on both ends of the cylinders (in lifted position)

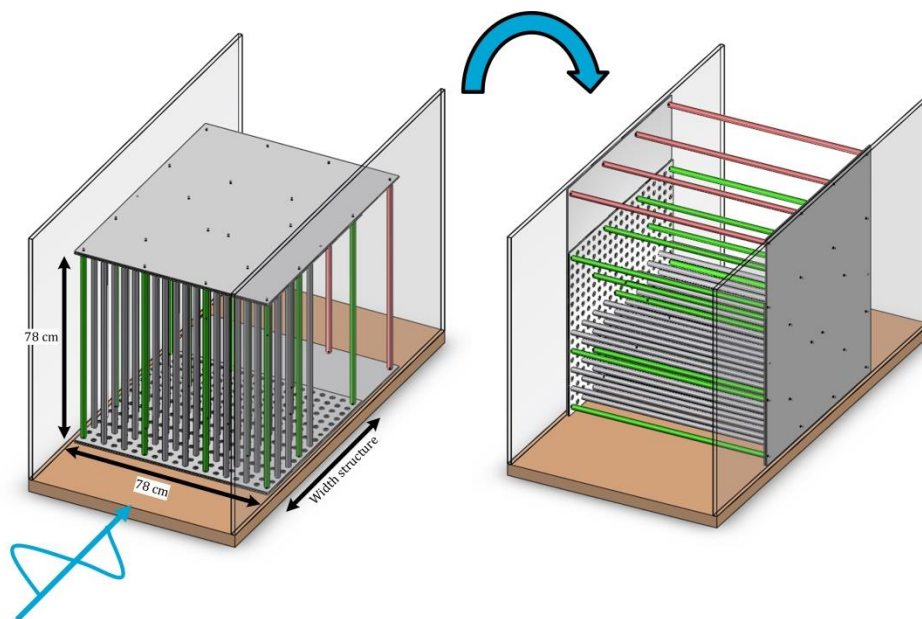


Figure 3.8 3D design of the physical scale model both vertically and horizontally orientated

The width of the structure, which is indicated in Figure 3.8, is chosen in such a way that it resembles the width of the structure in the field. The width of the structure in the field is around 0.5 m. To be able to look at the width effect of the structure, two widths are tested: 0.35 m and 0.68 m. These values are similar to the values in the field and therefore beneficial for scaling, which is further explained in Section 3.3. Reason that no values such as 0.5 m and 1.0 m are chosen is because of the limited number of elements. The number of elements that are used in the tests is equal to 171. Reason for limiting the number of elements is that the structure should not become too heavy to lift, it should not be too time consuming to change the configurations and finally for economic reasons. Having 171 elements means that only half the grid (indicated in Figure 3.7) can be filled which has a porosity of 0.80. Increasing the width of the structure and keeping the same porosity is therefore not possible. However, what can be done is spreading out the same number of elements (171) over a larger width of 0.68 m. Therefore, the porosity increases from 0.80 to 0.90. To be able to look at the width effect exclusively, the porosity of 0.90 can also be created with a structure width of 0.35 m.

Besides the width effect, it also becomes interesting to look at the effect of spreading out the same number of elements over a larger area. Reason that it can be interesting is that higher dissipation rates might be achieved without adding extra material. Therefore, this effect is added to the set of tests as well. To summarize, the following effects are tested:

- Orientation (horizontal vs. vertical)
- Porosity
- Spreading out the same number of elements over a larger area
- Arrangement
- Width

Not all combinations of effects are tested. The combinations that are made are explained in Section 3.5. In this section the different configurations that are made with the grid are shown. The different tested effects are represented by the different configurations.

3.3 Scaling

3.3.1 Scaling rules

The wave induced flow can be characterized by several dimensionless parameters which are explained in Section 2.1.5. These include the Froude number, the Reynolds number and the Keulegan Carpenter number. These dimensionless parameters allow scaling the field conditions to the flume scale.

The Froude number has to be the same for the prototype (structure in the field) and the scale model (structure in the flume). To be able to fulfil this requirement scaling rules have to be applied. First a characteristic length scale in the prototype and scale model has to be defined. The ratio between these is the scaling factor n :

$$n = \frac{\text{Characteristic length scale prototype}}{\text{Characteristic length scale scale model}} = \frac{L_p}{L_m} \quad [3.1]$$

With the characteristic length scale n , other scales can be determined:

$$\begin{aligned} \text{Time scale:} \quad & \frac{t_p}{t_m} = \sqrt{n} \\ \text{Velocity scale:} \quad & \frac{u_p}{u_m} = \sqrt{n} \\ \text{Force scale:} \quad & \frac{F_p}{F_m} = n^3 \end{aligned}$$

Furthermore, it is favourable that the Reynolds number (Re) and Keulegan Carpenter number (KC) are the same in the prototype and the scale model. However, as these scales conflict it is only possible to have these numbers in the same order of magnitude rather than having the exact same value.

3.3.2 Field conditions

In order to produce data a full scale example is chosen on which the scaling rules are applied, aiming to create a similar flow regime. As discussed in Sections 1.1 & 1.4, the full scale example is taken from the project location Demak. Based on field observations, a number of representative (local) wave conditions are provided by Witteveen + Bos.

The significant wave height (H_s) varies between 0.25 m (daily conditions) and 1.5 m (extreme conditions) as shown in Figure 3.9. The local water depth varies between 0.20 m and 1.20 m and the wave period varies between 1-5 s. Taking into account the depth- and steepness limits for wave breaking (described in Section 2.1.3), the H_s/d and H_s/L ratios that remain are:

$$0.21 \leq H_s/d \leq 0.60$$

$$0.01 \leq H_s/L \leq 0.06$$

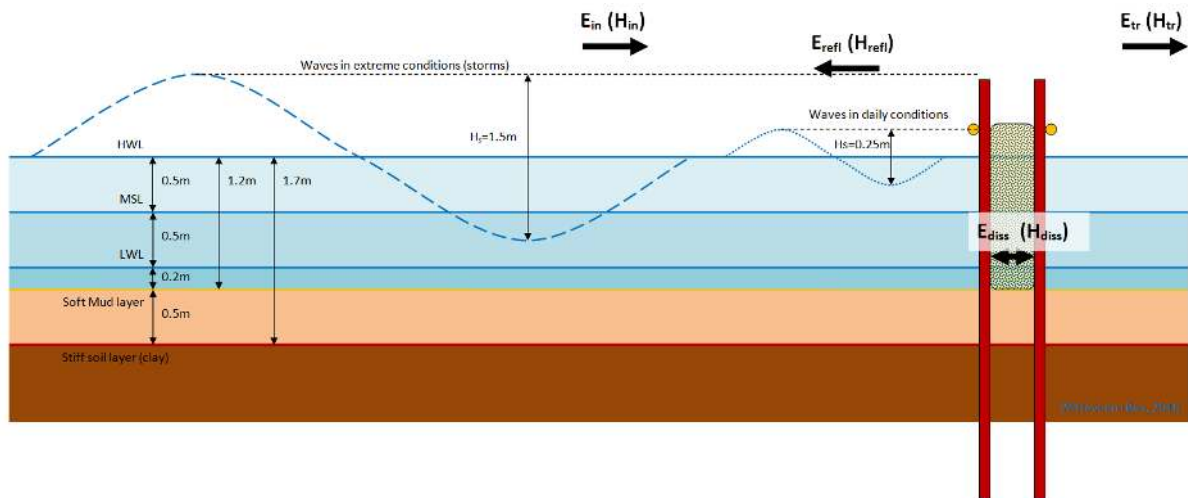


Figure 3.9 Wave conditions based on field observations in Demak. Adapted from: (Witteveen+Bos, 2018).

Besides these ‘expert estimates’, measurements have been done at several locations in the project area. From these measurements, it becomes clear that wave periods larger than 5 s occur as well.

The measurements include the significant wave height, wave period and water depth and are done in both summer and winter. An overview of the locations with the results of the measurements is shown in Appendix B. At the locations of the measurements it becomes clear that the significant wave height changes between 0.02-0.05 m in summer. The water depth varies between 0.02 and 0.50 m with periods varying between 3-5 s. The plots for the winter period are less clear. It seems that with a water depth of 0.60 m, wave heights of 0.10 m occur with a wave period of 8 s. For a larger water depth of 0.80 m, wave heights of 0.20 occur with a period of 7-8 s.

Figure 3.10(a) shows the most offshore location (WL45). The results of this location, presented in Figure 3.10(b), are recorded in the winter period. The results are clearer in this case, showing that wave periods vary between 5-8 s. This does not change the range of the wave steepness shown above. However, it does indicate that longer waves occur. Based on the dispersion relation (shown in Equation 2.2), wave lengths up to 35.4 m occur. In the case where the wave periods are between 1-5 s, wave lengths only vary between 2.2 m – 22.2 m.



Figure 3.10(a) Locations of the wave loggers in the project area (source: Google Earth)

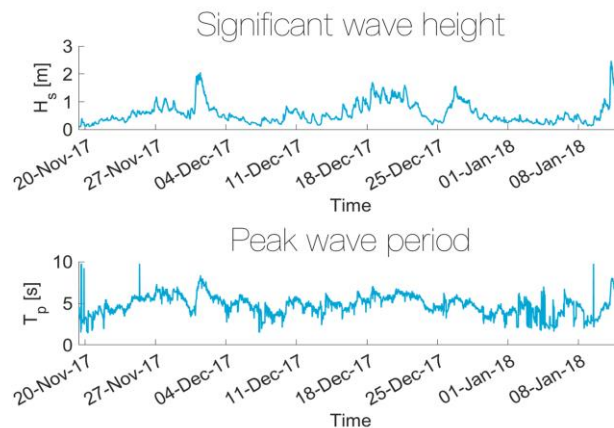


Figure 3.10(b) Results of wave logger WL45

3.3.3 Scaled conditions

In reality an irregular wave field is present with a large number of waves with different heights and periods that interact with each other. In contrast to the case of irregular waves, regular waves have a single value for the wave height H and the wave period T . It is practical to have single values that characterize the entire wave field, as this simplifies calculations. For this reason and to decrease the testing time the choice is made to do the test with regular waves.

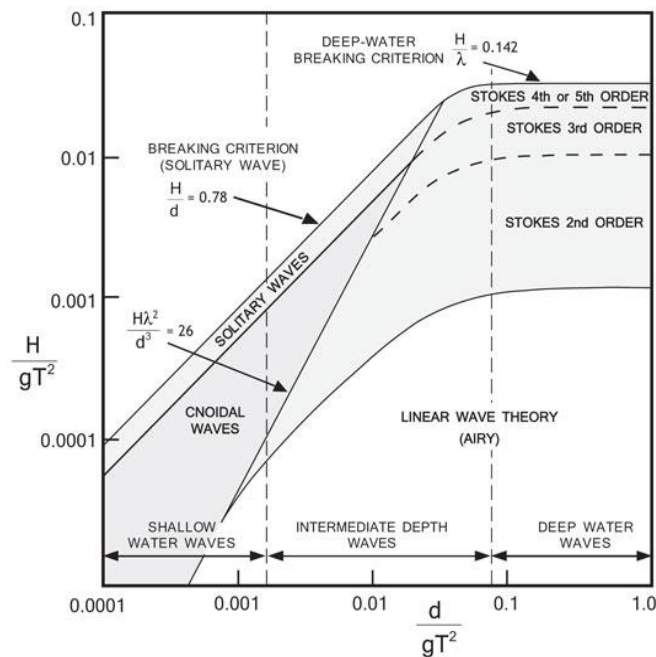


Figure 3.11 Applicability linear wave theory (Le Mehauté, 1976)

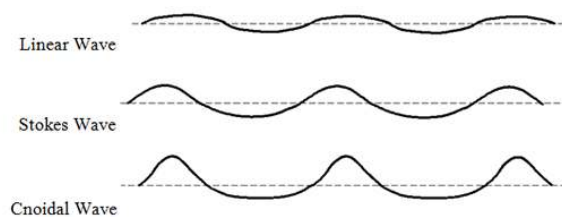


Figure 3.12 Shapes of wave from the different zones

Although the intention is to have regular linear waves, in practice most of the waves are non-linear. The shape of the wave are not perfectly sinusoidal, but have smaller crests and longer troughs as shown in Figure 3.12. Figure 3.11 shows the different wave zones according to Le Mehauté (1976).

Staying in the linear wave zone, indicates that low wave heights with high water depths have to be used. However, this leads to wave height to water depth ratios lower than 0.21, which would not be in agreement with the field conditions mentioned in Section 3.3.2. Furthermore, to clearly see how the wave energy balance (reflection, dissipation and transmission) is affected for different wave cases, it is preferable that the weight height that is chosen is not too low, as there is not much wave energy to dissipate.

Moreover, the maximum surface elevation relative to the bottom must stay below the structure height.

In the first series of tests wave heights of 7, 12 and 19 cm were chosen to test. However, the 7 cm wave was too low to measure dissipation and the 19 cm waves were too non-linear, which complicates the physics. Therefore, the choice was made to continue with 13 and 16 cm waves, shown in Table 3.2. A water depth of 0.5 m is used with wave periods varying between 1-3 seconds. These values are chosen aiming to cover the field conditions as much as possible. Results are shown in Table 3.3.

Table 3.2 Wave cases and various dimensionless parameters (first test series)

Name	d (m)	H (m)	T (s)	H/d	H/L	Fr	Re	KC	kd
H13T1	0.50	0.13	1.0	0.26	0.09	0.09	$3.9 \cdot 10^3$	10	2.1
H13T1.5	0.50	0.13	1.5	0.26	0.05	0.11	$4.9 \cdot 10^3$	18	1.1
H13T2	0.50	0.13	2.0	0.26	0.03	0.12	$5.3 \cdot 10^3$	26	0.8
H13T3	0.50	0.13	3.0	0.26	0.02	0.13	$5.5 \cdot 10^3$	42	0.5
H16T1.5	0.50	0.16	1.5	0.32	0.06	0.14	$6.0 \cdot 10^3$	23	1.1
H16T2	0.50	0.16	2.0	0.32	0.04	0.15	$6.5 \cdot 10^3$	33	0.8
H16T3	0.50	0.16	3.0	0.32	0.03	0.15	$6.8 \cdot 10^3$	51	0.5

Table 3.3 Dimensionless wave parameter in both the flume and field (first test series)

Flume	Field
$0.26 \leq H/d \leq 0.32$	$0.22 \leq H_s/d \leq 0.60$
$0.02 \leq H/L \leq 0.09$	$0.01 \leq H_s/L \leq 0.06$
$0.05 \leq w/L \leq 0.45$	$0.01 \leq w/L \leq 0.23$

The results of the first test are shown in Figure 3.13. The results are from three different vertical configurations, representing the arrangement effect (explained in Section 3.5). However, the aim of this figure is not to explain arrangement effects, but to indicate that the two different wave heights have similar results. Furthermore, it seems that there is a gap in the plot, where there might be a maximum value for the wave dissipation. Moreover, the waves with the 3 second period are in the cnoidal wave zone.

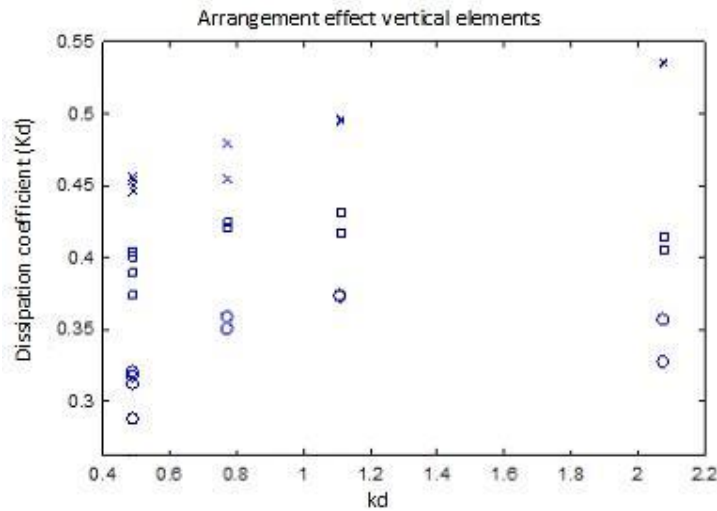


Figure 3.13 Dissipation coefficient vs. kd for different arrangements

For the above reasons some changes are made in the second test series. In order to decrease to level of non-linearity, the water depth is increased from 0.5 m to 0.6 m. To fill up the gap in the plot, two more wave periods are added to the tests, including 1.13 and 1.25 s. As the results for the two different wave heights are similar, it is chosen to continue with one wave height only, which is $H=0.13$ m.

Furthermore, the cnoidal waves are left out of the test series as the shape of the waves deviates more from linear waves in comparison to Stokes waves. These are the waves with wave periods larger than 2 seconds. The wave cases in this research are in the Stokes 2nd and 3rd order region, indicating that the waves cannot be fully described by linear wave theory. An overview of the wave cases is shown in Table 3.4.

Table 3.5 shows the wave height to water depth ratio, the wave steepness and the structure width to wave length ratio in both the flume and field. It can be concluded that the field conditions are not fully covered in the set of tests. Only daily conditions are represented, with a focus on the shorter waves. Short waves stir up sediment behind the brushwood structures, which enhances erosion. Therefore, understanding short wave attenuation could help mitigating this process and optimize structure design.

Table 3.4 Wave cases and various dimensionless parameters (second test series)

Name	d (m)	H (m)	T (s)	H/d	H/L	Fr	Re	KC	kd
H13T1	0.60	0.13	1.0	0.22	0.09	0.068	$3.3 \cdot 10^3$	9	2.5
H13T1.13	0.60	0.13	1.13	0.22	0.07	0.076	$3.7 \cdot 10^3$	11	2.0
H13T1.25	0.60	0.13	1.25	0.22	0.05	0.081	$3.9 \cdot 10^3$	13	1.7
H13T1.5	0.60	0.13	1.50	0.22	0.04	0.089	$4.3 \cdot 10^3$	16	1.3
H13T2	0.60	0.13	2.0	0.22	0.03	0.097	$4.7 \cdot 10^3$	24	0.9

Table 3.5 Dimensionless wave parameter in both the flume and field (second test series)

Flume	Field
$H/d = 0.22$	$0.13 \leq H_s/d \leq 0.60$
$0.03 \leq H/L \leq 0.09$	$0.01 \leq H_s/L \leq 0.06$
$0.09 \leq w/L \leq 0.45$	$0.01 \leq w/L \leq 0.23$

3.4 Setup of wave gauges

The incoming, reflected and transmitted wave heights are measured by wave gauges, which are shown in Figure 3.13. As regular waves are being tested only two wave gauges are needed to be able to distinguish the incoming wave and the reflected waves. To be able to do this the method of Goda and Suzuki (1976) is used, which is explained in more detail in Appendix C.

Two wave gauges are placed in front of the structure to measure the incoming and reflected waves. To measure the transmitted waves and the reflected waves from the wave absorber, two wave gauges are placed behind the structure as well. To be able to apply the method of Goda and Suzuki, the distance between the structure and the wave gauges has to be at least 20% of the wave length. In addition, the distance between the wave gauges has to be 25% of the wave length. An overview of the total set up including the wave gauges is shown in 3.14. The set-up of the physical scale model and the wave gauges is shown in Figure 3.15(a). Note that the distance between the wave gauges is adjusted for every wave case.

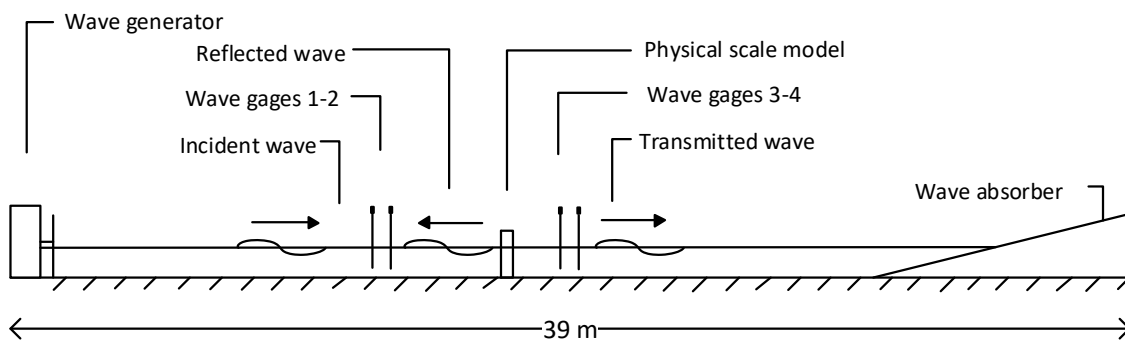


Figure 3.14 Experimental set-up including the wave gauges

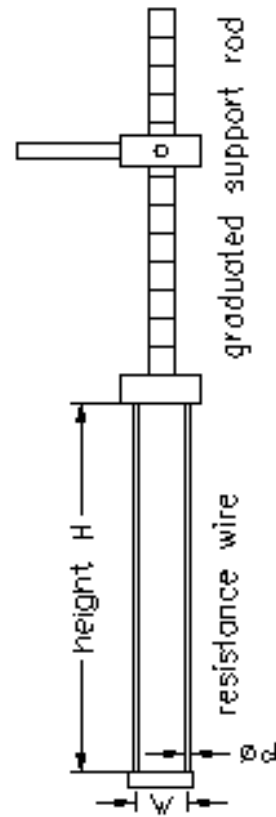
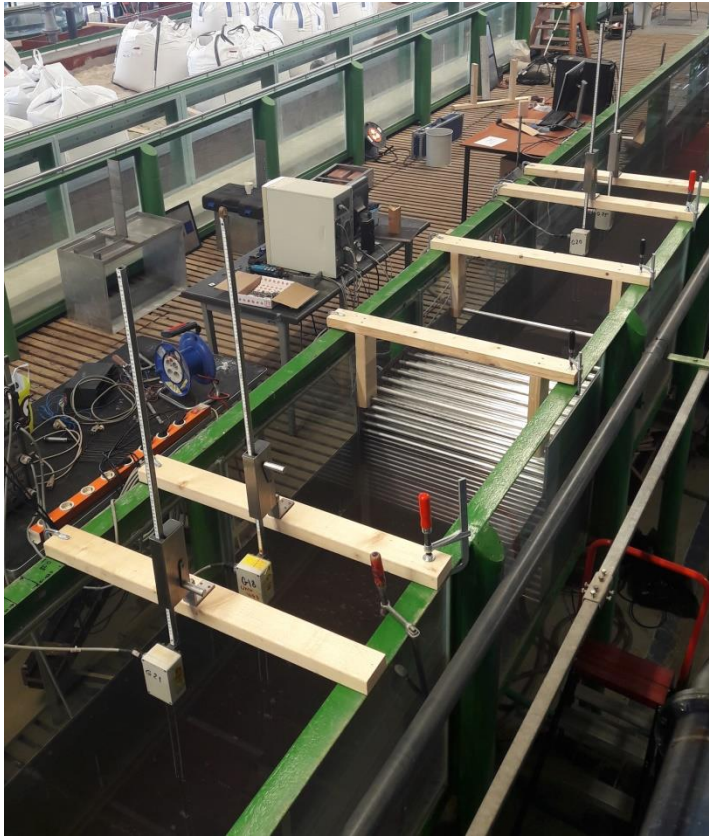


Figure 3.15 (a) Set up of physical scale model and the four wave gauges (b) Sketch of wave gauge (Edinburgh Designs, 2016)

The wave gauges measure the conductivity depending on the water level and give a signal varying between -10V and 10V. Therefore, the wave gauges need to be calibrated individually. This is done by creating a series of fixed water level differences and measuring the corresponding response in volts. There is a linear relationship between the water level and voltage. By using this linear relationship, the measurements in volts are translated into water level measurements. The wave gauges have an accuracy of ± 1 mm. A sketch of the wave gauge is shown in Figure 3.15(b). More information on the specification of the wave gauges is found in Appendix D.

3.5 Description of configurations

In this section the different configurations, representing the different effects of the structure, are described. The five wave conditions, mentioned in Section 3.3.3, are tested for each configuration. As explained in Section 3.2 the following effects are tested: orientation (horizontal vs. vertical), porosity, spreading out the same number of elements over a larger area, width and arrangement. For all the configurations the effect of the orientation is tested. The configurations presented next show the top view of the grid with an arrow representing the direction of wave propagation. Note that only the vertical elements are presented. In case of the horizontal elements the exact same configurations are used, only with a 90 degrees rotation of the structure.

The number of elements that are used is equal to 171. With this number half the grid (with a width of 0.35 m) can be filled, as shown in Figure 3.16(a). When half the grid is filled, the porosity is equal to $n=0.80$. In this case the spacing between the elements is the same in longitudinal direction (indicated with a) and in the lateral direction (indicated with b). To exclusively test the porosity effect, distances a and b should be equal to each other, which makes that the elements should be placed in the same (uniform) way. To reach a higher porosity case that can be compared to the lower porosity case of $n=0.80$, elements are taken away in both the longitudinal and lateral direction. In this case the porosity is equal to $n=0.94$, as shown in Figure 3.16(b).

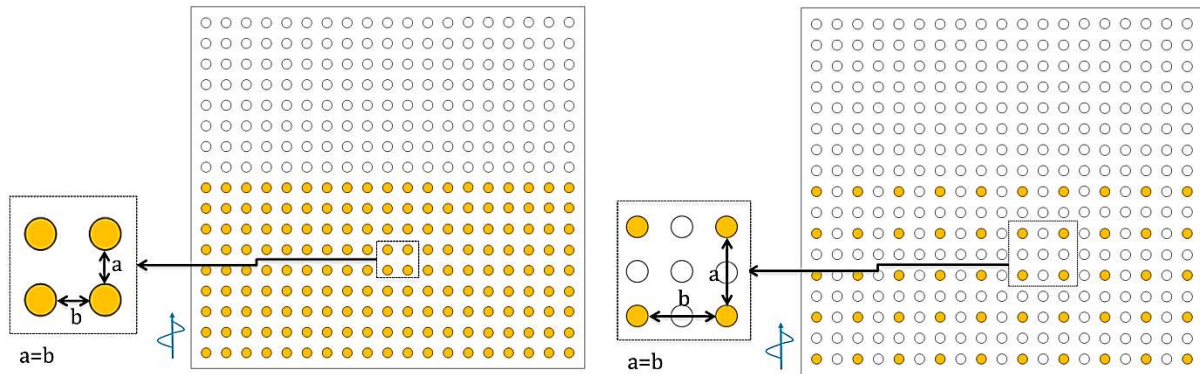


Figure 3.16 (a) Configuration with porosity 0.80, width 0.35 m and uniform placement of the elements (b) Configuration with porosity 0.94, width 0.35 m and uniform placement of the elements

Looking at the porosity case of 0.80, the structure width is equal to 0.35 m and the number of elements is equal to 171. For the next configurations, the elements are spread out over a larger area, which has a width of 0.68 m. Redistributing the elements is done in three different ways. Therefore, the arrangement effect is tested as well. The elements are spread out in such a way that:

- the longitudinal spacing between the elements is larger than the lateral spacing between the elements ($a > b$) as shown in Figure 3.17(b).
- the lateral spacing between the elements is larger than the longitudinal spacing between the elements ($b > a$) as shown in Figure 3.18(b).
- the elements are placed in a staggered position ($a = b$) as shown in Figure 3.19(b).

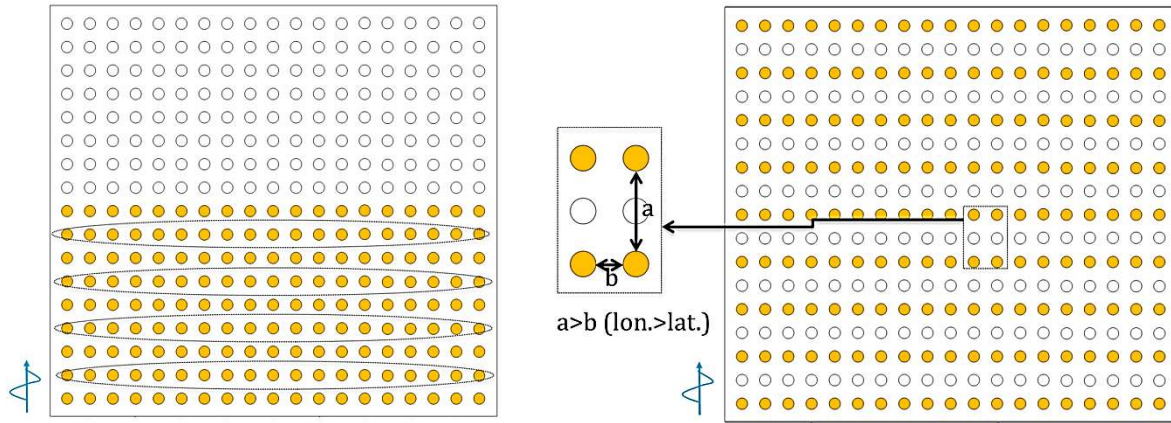


Figure 3.17 (a) Configuration with porosity 0.80, width 0.35 m and uniform placement of the elements (b) Configuration with porosity 0.90, width 0.68 m and the longitudinal spacing between the elements is larger than the lateral spacing ($a > b$)

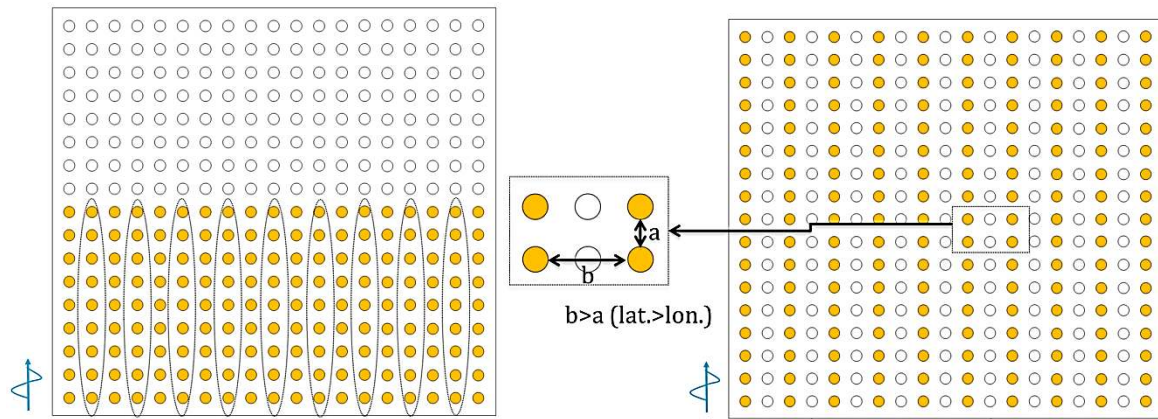


Figure 3.18 (a) Vertical configuration with porosity 0.80, width 0.35 m and uniform placement of the elements (b) Vertical configuration with porosity 0.90, width 0.68 m and the lateral spacing between the elements is larger than the longitudinal spacing ($b > a$)

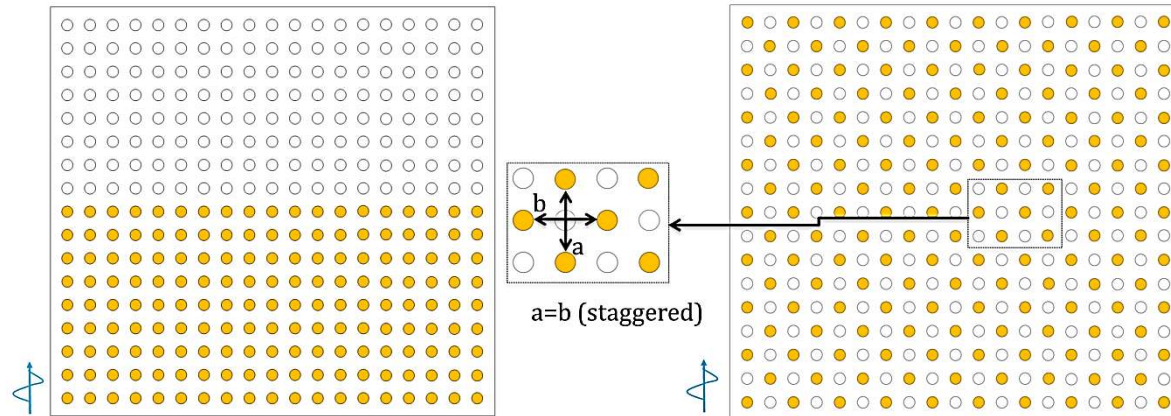


Figure 3.19 (a) Vertical configuration with porosity 0.80, width 0.35 m and uniform placement of the elements (b) Vertical configuration with porosity 0.90, width 0.68 m and staggered placement of the elements

The number of elements is not exactly the same in all cases. However, this does not make a difference in the porosity calculation. In all three cases the porosity increases from 0.80 to 0.90. Next, to exclusively test the effect of the width of the structure, the three latter cases that have a width of 0.68 m are used with a width of 0.35 m (shown in Figures 3.20-3.22). This way the porosity and arrangement are kept constant.

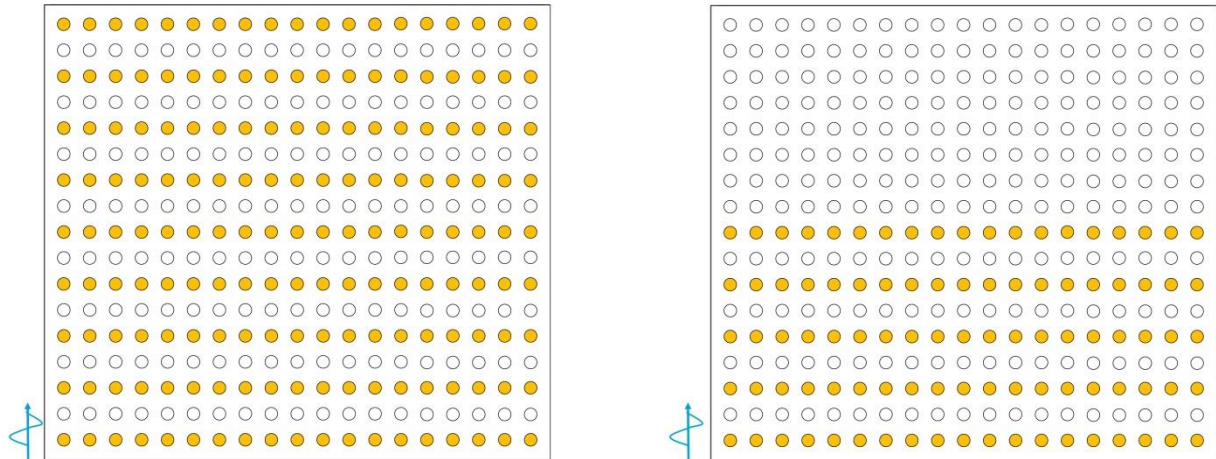


Figure 3.20 Vertical configurations with porosity 0.90 and the longitudinal spacing between the elements is larger than the lateral spacing between the elements (a) width is 0.68 m (b) width is 0.35 m

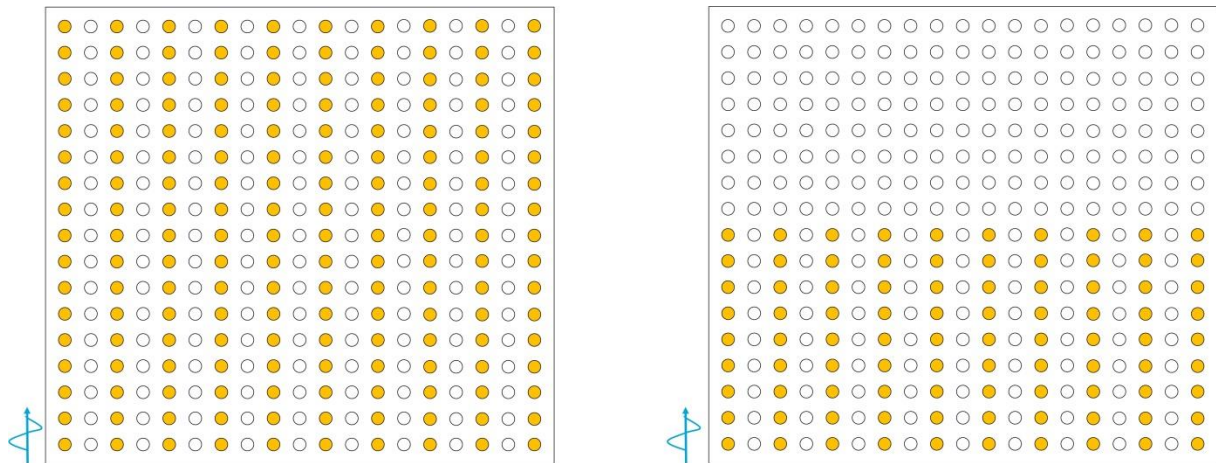


Figure 3.21 Vertical configurations with porosity 0.90 and the lateral spacing between the elements is larger than the longitudinal spacing between the elements (a) width is 0.68 m (b) width is 0.35 m

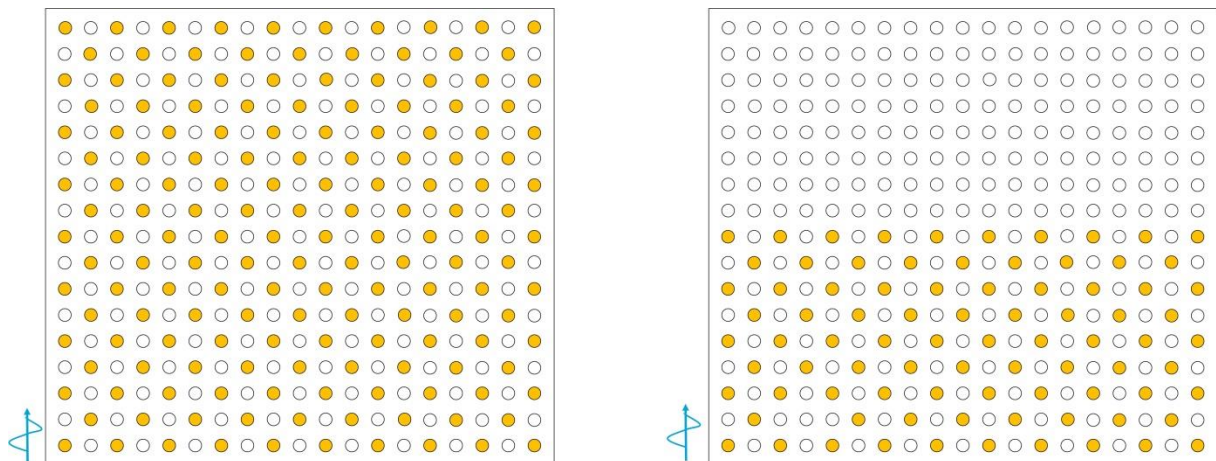


Figure 3.22 Vertical configurations with porosity 0.90 and staggered placement of the elements (a) width is 0.68 m (b) width is 0.35 m

4. Results of experiments

The present chapter provides an overview of the results of the experiments. In the first section, a description of how the measured data is processed is given. In the second section, the measured reflection, transmission and dissipation are shown as a function of the five wave cases. This is shown for all sixteen configurations. The five wave cases can be described by various dimensionless parameters. The effect of the different configurations (orientation, porosity, width, arrangement, etc.) on each parameter is studied, in order to select one of them for further analysis. This choice is (partly) based on the parameter that correlates best with the wave dissipation and is explained in the third section. The final section shows the effect of the different configurations on the wave dissipation as a function of the chosen wave parameter. The section only provides a description of the results. In Chapter 5 the results are analysed, in which (possible) explanations are given.

4.1 Data processing

The results of the 16 different configurations are presented in tables in Appendix E. For all configurations the incoming, reflected and transmitted wave heights are measured for 5 different wave cases. Also, the reflection from the wave absorber is measured. In order to distinguish the incoming wave heights from the reflected wave heights, the method presented by Goda and Suzuki (1976) is used. The method is described in more detail in Appendix C. From the measurements of the incoming, transmitted and reflected wave heights, the wave dissipation (in terms of energy) is determined. This is done by using the wave energy balance, presented in Equations 4.1-4.4. A more detailed derivation is shown in Section 2.2.1.

$$E_i = E_r + E_{diss} + E_t \quad [4.1]$$

$$\left(\frac{H_i}{H_i}\right)^2 = \left(\frac{H_r}{H_i}\right)^2 + \left(\frac{H_{diss}}{H_i}\right)^2 + \left(\frac{H_t}{H_i}\right)^2 \quad [4.2]$$

$$1 = C_r^2 + C_{diss}^2 + C_t^2 \quad [4.3]$$

$$C_{diss}^2 = 1 - \left(\frac{H_r}{H_i}\right)^2 - \left(\frac{H_t}{H_i}\right)^2 \quad [4.4]$$

4.2 Measured reflection, dissipation and transmission

The incoming wave energy is translated into reflection, dissipation and transmission. In order to see the distribution of the three components all data are plotted in Figure 4.1. These data include the tests of the 16 different configurations, which are tested under five different wave cases. The five wave cases are numbered from 1 to 5, going from the shortest (wave case 1) to the longest waves (wave case 5), as shown in Figure 4.2. From the plot it becomes clear that as a percentage of the incoming wave energy, reflection varies between 0.2-8.6%, transmission varies between 38-88% and dissipation varies between 11-58%. Generally the reflection is low and constant over the different wave cases. The transmission increases for longer waves, following that the dissipation decreases.

The reflection from the wave absorber is low in all cases ($<1\%$) and therefore the data is not corrected for this. Furthermore, each measurement has been performed twice to see whether results deviate from each other. As discussed in Section 3.4, the wave gauges have an accuracy of ± 1 mm. The tables presented in Appendix E show that the wave heights of the two repeated measurements deviate from each other with ± 1 mm. This is in agreement with the accuracy of the wave gauges.

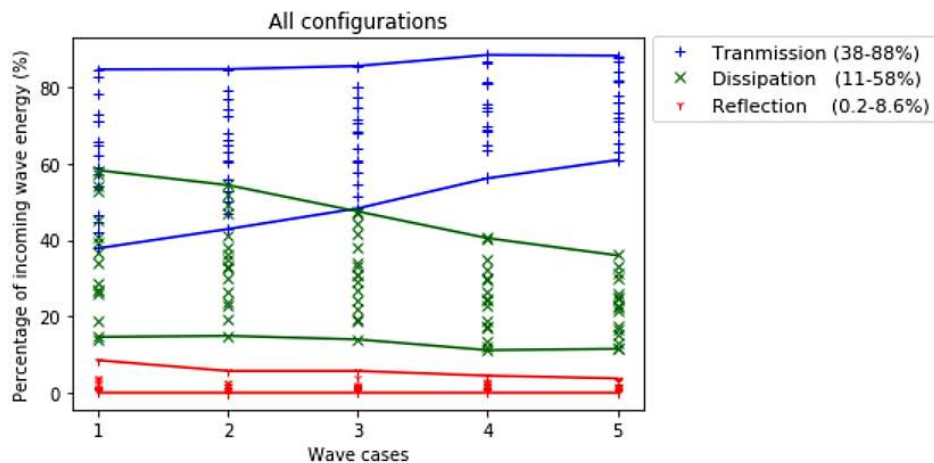


Figure 4.1 Reflection, transmission and dissipation from wave case 1 to wave case 5

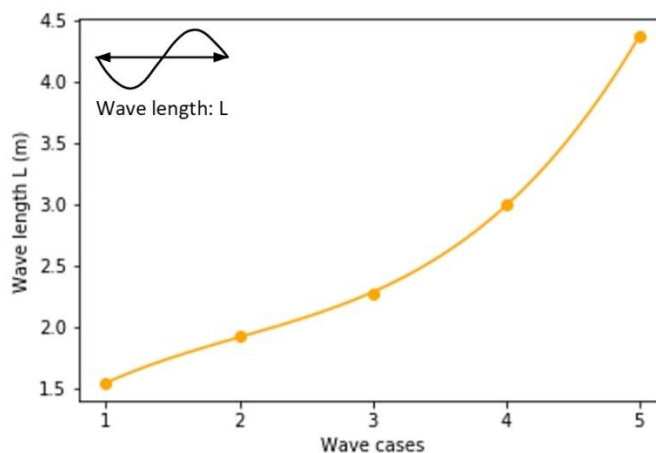


Figure 4.2 Wave length for the five different wave cases in which case 1 is the shortest wave and case 5 is the longest wave

4.3 Correlation wave dissipation and dimensionless wave parameters

The plot in Figure 4.1 shows the measurements of the reflection, transmission and dissipation against the five wave cases, going from short (wave case 1) to longer waves (wave case 5). The wave cases can be described by various dimensionless parameters, including the:

- Wave steepness: H/L
- Wave number multiplied by the water depth: kd
- Width of the structure over the wave length: w/L
- Keulegan-Carpenter number: KC
- Reynolds number: Re
- Froude number: Fr

As reflection is low (<3.5%) and constant for the different wave conditions, there is almost a one-to-one relationship between transmission and dissipation. For the latter reason and to avoid plots that become too abstract, only the dissipation is used. However, in some cases reflection is higher than 3.5%. These cases are looked at in more detail in the next section.

The plots of the dissipation rates against the various dimensionless wave parameters are shown in Figure 4.3. All of the 16 different configurations are included, represented by one specific colour. It generally holds that dissipation increases for increasing H/L , kd and w/L and decreases for increasing KC , Re and Fr .

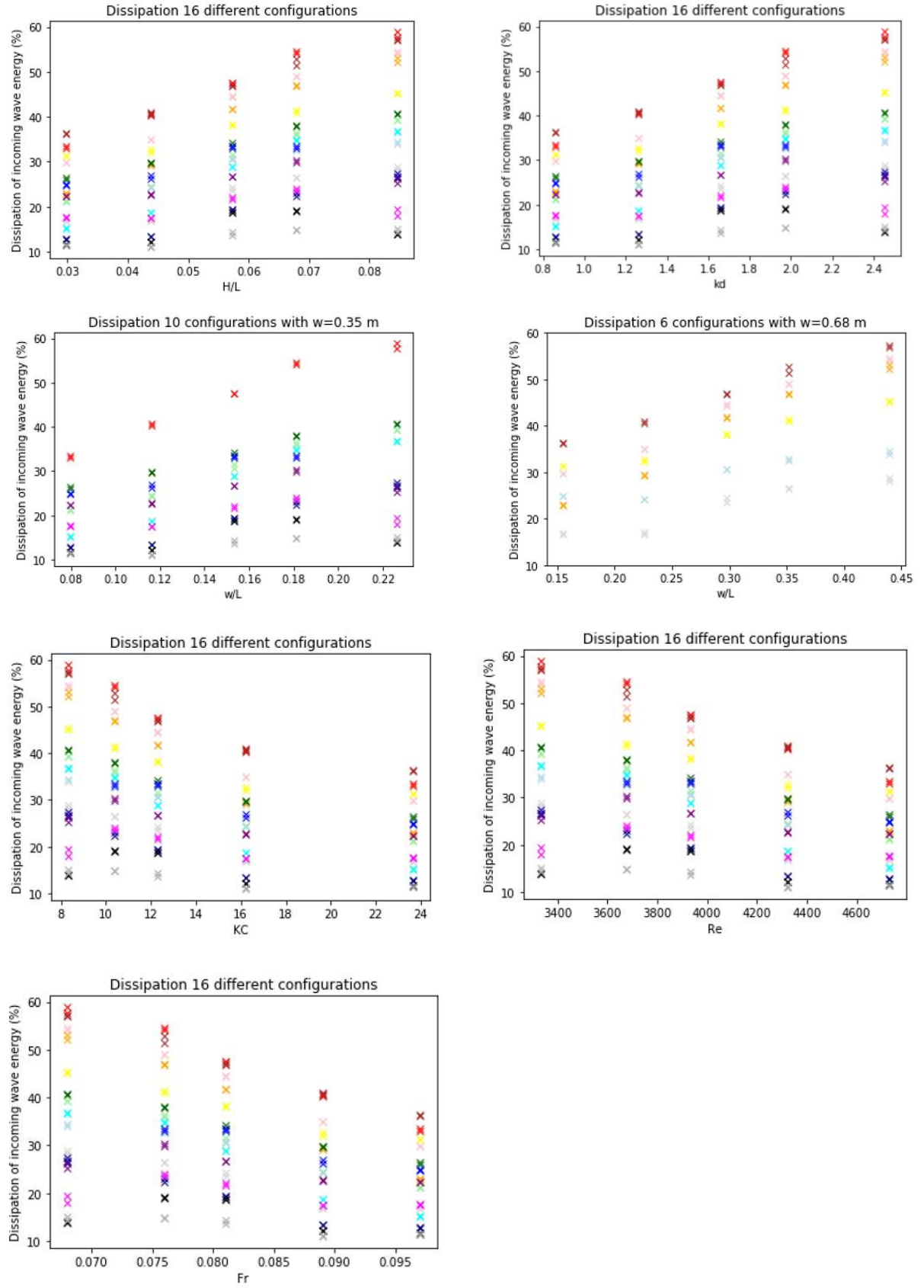


Figure 4.3 Plots of the dissipation rates of all configurations against various dimensionless parameters including the (a) Wave steepness (b) Wave number multiplied by the water depth (c) Width of the structure over wave length with width of 0.35 m (d) Width of the structure over wave length with width of 0.68 m (e) Keulegan Carpenter number (f) Reynolds number (g) Froude number

To have a better look at the effect of each of the 16 different configurations, one of the relationships between the dissipation and dimensionless wave parameter is analysed in more detail. This choice is (partly) based on the parameter that correlates best with the measured dissipation. In order to identify this, the correlation between the wave dissipation and the six different wave parameters is determined for each configuration. A trend line is made between the dissipation rate and the dimensionless parameter for each configuration. Different trend types are tried out, including a:

- Exponential trend: $y = ae^{bx}$
- Linear trend: $y = ax + b$
- Logarithmic trend: $y = a\ln(x) + b$
- Polynomial trend: $y = ax^2 + bx + c$
- Power trend: $y = ax^b$

In the different trend types, y is the wave dissipation and x the dimensionless parameter. The coefficient a , b and c are determined by using the least squares method. In this method, a , b , and c are chosen such that the difference between the measured data and the trend line is minimal. To see which of the trend line correlates best with the data, the correlation coefficients are determined, with X representing the data and Y representing the fitted trend line:

$$\text{Correl}(X, Y) = \frac{\sum(x - \bar{x})(y - \bar{y})}{\sqrt{\sum(x - \bar{x})^2 \sum(y - \bar{y})^2}}$$

A correlation coefficient squared (R^2) with a value of one represents a perfectly fitted trend line. The polynomial trend provides the best fit for all parameters and is subsequently used to analyse the different configurations. Next, the 16 different configurations are split up by their effects:

- Porosity
- Spreading out the same number of elements over a larger area
- Arrangement of the elements
- Width of the structure

The results of the correlation between the wave dissipation and the wave parameters are shown for each effect in Figures F1-F4 in Appendix F. What can be concluded from the plots is that the correlation between the wave dissipation and the five dimensionless wave parameters for all horizontal configurations is higher in comparison to the vertical ones. The correlation coefficient squared (R^2) is close to one in all cases. The same holds for the configurations that are vertically orientated that have a width of 0.68 m (independent of the arrangement or porosity). For the vertical configurations that have a width of 0.35 m, the correlation is lower as R^2 varies between 0.33 and 0.77. In these cases the correlation for KC is lower in comparison to the other parameters. Reason for this could be that the KC -range is not very wide as it varies from 8-23. The other five parameters (Re , Fr , H/L , kd and w/L) have comparable values of R^2 for all configurations. Therefore, the choice of parameter is not an obvious one.

As shown in Section 2.3.2, the wave dissipation can be expressed in terms of an empirical drag coefficient C_d . In Chapter 5 these coefficients are derived. Table 2.2 shows an overview of previous studies on the drag coefficient as a function of either Re or KC . In order to make comparisons with previous studies (Chapter 5), it would be useful to choose one of these parameters. However, for now the choice is made to use parameter kd . This parameter determines the orbital velocities. Since the horizontal structures obstruct both vertical and horizontal velocities, kd considerably affects the drag forces and therefore the dissipation through the structures. A more detailed explanation is provided in Section 5.1.1.

4.4 Wave dissipation for different configurations

The present section only provides a description of the results. In Chapter 5 the results are analysed, in which (possible) explanations are given.

4.4.1 Porosity effect

Figure 4.5 shows four cases in which the effect of two porosities ($n=0.80$ and $n=0.94$) is illustrated for both the vertical (shown left) and horizontal orientations (shown right). Looking at the horizontal case with a porosity of $n=0.80$, the wave dissipation increases when the waves become shorter (which is for increasing kd , as indicated in Figure 4.4). The vertical case shows a different trend, in which there is a maximum value for the wave dissipation at $kd=2.0$. Furthermore, the wave dissipation for the horizontal case is higher than the vertical one, with a factor varying from 1.3-2.2 depending on kd .

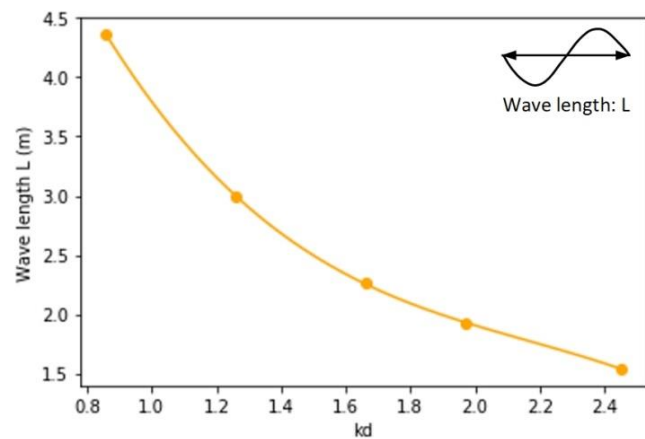
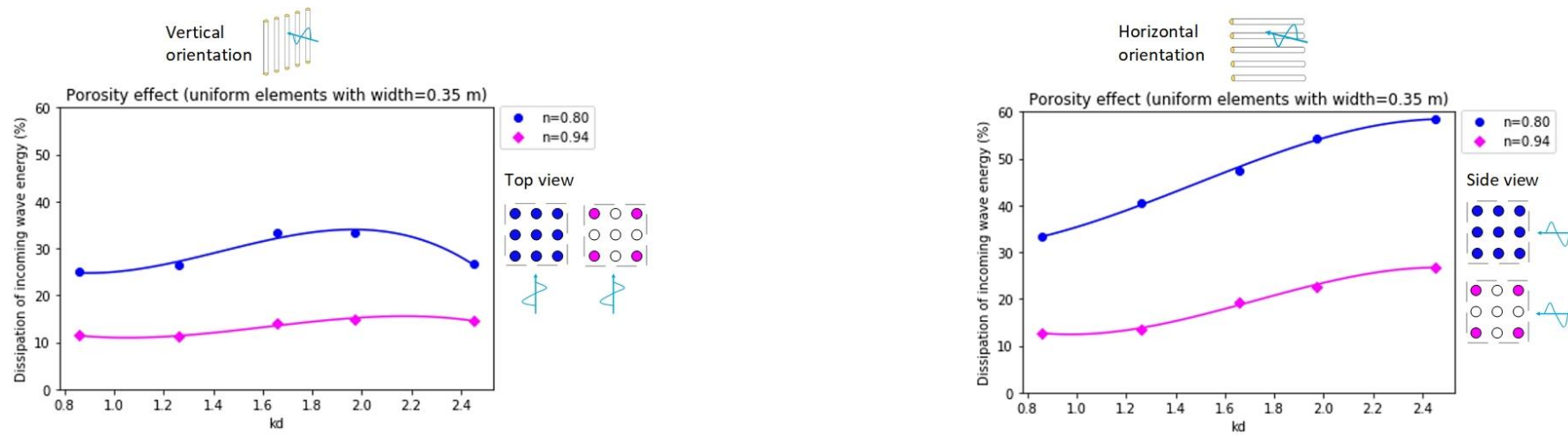
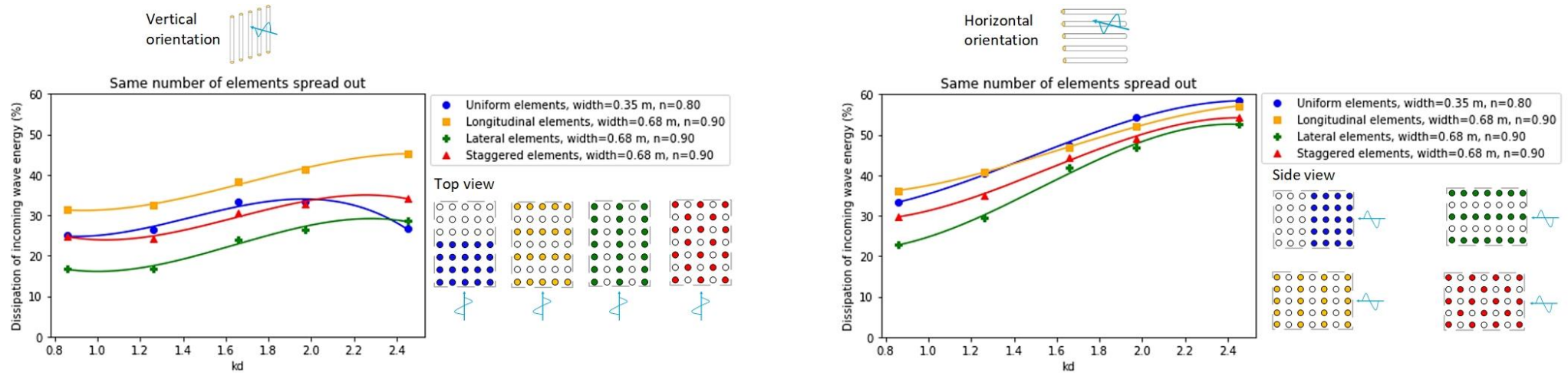


Figure 4.4 Wave length L in meters as a function of kd

For the horizontal orientation with the higher porosity of $n=0.94$, the wave dissipation also increases when the waves become shorter. The increase is milder in comparison to the lower porosity case. Moreover, the wave dissipation for the higher porosity case is smaller compared to the lower porosity case. However, as the waves become longer (decreasing kd), the difference in dissipation becomes smaller.

The two different porosities in the vertical orientation do not show similar trends. For the higher porosity the dissipation increases only slightly (with 3%) as the waves become shorter, while for the lower porosity there is a relative maximum. After this maximum is reached, the wave dissipation decreases as the waves become shorter. Reason for this decrease in dissipation is the increase in reflection (up to 8.6% for the shortest waves). This (relative) large increase in reflection only holds for the vertical orientation with the lower porosity. For the higher porosity case the increase in reflection is smaller, as it only goes up to 1.2%. The same holds for the horizontal elements, which have reflection rates going up to 3.5%.

Figure 4.5 Plots of dissipation rates against kd for two different porosities. Vertical orientation (left) Horizontal orientation (right)Figure 4.6 Plot of dissipation rates against kd for three different ways of spreading out the elements. Vertical orientation (left) Horizontal orientation (right)

4.4.2 Effect of spreading out the same number of elements over a larger area

Figure 4.6 shows the effect of spreading out the same number of element over a larger area. The vertical orientations are shown left and the horizontal ones are shown right. The elements are placed in three different ways, which is also indicated in the figure. The three different ways include spreading out the elements in such a way that:

- the longitudinal spacing between the elements is larger than the lateral spacing between the elements (referred to as the longitudinal elements).
- the lateral spacing between the elements is larger than the longitudinal spacing between the elements (referred to as the lateral elements).
- the elements are placed in a staggered position (referred to as the staggered elements).

In the reference case (vertical elements, indicated in blue), there is maximum wave dissipation at $kd=2.0$. In all the cases in which the elements are spread out, the trend changes, as the wave dissipation increases as the waves become shorter (increasing kd).

For the longitudinal elements, there is an increase in wave dissipation with a factor 1.2-1.7 (depending on kd) in comparison to the reference case. For the staggered elements, there is only higher wave dissipation when $kd>2.0$. Finally, for the lateral elements, the wave dissipation decreases. Only for $kd>2.35$ the dissipation increases slightly.

The behaviour of the horizontal cases is different from the vertical ones. The trend lines in all four cases are similar, as the wave dissipation increases for shorter waves. Spreading out the elements over a larger area only leads to an increase in wave dissipation for the longitudinal elements. However, this only holds for $kd<1.25$, in which the wave dissipation increases until a factor of 1.1. For the staggered and lateral elements, the wave dissipation decreases in comparison to the reference case.

4.4.3 Effect of arrangement between the elements and width

The upper graphs in Figure 4.7 show the effect of the different arrangements between the elements with a width of 0.35 m. The lower graphs show the same effect, but in these cases the width is 0.68 m. The vertical orientations are shown left and the horizontal ones are shown right.

Looking at the half width cases, the longitudinal elements provide the maximum dissipation, followed by the staggered and lateral elements. The vertical elements dissipate less energy (maximum values of 30%) and the differences between configurations are quite similar for the different wave cases. The dissipation rates are higher for the horizontal orientation (maximum values of 40%). However, for the shortest waves (highest kd values) all the arrangements dissipate a similar amount of energy, as when the waves become longer (lower kd values) the differences are larger.

The same trends are shown for the full width cases. Moreover, an increase in width leads to additional dissipation in all cases. Looking at the effectiveness of increasing the width for the vertical orientation, the following can be concluded. For the shorter waves (higher kd values), an increase in width with a factor 2 leads to an increase in wave dissipation with a factor 1.6. As the waves become longer (lower kd values), this factor is 1.4. For the horizontal orientation, the increase in wave dissipation is a factor 1.4 for both short and long waves.

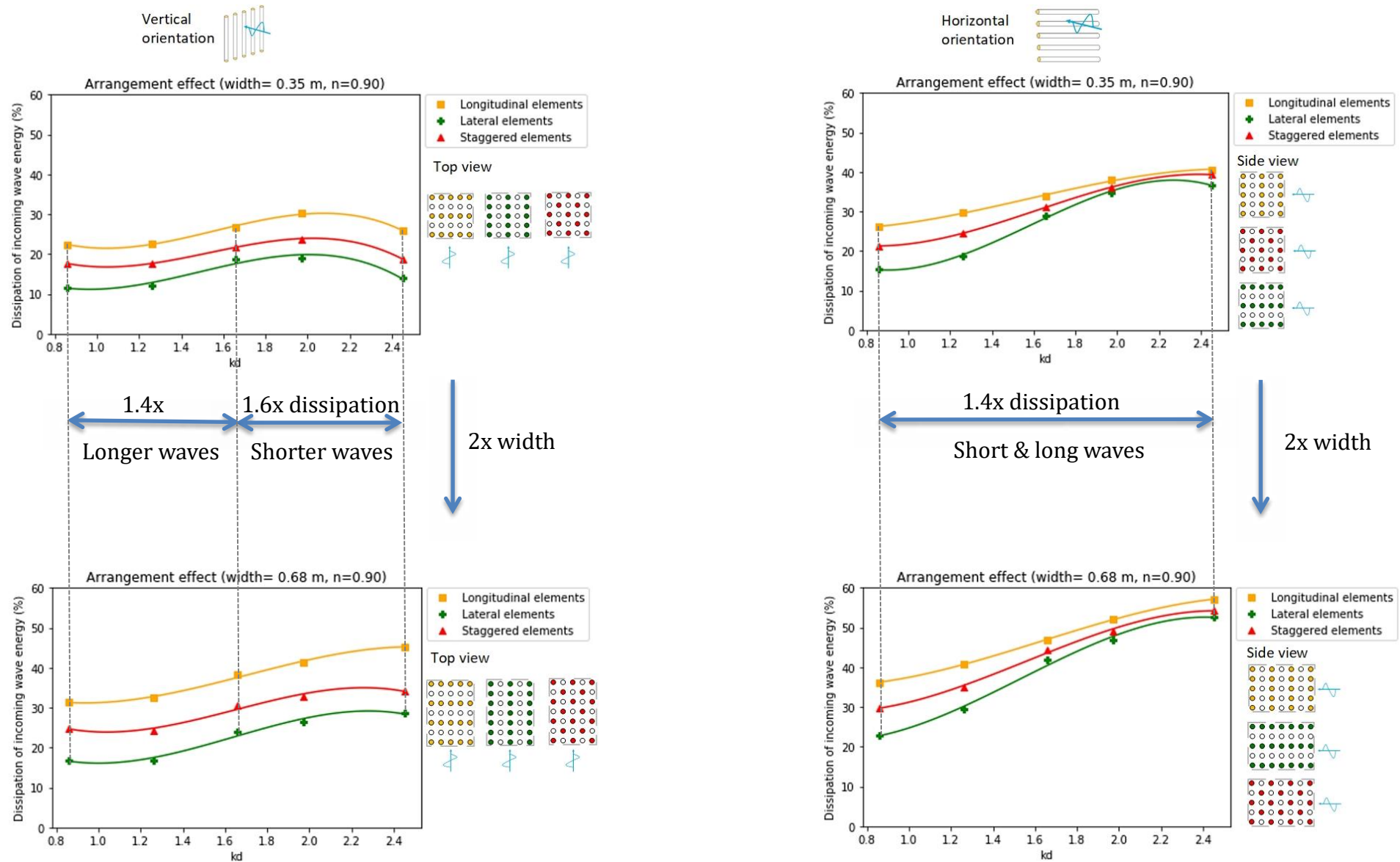


Figure 4.7 Plot of dissipation rates against kd for three different ways of arrangement. Vertical orientation with width=0.35 m (upper left), horizontal orientation with width=0.35 m (upper right), vertical orientation width=0.68 m (lower left) and horizontal orientation width=0.68 m (lower right).

The results of the half width and full width structure are combined, to show how the wave dissipation changes through the structure. An impression of the wave transformation is shown in Figure 4.8, with the vertical orientation shown left and the horizontal orientation shown right. At location $x=0$ m, it is assumed that no wave energy is dissipated. At location $x=0.35$ m the dissipation rates of the half width structure are used and at location $x=0.68$ m the dissipation rates of the full width structure are used.

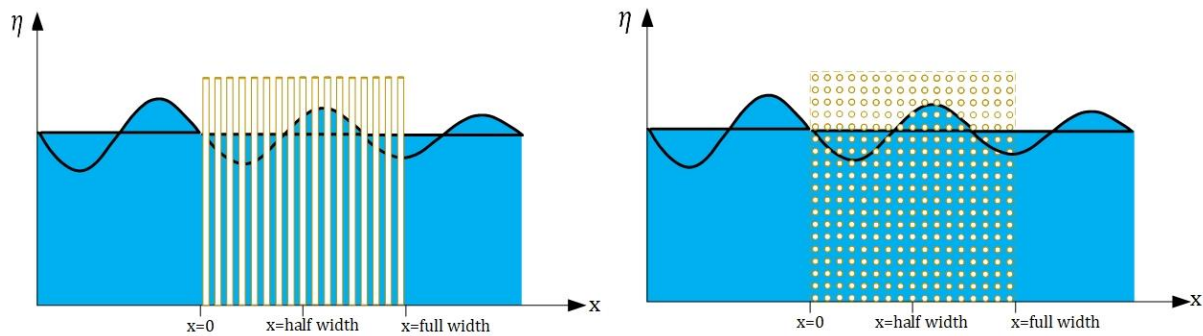


Figure 4.8 Wave transformation through structure. Vertical orientation (left) Horizontal orientation (right)

The results of the structures with vertical orientation are shown in Figure 4.9. What can be concluded from the plots is that in nearly all wave cases (expressed in different wave lengths), most of the dissipation takes place in the first half of the structure. This percentage is around 70%, meaning that 30% of the total dissipation takes place in the second half of the structure. This holds for all arrangements (longitudinal, lateral and staggered elements). Only in case of the shortest wave (marked black), around 50-55% of the total wave dissipation takes place in the first half of the structure, following that 45-50% takes place in the second half. Again this trend is seen for all arrangements.

The same plots are made for the structures with horizontal orientation, as shown in Figure 4.10. The difference with the vertical orientation is that for all wave cases, most of the dissipation takes place in the first half of the structure. This percentage is also around 70%, following that 30% of the total dissipation takes place in the second half of the structure. Again this holds for all arrangements.

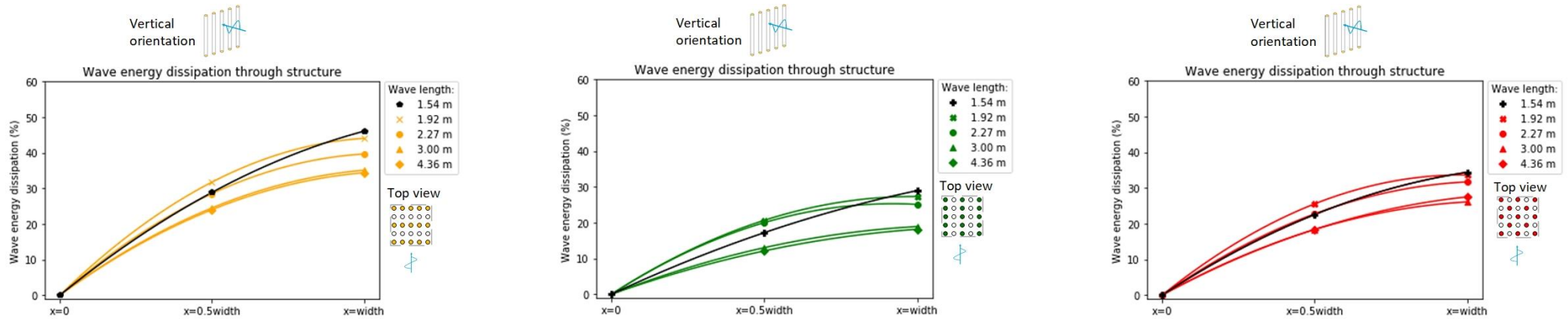


Figure 4.9 Wave energy dissipation through structure with vertical orientation. Longitudinal elements (left), lateral elements (middle) and staggered elements (right).

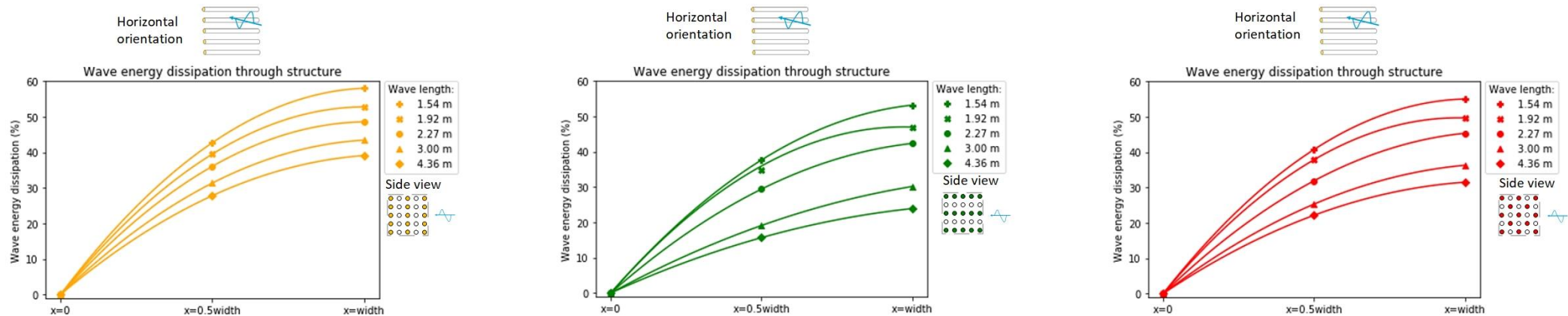


Figure 4.10 Wave energy dissipation through structure with horizontal orientation. Longitudinal elements (left), lateral elements (middle) and staggered elements (right).

5. Analysis of results

In the present chapter the results are analysed. Firstly, the drag coefficients of each configuration are derived using the calibration method on Dalrymple's analytical model for wave dissipation. Secondly, the drag coefficients of each effect (orientation, width, arrangement, etc.) are compared to each other to see whether their relative values are as expected. Thirdly, the results are also compared to other research works to see how much they relate to each other under comparable conditions. Finally, it is shown how the results obtained in the flume relate to the prototype.

5.1 Calibrated drag coefficients for different configurations

As derived in Section 2.2.3, an analytical expression can be found for the transmission coefficient (Dalrymple, 1984):

$$C_t = \frac{H_t}{H_i} = \frac{1}{1+\alpha w} \quad [5.1]$$

H_t = transmitted wave height (m)

H_i = incoming wave height (m)

w = structure width (m)

$$\alpha = \frac{E_d}{a^2 \rho g c_g} \quad [5.2]$$

E_d = dissipated wave energy per unit area (J/m²)

a = amplitude of the incoming wave (m)

c_g = wave group velocity (rad/m)

$$E_{d,horizontal} = F_{d,horizontal} \cdot u = \frac{2}{3\pi} \rho C_d D \frac{N}{k} \cdot \frac{(\sinh(kd)^3 + 3\sinh(kd))}{3 \cosh(kd)^3} \left(\frac{gk}{\omega}\right)^3 a^3 \quad [5.3]$$

$F_{d,horizontal}$ = the horizontal drag force (N)

u = the horizontal velocity due to the wave motion (m/s)

C_d = drag coefficient per element (-)

N = number of elements per unit area (m⁻²)

D = diameter cylinder (m)

k = the wave number (rad/m)

ω = the angular frequency (rad/s)

d = the water depth (m)

With the measured incoming and transmitted wave heights, the drag coefficient can be found for each wave case. Note that this is the drag coefficient averaged over the total number of elements (C_d per element). Again, the configurations are split up by the following effects:

- Orientation (horizontal vs. vertical elements)
- Porosity
- Arrangement of the elements
- Spreading out the same number of elements over a larger area
- Width of the structure

5.1.1 Orientation effect (horizontal vs. vertical elements)

Figure 5.1 shows the calibrated drag coefficients of all the tested effects as a function of kd . In terms of kd , the three different water regions are defined as follows (Ippen 1966):

For deep water:	$kd \gg 1$
For intermediate water:	$kd \approx O(1)$
For shallow water:	$kd \ll 1$

The vertical elements are shown left and the horizontal elements are shown right. For all tested effects, the drag coefficients of the vertical elements are more constant for varying kd in comparison to the horizontal ones. For the vertical elements, the drag coefficient varies from 1-3 depending on the configuration. In case of the horizontal elements, the drag varies from 3-4 for the higher kd values (deeper water) and from 1-3 for the lower kd values (shallower water). Therefore, as kd decreases the values of the drag coefficients of the horizontal and vertical elements become more similar to each other.

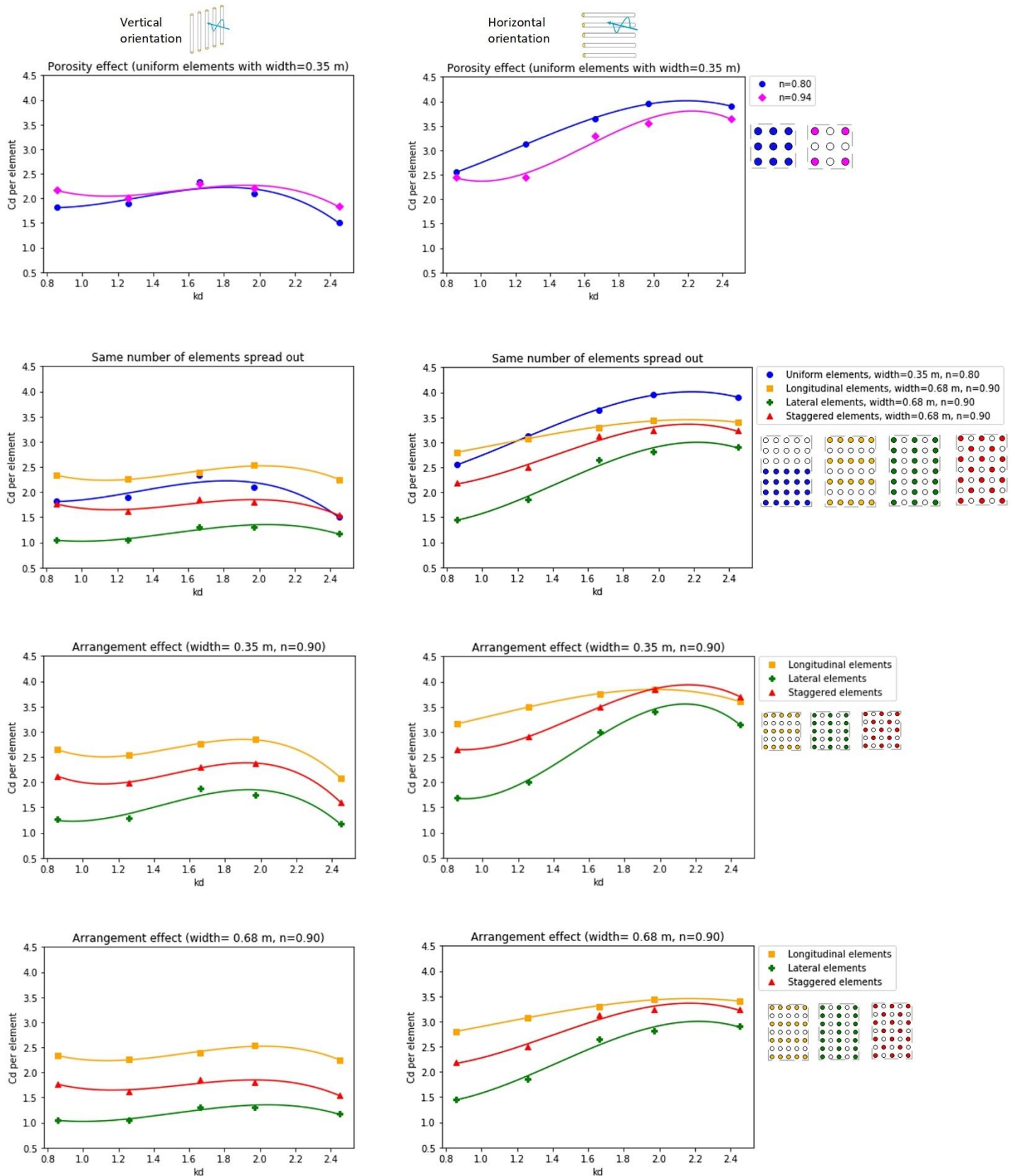


Figure 5.1 Calibrated drag coefficient as a function of kd (all configurations). Vertical orientations (left) Horizontal orientations (right)

For the horizontal elements, not only the horizontal drag force, but also the vertical drag force plays a role (shown in Figure 5.2).

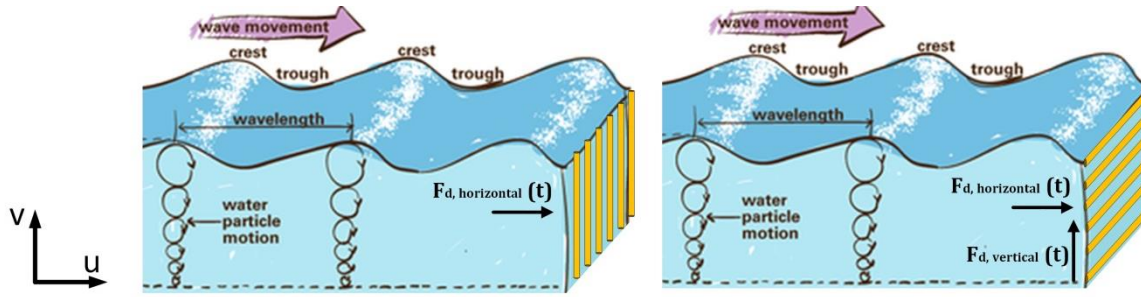


Figure 5.2 Drag forces on vertical elements (left) and horizontal elements (right). Adapted from: (Maya B., n.d.).

Dalrymple (1984) derived the wave energy dissipation by an array of vertical cylinders from the work by the horizontal drag force (derivation shown in Section 2.3.2):

$$E_{d, horizontal} = F_{d, horizontal} \cdot u = \frac{2}{3\pi} \rho C_d D \frac{N}{k} \cdot \frac{(\sinh(kd)^3 + 3\sinh(kd))}{3 \cosh(kd)^3} \left(\frac{gk}{\omega}\right)^3 a^3 \quad [5.3]$$

Equation 5.3 only considers the energy dissipation due to the horizontal velocity component (u), while the measured dissipation is caused by both the horizontal and vertical component:

$$E_{d, total} = E_{d, horizontal} + E_{d, vertical} \quad [5.4]$$

In which $E_{d, vertical}$ is the work done by the vertical drag force:

$$E_{d, vertical} = F_{d, vertical} \cdot v = \frac{1}{2} \rho C_d D v |u| N \cdot v \sim |u| v^2 \quad [5.5]$$

$F_{d, vertical}$ = the vertical drag force (N)
 v = the vertical velocity due to the wave motion (m/s)

When there is dissipation caused by the vertical velocity component (v), it is calibrated into the (horizontal) drag coefficient which leads to higher values. Vertical dissipation starts playing a role when the vertical velocities are relatively high. That is the case in deep water ($kd \gg 1$) relative to shallow water ($kd \ll 1$) as shown in Figure 5.3.

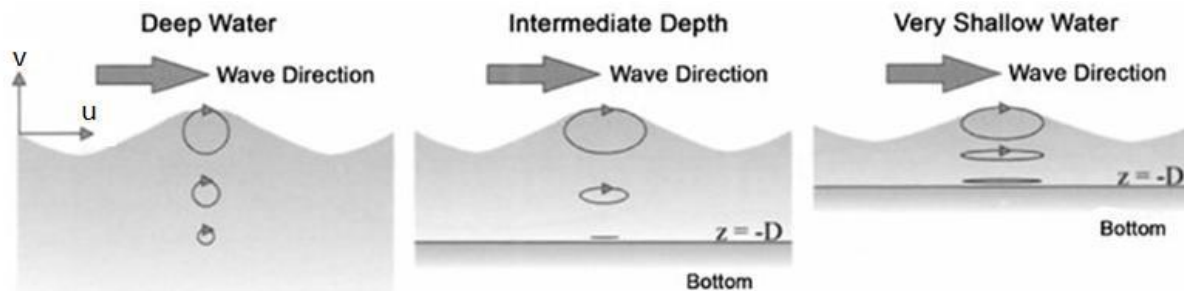


Figure 5.3 Deep, intermediate and shallow water depths. Adapted from: (Lee, 2010).

Figure 5.4 shows the depth integrated velocity amplitude for both the horizontal (u) and the vertical (v) velocity as a function of kd . The derivation of the velocity amplitudes is shown in Section 2.1.4. The figure shows that the vertical velocities are relatively high for higher kd values. Due to the higher vertical velocities, there is also wave dissipation that is caused by this component. The additional wave dissipation is calibrated into the (horizontal) drag coefficient, leading to higher values (3-4). As kd decreases, the vertical velocities become smaller. In that case the drag coefficient of the horizontal elements decreases to values from 1-3. These values are the same as the values of the vertical elements. Therefore, as the water becomes shallower, the dissipation rates of the horizontal and vertical elements become more similar to each other.

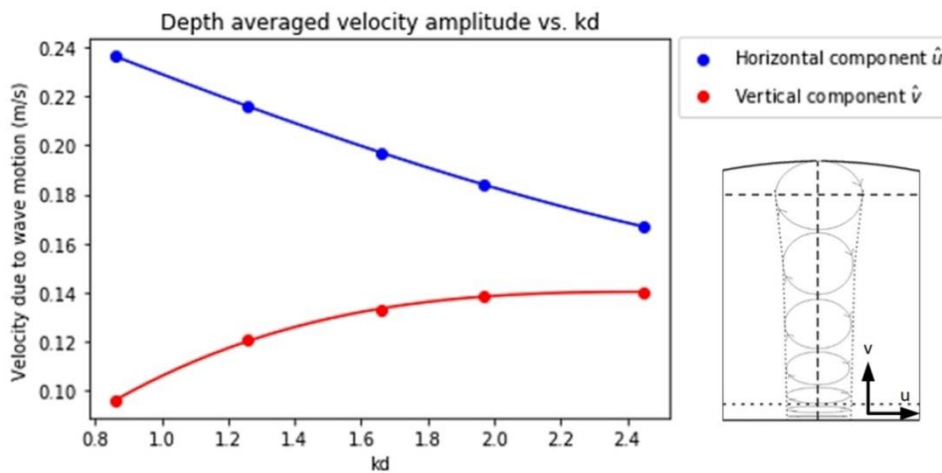


Figure 5.4 Depth integrated velocity amplitude as a function of kd

5.1.2 Porosity effect

In previous literature, the drag coefficient has been determined for arrays of cylinders with different densities. Nepf (1999) showed that the bulk drag coefficient (C_d per element) decreases with increasing density (ad), as shown in Figure 5.5. This has been performed in steady flow, rather than oscillatory flow. Suzuki and Arikawa (2010) performed numerical modelling tests for cylinders under oscillatory flow, also showing that the drag coefficient decreases with increasing density (shown in Figure 5.6). Considering these results, it is expected that the C_d per element decreases for increasing density. A higher density means a lower porosity. Therefore, the drag coefficient would be lower in the lower porosity case ($n=0.80$) in comparison to the higher porosity case ($n=0.94$). The drag coefficient (per element) is plotted as a function of Re for the two different porosities (shown in Figure 5.7).

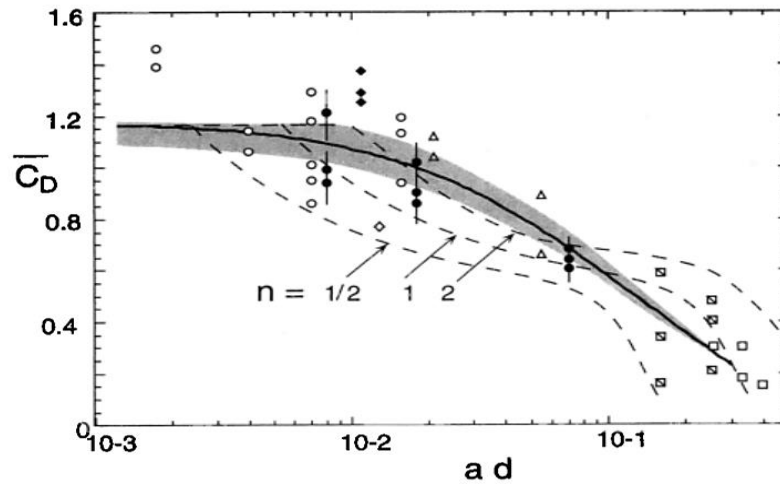
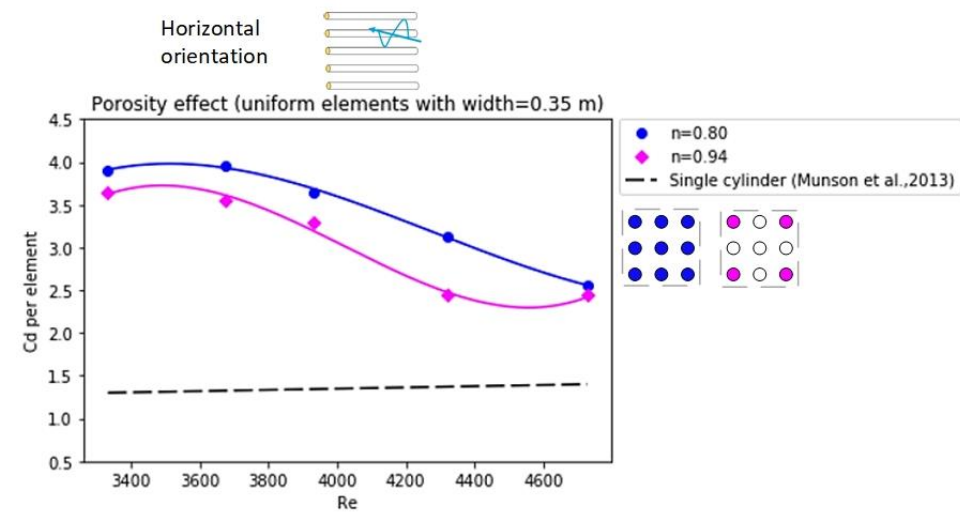
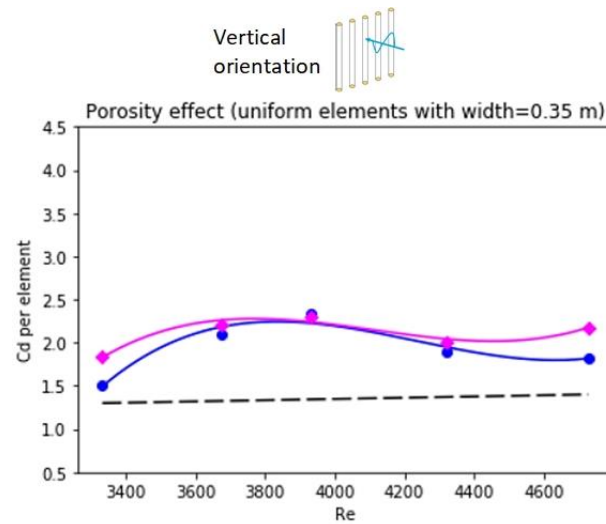


Figure 5.5 Bulk drag coefficient for different densities of elements (Nepf, 1999)

Drag coefficient for a single cylinder and bulk drag coefficients in the different densities for multiple cylinders.	
CASE	C_D or Bulk drag coefficient
Single cylinder	1.4
	1.39
	1.40
	1.22

Figure 5.6 Arrays of cylinders with three densities and their drag coefficient (Suzuki and Arikawa, 2010)

Figure 5.7 Drag coefficient against Re for two different porosities. Vertical orientation (left) Horizontal orientation (right)

As discussed in Section 4.3, Re has a higher correlation with the measured wave dissipation than KC (shown in Figure 5.8). For that reason it is chosen to plot the drag coefficient against Re rather than KC .

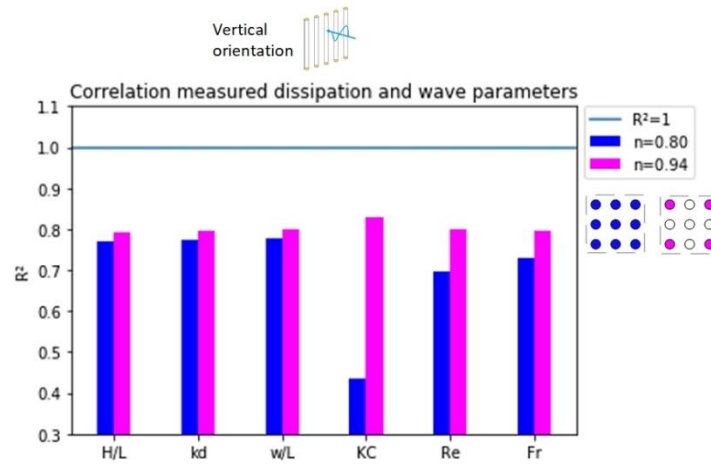


Figure 5.8 Correlation wave dissipation and various dimensionless wave parameters

As expected, the drag coefficients of the vertical elements are (slightly) higher in the higher porosity case. However, in the case of the horizontal elements the results are quite unexpected, as the drag coefficient is higher for lower porosity. As Re increases, the drag coefficients start to converge. The lower Re numbers have higher kd values (shown in Figure 5.9). As mentioned in the previous section, for higher kd values the vertical velocities are relatively high (shown in Figure 5.4). The vertical velocities can be reduced more effectively by the horizontal elements, as they have more exposure to the vertical velocity component in comparison to the vertical elements. Based on the results, it could be possible that the vertical velocities are reduced more in the higher porosity case, leading to lower drag coefficients.

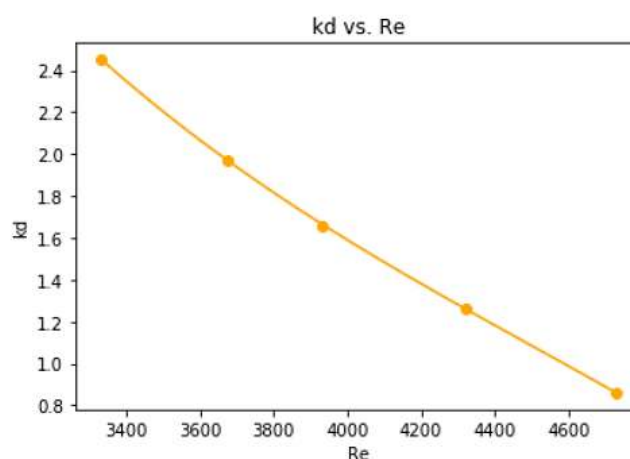


Figure 5.9 kd as a function of Re

5.1.3 Arrangement effect

Previous studies have shown the effect of the arrangement of elements on the drag coefficient. Bokaian and Geoola (1984) tested two elements with different lateral (T) and longitudinal spacing (L) in steady flow (shown in Figure 5.10). In these tests the drag coefficient of cylinder B has been determined.

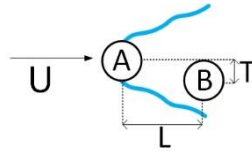


Figure 5.10 Cylinders A and B with varying lateral (T) and longitudinal (L) spacing in steady flow

For decreasing lateral (T) and longitudinal spacing (L), the drag coefficient of cylinder B decreases as shown in Figure 5.11. This results from two properties of the wake. The first one is that cylinder B experiences a lower velocity (due to the reduction in the wake). The second is that the turbulence, which is contributed by the wake, delays the point of separation on the downstream cylinder. This results in a lower pressure difference along the trailing cylinder and therefore a lower drag coefficient.

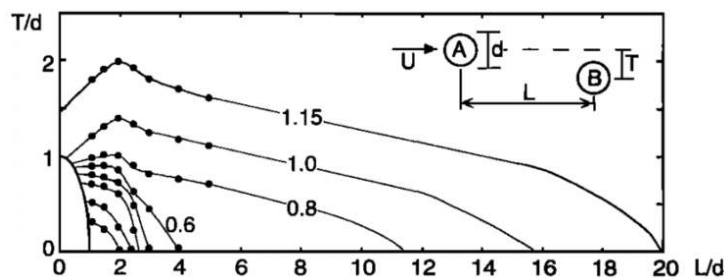


Figure 5.11 Drag coefficient cylinder B for varying lateral and longitudinal spacing (Nepf, 1999)

Considering these results, it is expected that the C_d per element decreases as the elements become more sheltered. Figure 5.12 shows the three different arrangements that are tested: the longitudinal elements (left), the staggered elements (middle) and the lateral elements (right). The longitudinal elements are most exposed and are therefore expected to have the highest drag coefficients. The lowest drag coefficients are expected to belong to the lateral elements, as these are most sheltered. The staggered elements are less exposed in comparison to the longitudinal elements and less sheltered in comparison to the lateral elements. Therefore, the values of the drag coefficients of the staggered elements are expected to be in between the ones for the longitudinal and lateral elements.

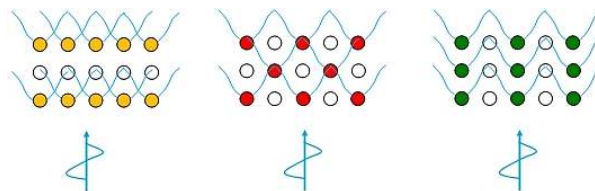


Figure 5.12 Longitudinal elements (yellow), staggered elements (red) and lateral elements (green)

The results of the different arrangements are shown in Figure 5.13. For both the vertical and horizontal elements the results are as expected, as the highest drag coefficients belong to the longitudinal elements, followed by the staggered and lateral elements.

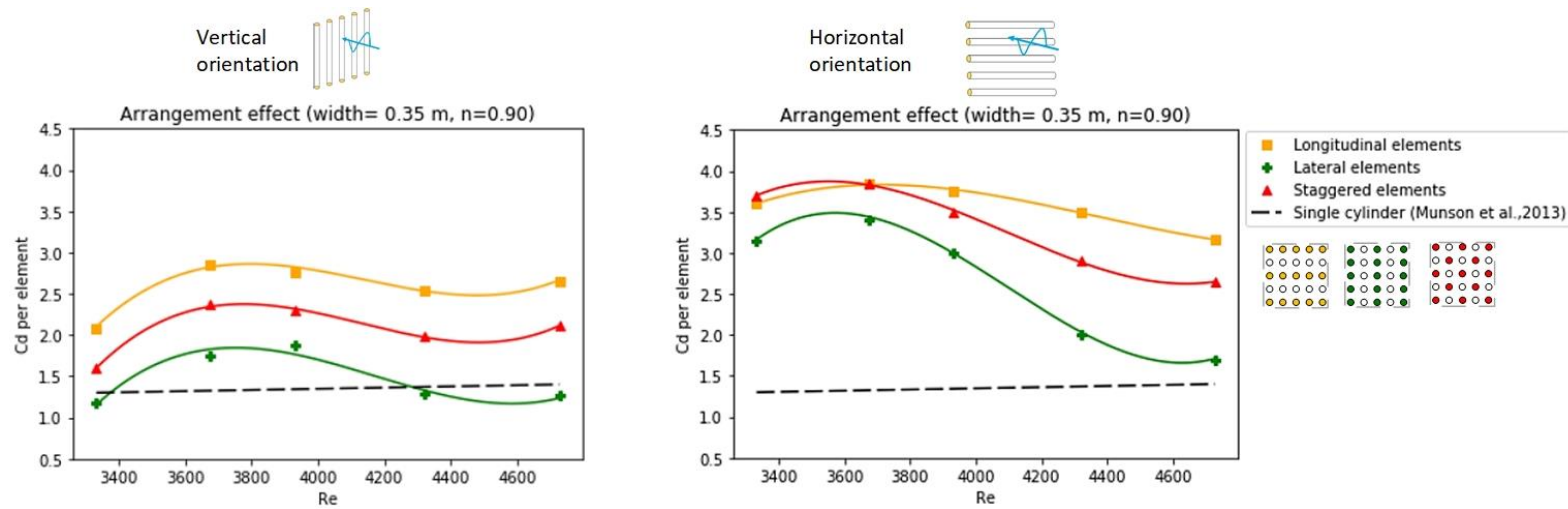


Figure 5.13 Drag coefficient against Re for three different ways of arrangement with width=0.35 m. Vertical orientation (left) Horizontal orientation (right)

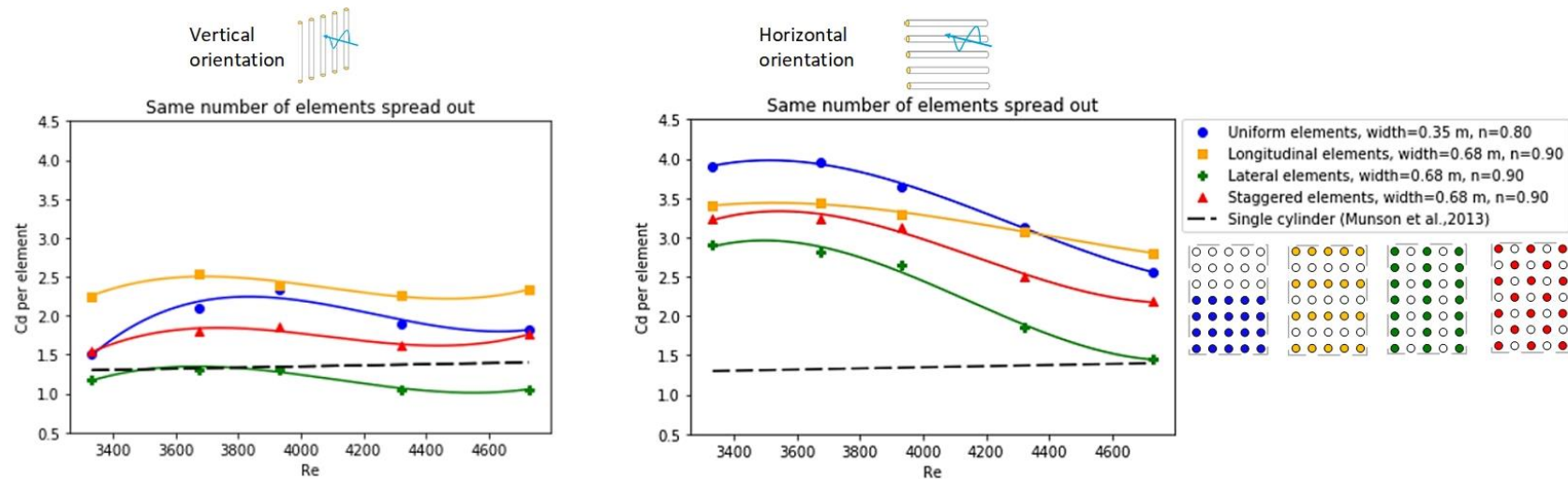


Figure 5.14 Drag coefficient against Re for three different ways of spreading out the elements. Vertical orientation (left) Horizontal orientation (right)

5.1.4 Effect of spreading out the same number of elements over a larger area

Spreading out the same number of elements over a larger area leads to an increase in porosity from $n=0.80$ to $n=0.90$ and therefore it is expected that the drag coefficient per element increases as well. However, it is not only the porosity that changes when the elements are spread out, but also the arrangement. In the reference case of $n=0.80$, the elements are uniform, which does not hold for the redistributed cases. This also influences the drag coefficient, as explained in the previous section.

The results are shown in Figure 5.14. Only in the case of the longitudinal elements, the drag coefficient is larger in comparison to the reference case. In case of the vertical elements, this holds for all Re . In case of the horizontal elements, the drag coefficient of the longitudinal elements is only larger when $Re > 4350$. As shown, the vertical velocity decreases for decreasing kd (increasing Re), while the horizontal velocity increases. The results suggest that the vertical velocities are reduced more in the reference case, whereas horizontal velocities are reduced more in the spread out case (longitudinal elements). For the staggered and lateral elements the drag decreases in comparison to the reference case, showing that in the presently tested range the arrangement effect has a larger influence on the drag than the porosity effect.

5.1.5 Width effect

When there are two cylinders, they may shelter each other (shown in Figure 5.15). Downstream cylinder B could therefore experience a lower velocity (depending on the distance between the two cylinders). As explained in Section 5.1.3, this is due to the reduction of the velocity in the wake area of cylinder A. The turbulence which is contributed by the wake also delays the point of separation on the downstream cylinder, resulting in a lower pressure difference along the cylinder. These two properties of the wake result in a lower drag coefficient of cylinder B in comparison to cylinder A. The drag coefficient averaged over both elements would therefore also be lower.

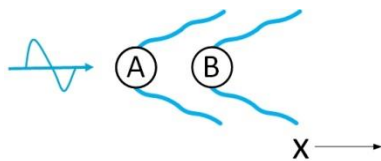


Figure 5.15 Cylinders A and B

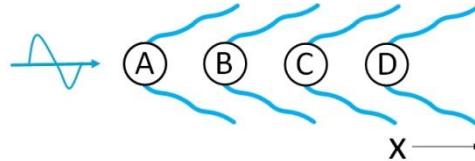


Figure 5.16 Cylinders A, B, C and D

Considering these results, it is expected that the drag coefficient of cylinder C (Figure 5.16) even has a lower value than cylinder B, as it is behind both cylinders A and B. The same holds for cylinders D-E-F-G and so on, meaning that the drag coefficient of each following element would decrease for increasing x . Based on this assumption, it is expected that the drag coefficients (averaged over the elements) of the half width structures have higher values than ones of the full width structures. The results are shown in Figure 5.17 (half width structures) and Figure 5.18 (full width structures). The results are according to the expectations. Only in case of the vertical elements with the lowest Re values (shortest waves), the drag coefficients of the half and full width structures are quite similar. A possible explanation is presented in the final part of this sub-section.

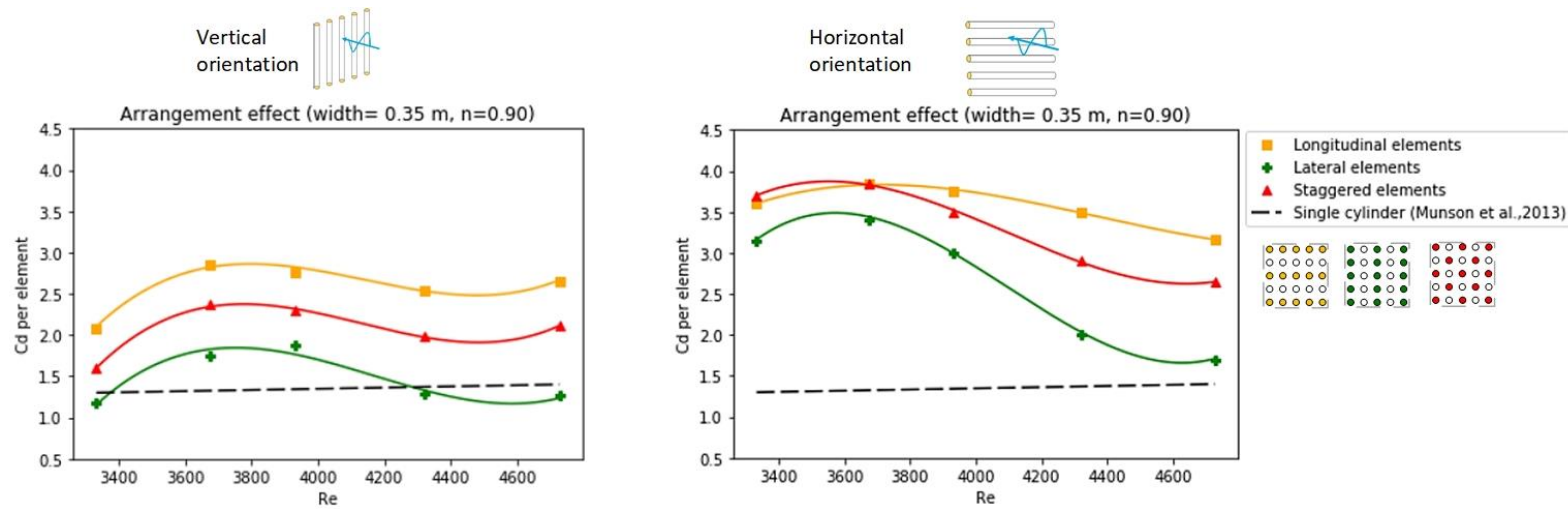


Figure 5.17 Drag coefficient against Re for three different ways of arrangement with width=0.35 m. Vertical orientation (left) Horizontal orientation (right)

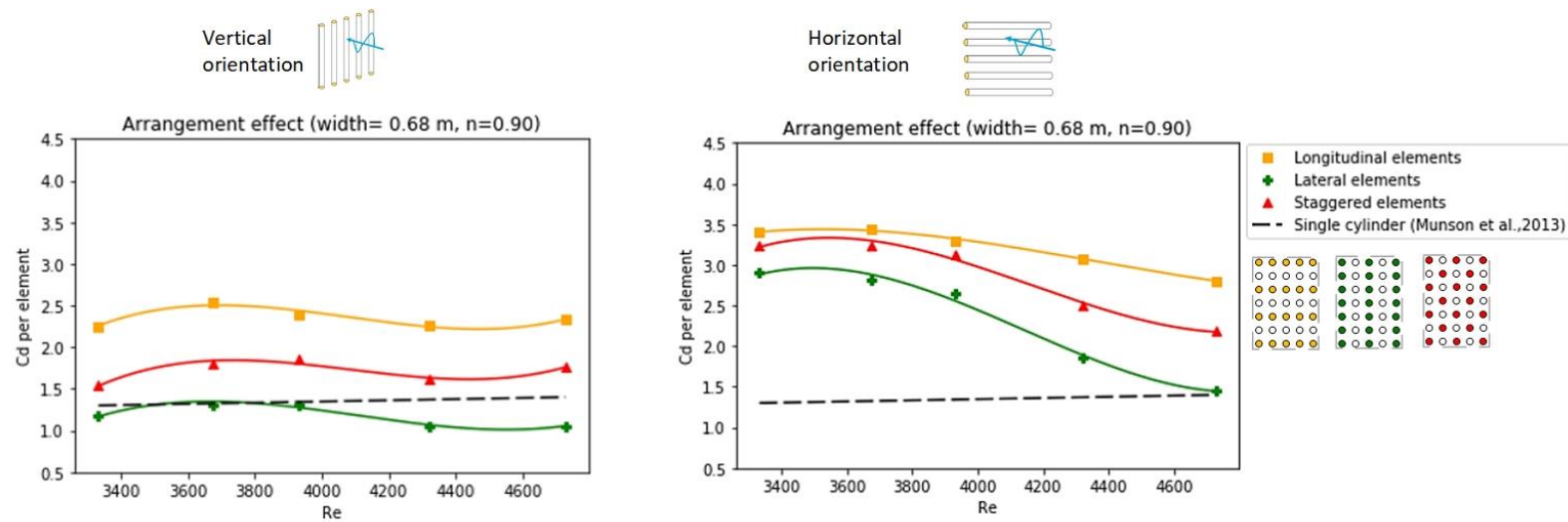


Figure 5.18 Drag coefficient against Re for three different ways of arrangement with width=0.68 m. Vertical orientation (left) Horizontal orientation (right)

The elements are shown in Figure 5.19. As shown in Equation 5.3, the wave energy dissipation is proportional to the drag coefficient multiplied by the velocity to the third power:

$$E_{d,horizontal} \sim C_d \cdot u^3 \quad [5.6]$$

Throughout the structure (increasing x), each element may experience a lower velocity in comparison to the velocity experienced by the element in front of it (upstream element). Therefore, the wave dissipation that is contributed by each element would decrease non-linearly for increasing x .

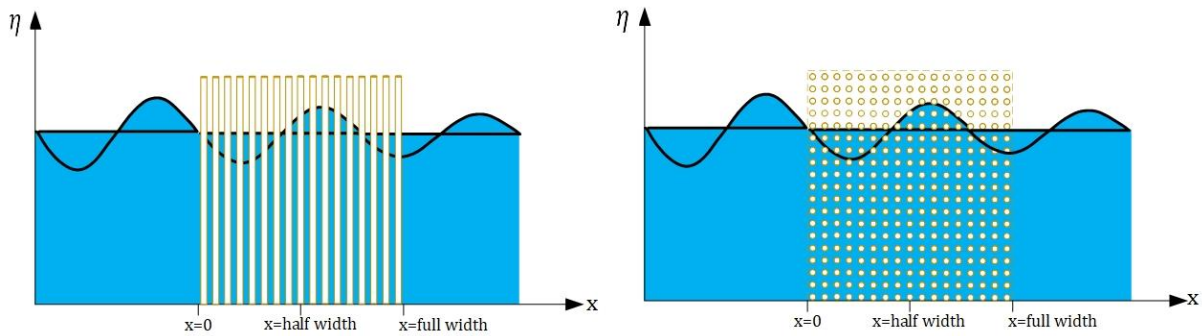


Figure 5.19 Wave transformation through structure. Vertical orientation (left) Horizontal orientation (right)

Based on this reasoning, it is expected that most of the dissipation would take place in the first half of the structure. As mentioned in Section 4.4.3 that is the case. For both horizontal and vertical elements around 70% of the total dissipation takes place in the first half of the structure. This holds for all three different arrangements (longitudinal, lateral and staggered elements) in all wave cases. The wave energy dissipation through the structures with the longitudinal elements is shown (again) in Figure 5.20.

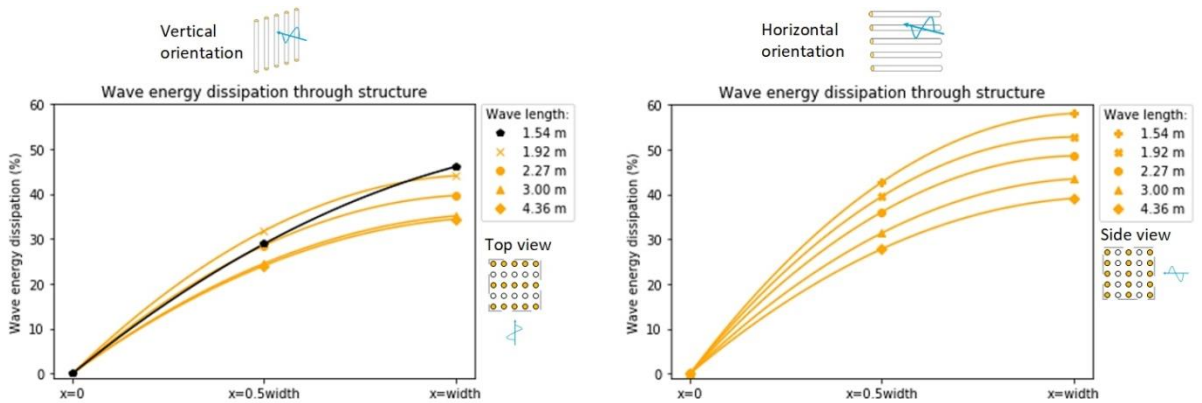


Figure 5.20 Wave energy dissipation through structure with longitudinal elements. Vertical orientation (left) Horizontal orientation (right)

What is striking is that only in case of the vertical elements with the shortest waves (marked black) around 50-55% of the total wave dissipation takes place in the first half of the structure. This also holds for the lateral and staggered elements (shown in Section 4.4.3). The results could be related to the drag coefficients that are found for the vertical elements with the lowest Re values (shortest waves). In this range the drag coefficients of the half and full width structures are quite similar. This could be explained by the length of the wakes. For smaller wave periods the length of the wakes are shorter, as

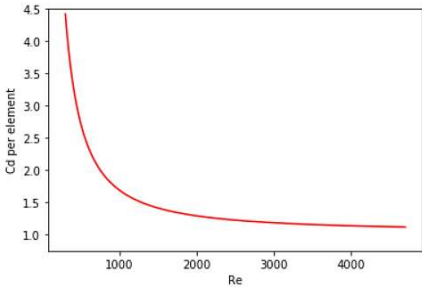
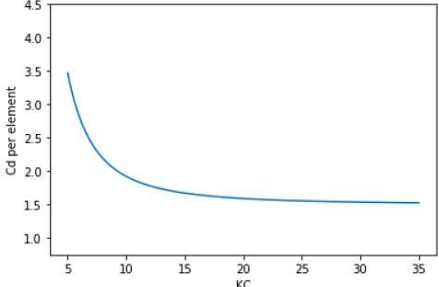
every half period the velocity decreases until it changes direction. Also, the amount of time available for the development of a wake is lower. As the wake length is shorter, the wakes might finish before reaching the next element. The drag coefficients of the downstream elements would therefore be unaffected.

However, these results are not seen in case of the horizontal elements. For the shortest waves, around 70% of the total wave dissipation takes place in the first half of the structure (rather than 50-55%). Also, the drag coefficients of the half width structures have higher values than the ones of the full width structures. This is possibly due to the presence of higher vertical velocities with the shortest waves (shown in Figure 5.4). The vertical velocities can be reduced more effectively by the horizontal elements, as they have more exposure to the vertical velocity component in comparison to the vertical elements. Based on the results, it could be possible that the vertical velocities are more reduced in the first half of the structure in comparison to the second half, which would explain the higher dissipation rate of 70%.

5.2 Comparison drag coefficients with previous studies

So far the relative values of the drag coefficients have been discussed to see the influence of the different configurations. In this section the results are compared to other research works to see how much they relate to each other under comparable conditions. In previous vegetation studies drag coefficients have been derived as well, as shown in Table 2.2 (Section 2.2.3). In these studies the vegetation has been schematized in various ways such as flexible plastic strips, flexible real vegetation and rigid wooden cylinders. The latter schematization has the most similarity to the application used in this research and is shown in Table 5.1

Table 5.1 Overview of vegetation studies on the drag coefficient. Vegetation schematized as rigid cylinders

Study	Hu et al. (2014)	Ozeren et al. (2014)
Schematization	Rigid wooden cylinders	Rigid wooden cylinders
Flow	Waves + current	Waves
Deriving method	Direct measurement method	Calibration method
C_d relation	$C_d = 1.04 + \left(\frac{730}{Re}\right)^{1.37}$ $R^2 = 0.66$ $300 < Re < 4700$ 	$C_d = 1.5 + \left(\frac{6.785}{KC}\right)^{2.22}$ $R^2 = 0.21$ $5 < KC < 35$ 

The KC range of 8-23 that is used in this research is applied on the two previous studies. Reason for using parameter KC (instead of Re) is that it describes the importance of the drag forces relative to the inertia forces. For small KC numbers inertia dominates, while for large numbers the drag forces are more important. Furthermore, the KC number gives insight on the magnitude of the stroke of motion of the waves, as this is calculated by (Suzuki and Arikawa, 2010):

$$2a = \frac{KC}{\pi} D \quad [5.7]$$

$2a$ = the stroke of motion of the waves (m)

D = diameter of the cylinder (m)

When the stroke of motion of the waves ($2a$) is smaller than the spacing between the elements (S), the bulk drag coefficient (drag coefficient per element) is equal to the value of a single element. When $2a > S$, the bulk drag coefficient starts decreasing (shown in Section 2.2.3).

Results are shown in Figure 5.21. Hu et. al. (2014) found lower and more constant values of the drag coefficients compared to Ozeren et. al. (2014). Furthermore, the values are lower than the ones of a single cylinder. Reason for the more realistic values of the drag coefficients is that they are derived from direct force and velocity measurements, while in the other study the calibration method is used.

The (calibrated) drag coefficients of the vertical elements obtained in this study are added to the plot (Figure 5.21). Note that the fitted line of Ozeren et. al. (2014) is shown, while in the original plot there is a lot of scatter around the fitted line (shown in Figure 5.22). The coefficients derived in this study usually fall on top of the ones in the original plot by Ozeren. Only in the case of the longitudinal elements the drag coefficients are higher than those found in the literature. However, this arrangement was not tested in their experiments.

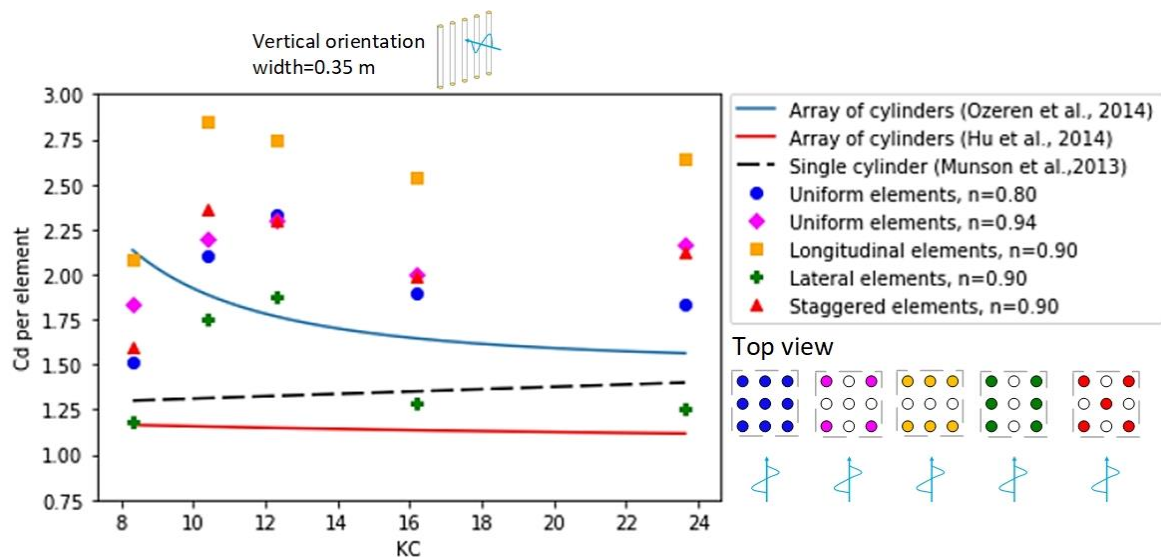


Figure 5.21 Drag coefficients plotted as a function KC for current and previous studies

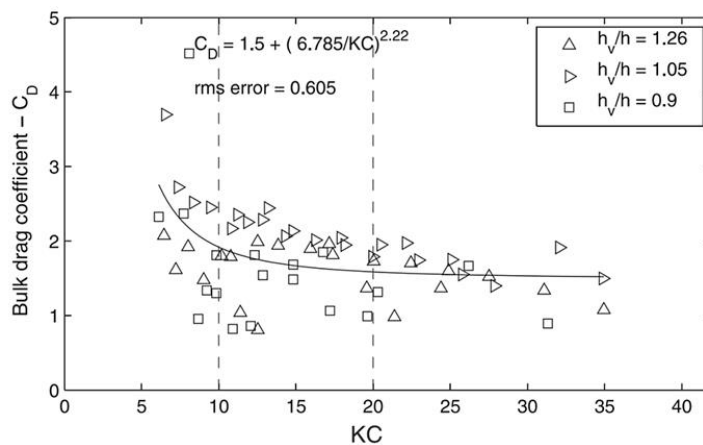


Figure 5.22 Original plot of Ozeren et. al. (2014)

For $KC < 15$ the calibrated drag coefficients start increasing. This is possibly due to the relative importance of the inertia force. For larger values of KC the drag coefficients are more constant. These values might be too large as well, which could be due to an underestimation of the horizontal velocity (u). With the calculated velocity (u) and the measured energy dissipation, the drag coefficients are computed:

$$E_d \sim C_d \cdot u^3 \quad [5.8]$$

The velocity that is used is the undisturbed velocity in front of the structure, assuming linear wave theory. However, the velocity inside the structure might be higher as the flow accelerates in between the gaps of the elements. An estimation of the higher velocity can be made by dividing the undisturbed velocity by the porosity of the elements (n). With the same (measured) energy dissipation the drag coefficient would go down with a factor $(1/n)^{-3}$. With porosities varying between 0.80-0.94, the drag coefficients would have a 51-83% decrease.

The drag coefficients obtained in this study are also compared with the study of Suzuki and Arikawa (2010). The drag coefficient per element is plotted as a function of $2a/S$ (shown in Figure 5.23). With this parameter not only the porosity, but also the wave case is represented. The drag coefficients obtained in this study are higher for all $2a/S$. For $2a/S > 1$, it is expected that the drag coefficient would start decreasing, but that trend is not shown. As mentioned, the high values of the drag coefficients could be due to inertia and permeability effects. Furthermore, the wave cases in this research are in the Stokes 2nd and 3rd order region, indicating that the waves cannot be fully described by linear wave theory. The non-linear effects among other possible effects are not included in the analytical model of Dalrymple (1984). Therefore, the drag coefficients do not only represent drag forces, but also other processes.

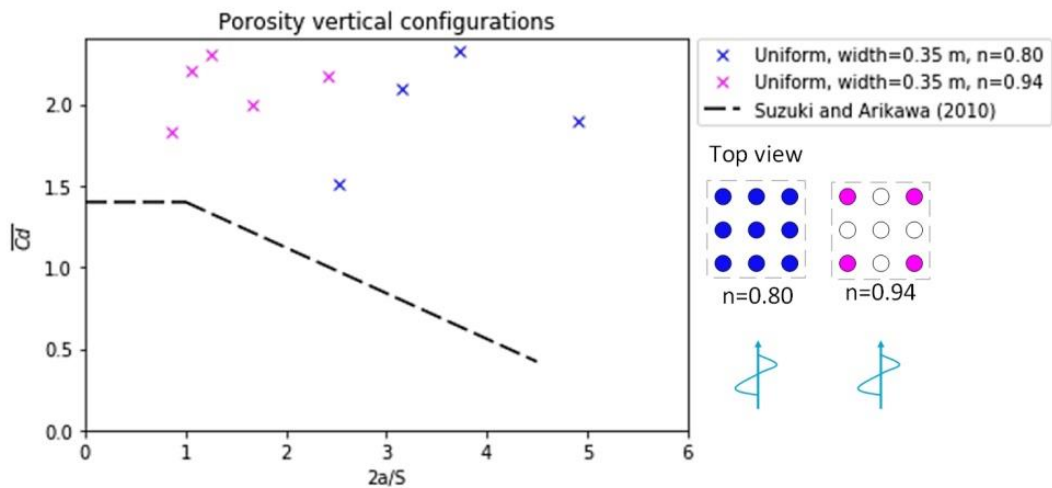


Figure 5.23 Bulk drag coefficient vs. $2a/S$

5.3 Relationship with prototype

The brushwood structures in Demak consist of vertical and horizontal elements. The vertical elements are either bamboo poles or PVC poles. The horizontal elements consist of brushwood. These elements can be seen as filling material of the structure (shown in Figure 5.24a). Based on the study of Lucas (2017) the porosity of the brushwood is estimated to be $n=0.25-0.40$. During the project several problems have been encountered with brushwood, as the material requires regular maintenance. This is partly due to the sinking of the material into the soft mud. Also, the brushwood material washes away often as it is lighter than water and difficult to constrain in vertical direction. Because of these problems, PVC poles without fill material have been applied as well in a later stage in the project (shown in Figure 5.24b).



Figure 5.24 (a) Structure with brushwood fill material (Gijón Mancheño, 2017) (b) Structure without brushwood fill material (Gijón Mancheño, 2017)

The results of the physical scale model have shown that for decreasing kd (moving towards shallow water) the dissipation rates of the horizontal and vertical elements become more similar to each other. For increasing kd (moving towards deep water) the highest dissipation rates are obtained by the horizontal elements. The results of the drag coefficient per element as a function of kd are shown in Figure 5.25. These include the three configurations that have the highest dissipation to reflection ratios.

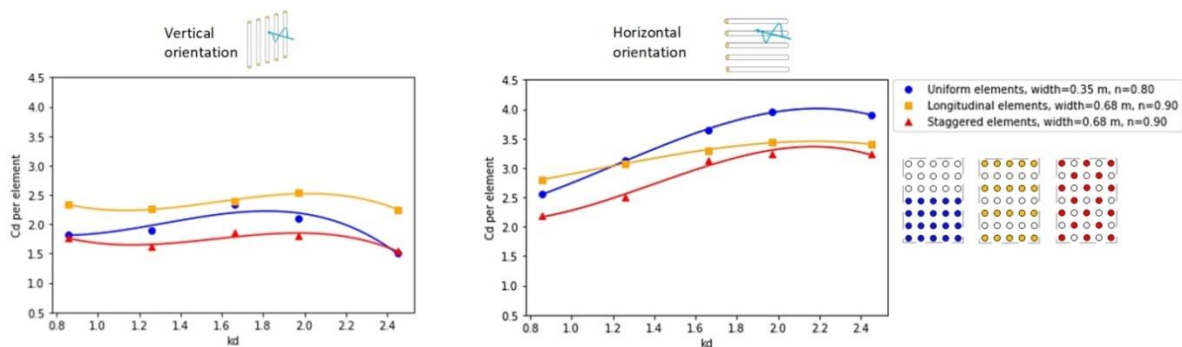
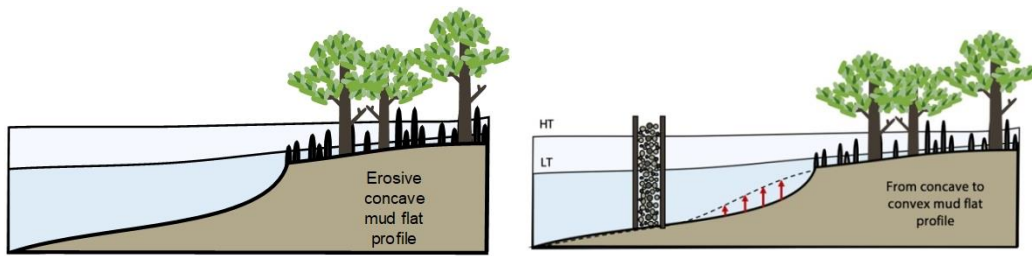
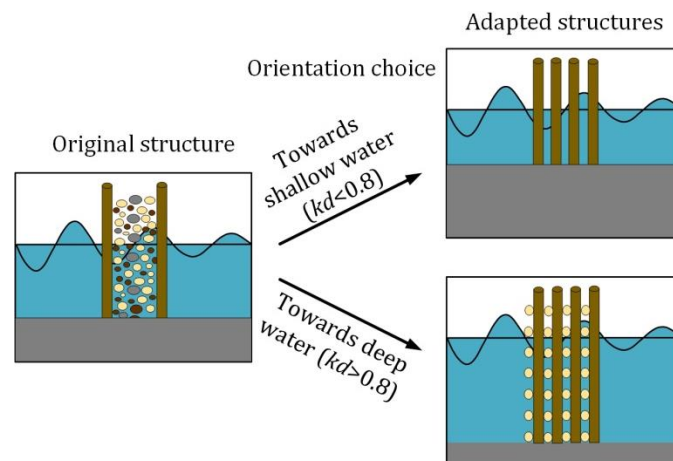


Figure 5.25 Drag coefficient as a function of kd for top three configurations. Vertical orientation (left) Horizontal orientation (right)

To relate the results obtained from the flume scale to the prototype, two representative wave conditions are chosen. These are based on the local wave conditions measured in front of the brushwood structure in the project area of Demak in both the summer and winter of 2017. Results of these measurements are shown in Appendix B. In summer the following wave height, wave period and water depth are used: $H_s = 0.05$ m, $T_p = 5.5$ s and $d = 0.70$ m. In winter more extreme conditions are present, namely: $H_s = 0.40$ m, $T_p = 8$ s and $d = 1.25$ m. By using the dispersion relation (Equation 2.2), the corresponding kd values are computed. For both seasons the kd value is equal to 0.30. Looking at the graphs in Figure 5.25, it is expected that for $kd = 0.30$ similar dissipation rates are obtained by the horizontal and vertical elements. For this reason and because of the intensive maintenance that is required when applying the brushwood material, it is recommended to only use vertical elements. Note that this is under the assumption that the drag coefficients of the laboratory experiments can be directly applied to the prototype.



However, among the 20 km coastline there might be locations that have higher kd values. This holds especially for the locations that have a highly erosive concave mud flat profile (shown in Figure 5.26). For those locations that tend to go more towards deep water conditions ($kd > 0.8$), it is recommended to use structures with horizontal elements. Based on the results, it is expected that higher dissipation rates are achieved with this orientation. As the brushwood structures in the field have lower porosities ($n = 0.25-0.40$) in comparison to structures in the flume ($n = 0.80-0.90$), it is expected that higher reflection rates are obtained. This is undesirable for structure stability and future mangrove colonization. For these reasons it is recommended to use horizontal bamboo beams that are more separated. Figure 5.27 shows an overview of the choice of orientation of elements based on parameter kd .



After the orientation of the structure is chosen, a few adaptations to the design can be made to increase the wave energy dissipation by the elements. One of these is spreading out the same number of elements over twice the area. Based on the results obtained in the flume, it is expected that higher dissipation rates are achieved when the vertical elements are spread out. In case of the horizontal elements it is not recommended to do this after $kd > 1.25$ (shown in Figure 5.25), as in the denser case higher dissipation rates are expected.

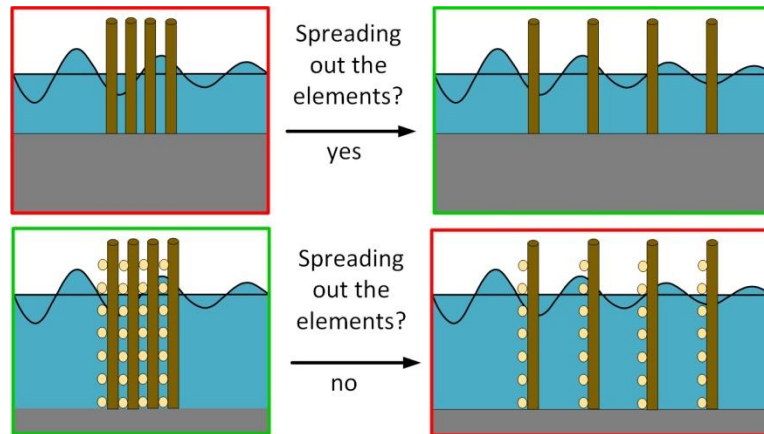


Figure 5.28 Spreading out the elements over twice the area. Configurations marked in green are expected to lead to higher dissipation rates in comparison to the configurations marked in red.

Another adaptation that can be made is increasing the width of the structure (as shown in Figure 5.29). However, due to the sheltering effect of elements it is expected that the additional dissipation is lower than the dissipation in the reference case (shown left). Therefore, it wouldn't be economical to increase the width of the structure. This should only be done at locations where additional wave dissipation is really necessary.

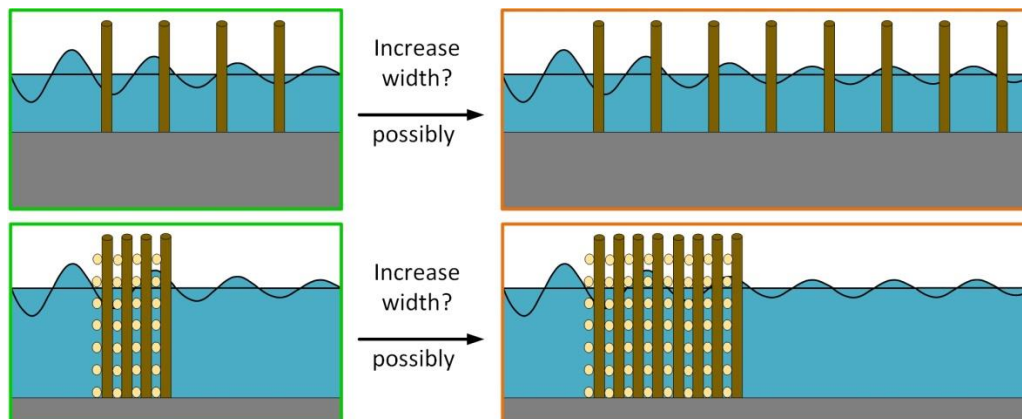


Figure 5.29 Increasing the width of the structure. Configurations marked in green are expected to have higher dissipation rates in comparison to the additional dissipation rates by the configurations marked in orange.

Note that no porosities are recommended. As only a limited number of porosities ($n=0.80-0.94$) are tested in this study, it could be possible that there are lower porosities that have higher dissipation to reflection ratios. Also the length scale effect is not checked, as the tests have been performed with one size of the diameter only. Furthermore, it could be possible that with the sparser structures more sediment is able to travel through the structures in offshore direction. This would happen if the transmitted waves are still high enough to stir up the sediment behind the structure.

6. Conclusions and recommendations

This chapter contains the final conclusions and recommendations of this study. Section 6.1 describes the conclusions and answers the research questions that were formulated in Section 1.3. Recommendations for further research are given in Section 6.2.

6.1 Conclusions

This study aims to optimise the design of permeable (brushwood) structures to capture sediment in order to encourage mangrove re-establishment on tropical mud coasts. Preferably wave transmission should be low in order to create a calmer climate behind the structure. In that way sediment is able to settle down, which could lead to a recovery of the mud profile. It is also preferred that reflection by the structure is low. High reflection rates cause scour holes that lead to instability of the structure. Furthermore, scour holes could hinder future mangrove re-establishment. Aiming to achieve low reflection and transmission rates, the dissipation inside the structure has to be as high as possible. The main research question was therefore formulated as follows:

In what manner do different design parameters of brushwood structures affect the wave energy balance (reflection, dissipation and transmission) for different wave cases?

The permeable (brushwood) structure was schematized as an array of cylinders. The following effects were tested in a wave flume under different wave cases:

- Orientation (horizontal vs. vertical elements)
- Porosity
- Arrangement of the elements
- Spreading out the same number of elements over a larger area
- Width of the structure

Generally the measured reflection rates (in terms of wave energy) are low and constant over the different wave cases (0.2-8.6%). Reason for this is that high porosities ($n=0.80$, $n=0.90$ and $n=0.94$) are used. Within the low rates there are small differences between configurations. The lowest porosity structures have the highest reflection rates. These results are in agreement with the expectations, as structures with lower porosities have a larger frontal area and therefore more reflection.

The wave energy dissipation rates of the different orientations were compared to each other. By using horizontal elements instead of vertical ones, up to twice as much wave dissipation is achieved. A reason for this difference is that the horizontal elements have

more exposure to the vertical component of the wave motion in comparison to the vertical elements. The vertical velocities can therefore be reduced more, which would explain the higher dissipation rates. When the vertical velocities become smaller, the horizontal and vertical elements start having similar dissipation rates.

Furthermore, the structure width was doubled to see to how much additional wave dissipation this would lead. The results show that in most cases around 70% of the total dissipation takes place in the first half of the structure. Therefore, the wave dissipation contributed by each element decreases through the structure. A reason for this is the sheltering effect of elements. Due to this effect, the downstream elements experience a lower velocity in comparison to the upstream elements. Their contribution to the total wave energy dissipation is therefore also lower.

Additionally, the effect of three different arrangements was tested. In one arrangement the elements are most exposed to the wave action ('longitudinal' elements), followed by arrangements that are more sheltered ('staggered' and 'lateral' elements). The sheltering effect of elements is also observed in the results of these tests, as the longitudinal elements have the highest dissipation rates, followed by the staggered and lateral elements.

For cost reasons it was interesting to see how much additional wave dissipation could be achieved by spreading out the same number of elements over twice the area. Results show that redistributing the vertical elements is beneficial for all the tested wave cases. For the horizontal elements it only becomes more beneficial to spread out the elements for the wave cases in which the vertical velocities are relatively low. This suggests that the horizontal velocities are reduced more in the spread out case (with higher porosity of $n=0.90$), whereas vertical velocities are reduced more in the reference case (with lower porosity of $n=0.80$).

With the obtained results, the following sub-question was answered:

How representative are existing analytical models for the wave dissipation through the structures?

Dalrymple (1984) derived an analytical model for wave dissipation through an array of vertical cylinders. The scale model used in the flume has more geometrical resemblance with this type of structure in comparison to other ones (e.g. granular structures). Therefore, the choice was made to link the results obtained in the flume to the analytical model of Dalrymple. In this model the wave energy dissipation is defined as the work done by the horizontal drag force (assuming linear wave theory). With the measured wave dissipation, drag coefficients were derived with the calibration method. The values of the drag coefficients of the different configurations were compared to each other. It became clear that the work done by the vertical drag force is not negligible. This holds especially for the horizontal elements that experience higher vertical velocities. Furthermore, the results are compared to other research works to see how much they relate to each other under comparable conditions. In the study of Ozeren et. al. (2014) drag coefficients were also derived through the calibration method and showed similar results. For $KC < 15$ the calibrated drag coefficients start increasing. This is possibly due to the relative importance of the inertia force.

Hu et. al. (2014) derived drag coefficients with direct force and velocity measurements and therefore the coefficients would be more representative of drag forces. Comparing the drag coefficients obtained in this study to the ones derived through the direct measurement method showed relative high values. This could be due to an underestimation of the horizontal velocity (u). The velocity that is used is the undisturbed velocity in front of the structure. However, the velocity inside the structure might be higher as the flow accelerates in between the gaps of the elements. Furthermore, the wave cases in this research are in the Stokes 2nd and 3rd order region, indicating that the waves cannot be fully described by linear wave theory. The inertia, permeability and non-linear effects among other possible effects are not included in the analytical model of Dalrymple. Therefore, the drag coefficients do not only represent drag forces, but also other processes.

The final sub-question was formulated as follows:

What recommendations can be made for the practical design of brushwood structures?

As the brushwood material requires regular maintenance, it became interesting to see whether a similar amount of wave dissipation could be achieved by using vertical elements only (without fill material). The results of the wave flume experiments have shown that up to twice as much wave dissipation is achieved by the horizontal elements in comparison to the vertical elements. This only holds in the wave cases in which the vertical velocities are relatively high. However, when the vertical velocities become smaller, the horizontal and vertical elements have similar dissipation rates. By representing the wave case with parameter kd , which is an indication for the different water regions (deep, intermediate or shallow water), a choice can be made for the orientation of the structure in the field. Under the assumption that the drag coefficients of the laboratory experiments can be directly applied to the prototype, it is recommended that for $kd < 0.8$ (moving towards shallow water with lower vertical velocities) vertical elements are used. When $kd > 0.8$ (moving towards deep water with higher vertical velocities), it is recommended that horizontal elements are used.

Based on wave measurements in front of the brushwood structures in Demak (2017), the kd value is estimated to be 0.30. For those specific locations it is recommended to use vertical elements. However, locations that are extremely erosive are expected to have higher kd values. For those locations it is recommended to use structures with horizontal elements. In the original brushwood structure the porosity is lower ($n=0.25-0.40$) in comparison to the structure in the flume ($n=0.80-0.94$) and therefore higher reflection rates are expected in the field. To avoid this, it is recommended to use horizontal bamboo beams that are more separated (instead of brushwood).

After the orientation of elements is chosen a few adaptations can be made to the structure that could increase the dissipation rates. One of these is spreading out the same number of elements over twice the area. Based on the results obtained in the flume, it is expected that higher dissipation rates are achieved when the vertical elements are spread out. In case of the horizontal elements it is not recommended to do this after $kd > 1.25$, as in the denser case higher dissipation rates are expected.

Another adaptation that can be made is increasing the width of the structure. However, due to the sheltering effect of elements, it is expected that the additional dissipation is lower than the dissipation in the reference case. Therefore, it wouldn't be economical to increase the width of the structure. This should only be done at locations where additional wave dissipation is really necessary.

Note that no porosities are recommended. As only a limited number of porosities ($n=0.80-0.94$) are tested in this study, it could be possible that there are lower porosities that have higher dissipation to reflection ratios. Also, the length scale effect is not checked, as the tests have been performed with one size of the diameter only. Furthermore, it could be possible that with the sparser structures more sediment is able to travel through the structures in offshore direction. This would happen if the transmitted waves are still high enough to stir up the sediment behind the structures.

6.2 Recommendations

To gain more insight on the physical mechanisms that affect the wave energy dissipation, the following recommendations are made for further research.

To distinguish drag and inertia effects, force and velocity measurements can be performed for the optimum configurations. By measuring the force and velocity on (single) elements throughout the structure, sheltering effects are taken into account as well. The measurements can be done by using a force transducer and ADV (Acoustic Doppler velocimetry). These should be placed next to each other, ensuring that the measurements are in phase and Morison's method can be applied (Appendix A). With this method, drag and inertia coefficients can be found. By using this direct measurement method, it is expected that more realistic values are obtained for the coefficients in comparison to the calibration method used in this study. Furthermore, the high drag coefficients found in this study could be due to an underestimation of flow velocities, as the undisturbed velocity in front of the structure is used (in between the gaps of the elements they might be higher). Also the waves are described by linear wave theory, when in fact they are non-linear. With the actual velocities measured inside the structure, these effects are taken into account.

Moreover, in the case of the horizontal structures, drag coefficients are relatively high (3-4) for higher vertical velocities. The energy dissipation also consists of a vertical part, which is the work done by the vertical drag force. In the analytical model by Dalrymple (1984), only the horizontal part is considered. With the proposed measurements a distinction can be made between the horizontal and vertical part of the energy dissipation, as the force transducer and ADV are able to measure in both directions. Therefore, it is expected that that also for the horizontal configurations more realistic values of the drag coefficients are obtained.

The reflection rates obtained in this study are relatively low and more or less constant over the different wave cases, as high porosity structures are tested. By using larger elements, not only length scale effects could be tested, but also lower porosities. As the porosity of the structure is lower, it is expected that higher and more varying reflection

rates are obtained. In this way, the interaction between reflection and structural parameters over the different wave cases can be analysed better. In this analysis the relationships for the reflection coefficients could be fitted with various parameters such as the porosity, frontal area (arrangement) and structure width to see which correlate best.

The tests are performed with regular aluminum elements ('perfect cylinders'), whereas in practice the elements have irregularities along the diameter and length. To see the effect of the irregularity, it is recommended to do additional tests with bamboo elements.

Finally, the obtained transmission rates can be used for new research applications such as morphological studies. In these studies, it can be checked whether the obtained transmission rates lead to a significant decrease in the amount of sediment that is stirred up. It is expected that this is the case, as the bed shear stress depends on the velocity squared ($\tau \sim u^2$) and thus on the wave height. When the wave height is reduced with a factor x , the bed shear stress is reduced with a factor x^2 . This may mean that waves do not have to be dissipated completely. If the required wave climate behind the structure is achieved, it does not necessarily have to be a problem that structures with high porosities are used, as less sediment would be able to stir up and transport in offshore direction through the structure. Furthermore, it can be studied whether the transmitted waves are low enough for the sediment (brought in by the tide) to settle down behind the structure.

Bibliography

Anderson, M. E. and Smith, J. M. (2014). Wave attenuation by flexible, idealized salt marsh vegetation. Coastal Engineering, Volume 83.

Bokaian, A. and Geoola, F. (1984). Wake-induced galloping of two interfering circular cylinders, J. Fluid Mechanics.

Bosboom, J. and Stive, M. (2015). Coastal Dynamics I: lecture notes CIE4305. Delft Academic Press.

Bradley, K. and Houser, C. (2009). Relative velocity of seagrass blades: Implications for wave attenuation in low-energy environments. Journal of Geophysical Research 114:1–13.

D'Angremond, K., Meer, J.W. v. d. and Jong, R. J. d. (1996). Wave transmission at low-crested structures, 25th International Conference on Coastal Engineering, Kobe, Japan.

Darcy, H. P. G., (1856). Les fontaines publiques de la ville de Dijon, Paris.

Dalrymple, R. A., Kirby, J. T. and P. A. Hwang (1984). Wave refraction due to areas of energy dissipation, J. Waterways, Port., Coastal, Ocean Eng., 110(1), 67-79.

Forchheimer, P. (1901). Wasserbewegung durch boden. Zeitschrift des Vereines Deutscher Ingenieur, 45th edition.

Goda, Y. and Suzuki, Y (1976). Estimation of incident and reflected waves in random wave experiments. In Proceedings of the International Conference on Coastal Engineering, Honolulu, Hawaii.

Holthuijsen, L. (2007). Waves in oceanic and coastal waters. Cambridge University Press.

Hu Z., Suzuki T., Zitman T., Uijttewaalt W. and Stive M. (2014) Laboratory study on wave dissipation by vegetation in combined current-wave flow, Coastal Engineering, Volume 88.

Infantes, E., Luhar, M. and Nepf, H., (2011). Seagrass blade motion under waves and its impact on wave decay. Marine Ecology Progress Series.

Ippen, A. (1966). Estuary and coastline hydrodynamics. McGraw-Hill.

Jadhav, R. S., Chen, Q. and Smith, J. M. (2013). Spectral distribution of wave energy dissipation by salt marsh vegetation. Coastal Engineering, Elsevier B.V.

Klaasman, B. (2005) Manual Matlab scripts Laboratory of Fluid Mechanics. Delft University of Technology.

- Kobayashi N., Raichle A.W. and Asano, T. (1993). Wave attenuation by vegetation. *J. Waterw. Port Coast. Ocean Eng.* 119, 30-48.
- Le Mehauté, B (1976). *An introduction to Hydrodynamics and Water Waves*. Springer.
- Losada, J. I., Maza, M. and Lara, J. L. (2016). A new formulation for vegetation-induced damping under combined waves and currents. In *Coastal Engineering 107*. Elsevier.
- Lucas, P. (2017). *Measuring and Modelling Wave Damping by Permeable Groins*.
- Mai, S., Lieberman, N. V. and Zimmermann, C. (1999). Interaction of foreland structures with waves, in W. Franzius-Institute for Hydraulic and G. Coastal Engineering, University of Hannover (eds), XXVIII-IAHR Conference, Graz.
- Mendez F.M. and Losada I.J. (2004.) An empirical model to estimate the propagation of random breaking and nonbreaking waves over vegetation fields. *Coastal Engineering* 51, 103-118. Mittal
- Mendez, F.J., Losada, I.J. and Losada, M.A. (1999). Hydrodynamics induced by wind waves in a vegetation field. *J. Geophys. Res.* 104, 18383–18396.
- Morison, J. R., O'Brien, M. P., Johnson, J. W. and Schaaf, S. A. (1950). The force exerted by surface waves on piles, *Petroleum Transactions, American Institute of Mining Engineers*.
- Nepf, H. M. (1999). Drag, turbulence, and diffusion in flow through emergent vegetation. *Water Resources Research*.
- Nepf, H. M., Sullivan, J. A. and Zavitoski, R. A. (1997). A model for diffusion within an emergent plant canopy, *Limnology and Oceanography*.
- Ozeren, Y., Wren, D.G. and Wu, W. (2014). Experimental investigation of wave attenuation through model and live vegetation. *J. Waterw. Port Coast. Ocean Eng.* 04014019.
- Thornton, E. B. and Calhoun, R. J. (1972). Spectral resolution of breakwater reflected waves, *Journal of Waterway, Harbour and Coastal Engineering Division*.
- Sayah, S. (2006). Efficiency of brushwood fences in shore protection against wind-wave induced erosion. *University of Libanaise*.
- Solitt, C.K. and Cross, R.H. (1972). Wave transmission through permeable breakwaters, 13th Conf. Coastal Engineering Vancouver.
- Suzuki, T. and Arikawa, T. (2010). Numerical analysis of bulk drag coefficient in dense vegetation by immersed boundary method. In *Coastal engineering* (S. 10).
- Ting, C., Lin, M. and Cheng, C. (2004). Porosity effects on non-breaking surface waves over permeable submerged breakwaters, Elsevier B.V.

Van der Meer, J.W. and Pilarczyk, K.W. (1990). Stability of low-crested and reef breakwaters. Proc. 22th. ICCE, Delft.

Williamson, C. H. K. (1992). The natural and forced formation of spot-like 'vortex dislocations' in the transition of a wake, J. Fluid Mechanics.

Winterwerp, J. (2014). Rehabilitation of mangrove-mud coasts an eroding part of Suriname coast.

Appendix A: Morison's equation and method

In an oscillatory flow with flow velocity u , Morison (1950) found an equation that gives the inline force parallel to the flow direction:

$$F = \rho C_m V \dot{u} + \frac{1}{2} \rho C_d A u |u| = F_I + F_D \quad [A.1]$$

F = the force on an object [N]

\dot{u} = the flow acceleration [m/s²]

F_I = the inertia force [N]

F_D = the drag force [N]

C_m = the inertia coefficient [-]

C_d = the drag coefficient [-]

A = the cross-sectional area perpendicular to the flow [m²]

V = the volume of the body [m³]

For a circular cylinder with diameter D , the cross-sectional area per unit cylinder length is $A=D$ and the volume of the cylinder is $V = \frac{1}{4} \pi D^2$ per unit cylinder length. Therefore, Equation A1 results in:

$$F = C_m \rho \frac{\pi}{4} D^2 \dot{u} + C_d \frac{1}{2} \rho D u |u| = F_I + F_D \quad [A.2]$$

Due to vortex shedding, there are also oscillatory lift forces. These forces are perpendicular to the flow direction and are therefore not included in the Morison equation. The drag force and inertia force are defined by empirical coefficients. The drag and inertia coefficient are determined experimentally. The coefficients can be fitted following the Morison method (1950), which is further explained.

From time series of the velocity u (m/s) and horizontal force F (N) one can determine the appropriate values for C_D and C_M by using Morison's Method (Morison et al., 1950). The approach is depended upon the realization that when:

u is maximum, \dot{u} is zero so that at that instant, t_1 , $F(t_1) = F_D$ and

\dot{u} is maximum, u is zero so that at that instant, t_2 , $F(t_2) = F_I$.

When the force is in phase with the velocity, the drag force is dominating over the inertia force. On the contrary, when the force is in phase with the acceleration, it implies that the inertia force is dominating over the inertia force.

Figure C1 shown an example plot of the time series of the velocity u (m/s), the acceleration \dot{u} (m/s²) and the horizontal force F (N). Under the above specified conditions, the Morison equation can be rearranged in such a way that both the inertia and drag coefficients can be determined:

$$C_M = \frac{4F}{\omega \rho D^2 \omega \hat{u}} \text{ at } t_1 \text{ when } u \text{ is zero} \quad [A.3a]$$

$$C_D = \frac{2F}{\rho D \hat{u} |\hat{u}|} \text{ at } t_2 \text{ when } \dot{u} \text{ is zero} \quad [A.3b]$$

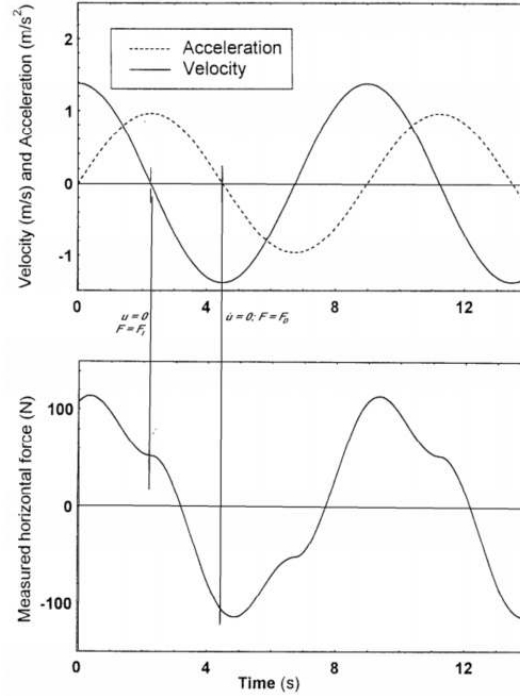


Figure C1 Measured Force and Velocity Record (Wave Forces on Slender Structures, n.d.)

The limitation of the method is that it can lack accuracy for the following reasons:

- A small error in the velocity time series can cause a significant phase error.
- The curve of $F(t)$ can be steep when determining C_D , which can cause an error in determining this coefficient. The effect on C_M is not as large.
- Information gathered from two instants (t_1 and t_2) is used to determine the coefficient. The rest of the data is not being used. Morison reduced this error by averaging the coefficients over a large number of measurements.

Appendix B: Wave measurements in Demak



Figure B1 Location of the wave loggers in Demak, Indonesia (source: Google Earth)

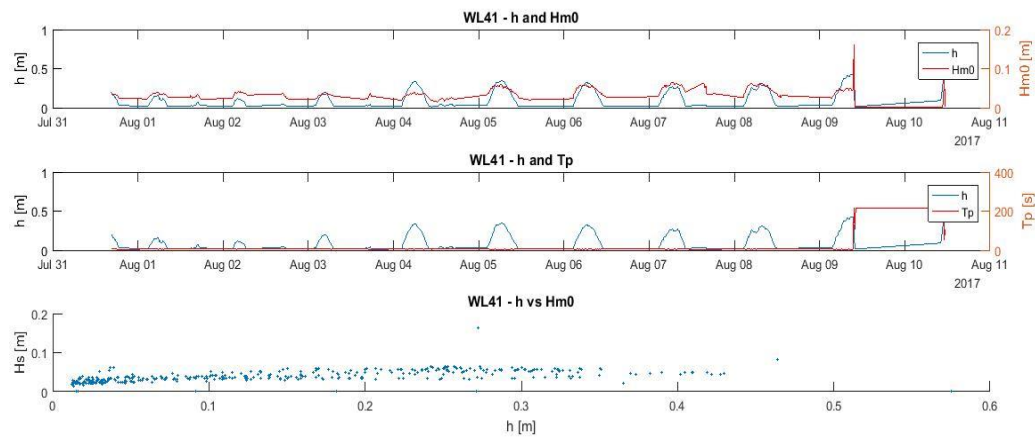


Figure B2 Wave data from summer period at location WL41

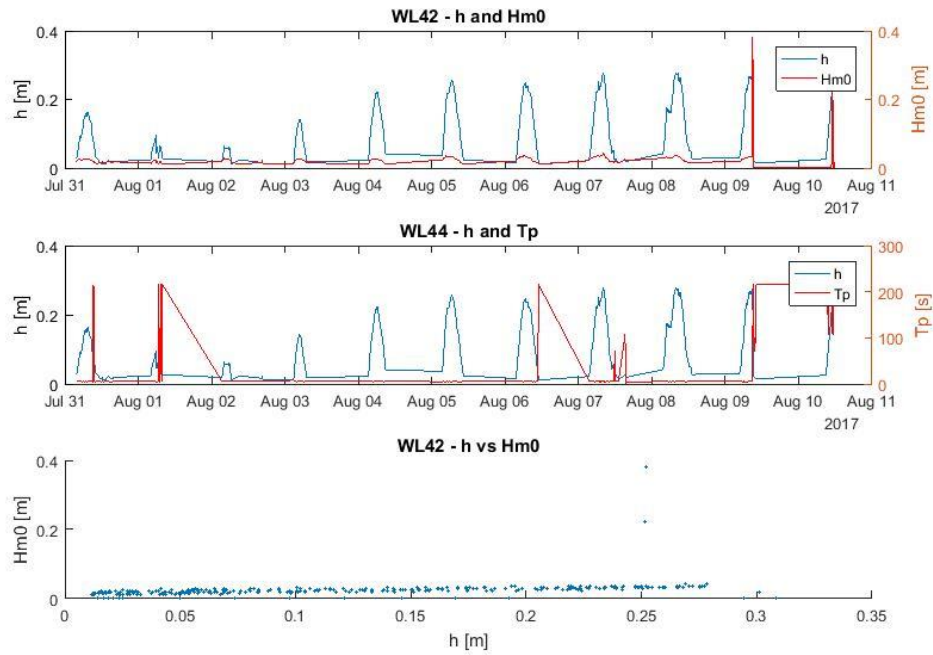


Figure B3 Wave data from summer period at location WL42

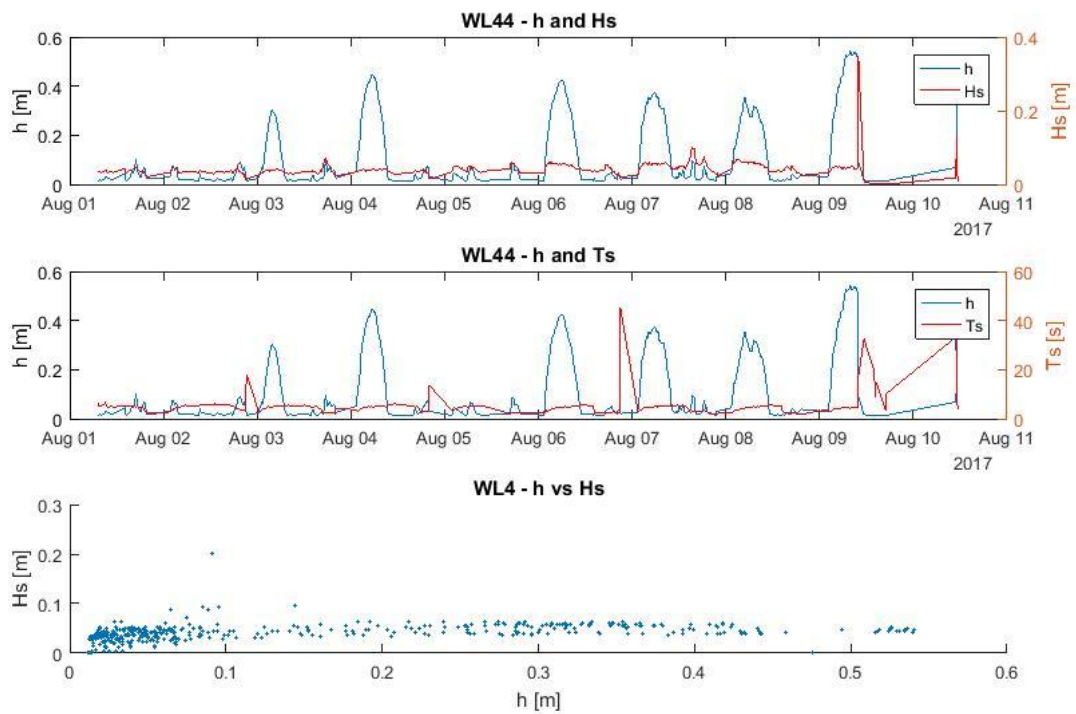


Figure B4 Wave data from summer period at location WL44

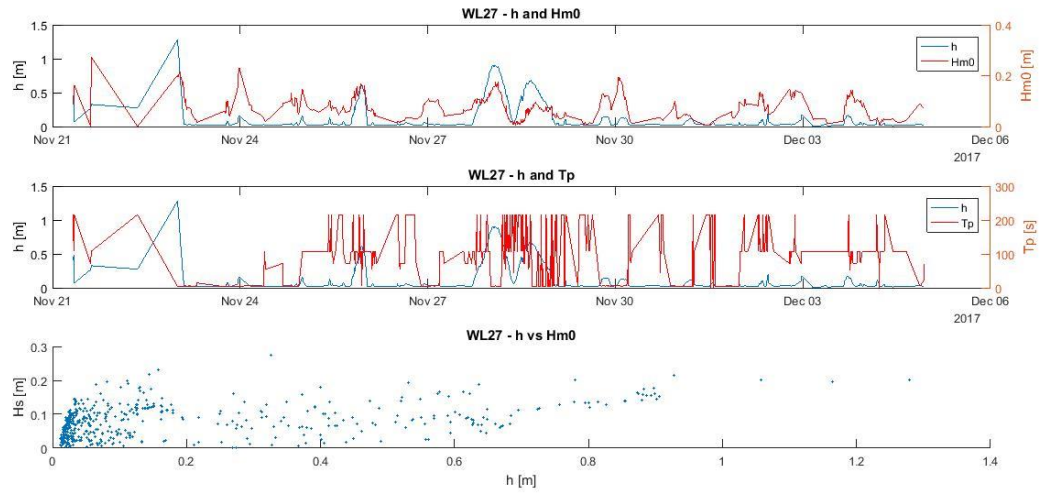


Figure B5 Wave data from winter period at location WL27

Appendix C: Method of Goda and Suzuki

To be able to calculate the wave height of the reflected wave, the method described by Goda and Suzuki (1976) can be used. This method has been written in a Matlab program Refreg by Klaasman (2005) and is used in the Environmental Fluid Mechanics Laboratory of TU Delft. In the case of regular waves two wave gauges are needed. They are placed at positions $x=x_1$ and $x=x_2$. The equations for the surface elevation η for both positions are given by:

$$\eta(x_1, t) = \sum_{n=1}^N a_{i,n} \cos(k_n x_1 - \omega_n t + \phi_{i,n}) + \sum_{n=1}^N a_{r,n} \cos(k_n x_1 + \omega_n t + \phi_{r,n}) \quad [B.1]$$

$$\eta(x_2, t) = \sum_{n=1}^N a_{i,n} \cos(k_n x_2 - \omega_n t + \phi_{i,n}) + \sum_{n=1}^N a_{r,n} \cos(k_n x_2 + \omega_n t + \phi_{r,n}) \quad [B.2]$$

In which:

η is the water-surface elevation relative to the mean water level

t is the time

$a_{i,n}, a_{r,n}$ the amplitude of the n -th harmonic of the incoming and reflected wave

k_n is the wave number of the n -th harmonic

ω_n is the angular wave frequency of the n -th harmonic

$\phi_{i,n}, \phi_{r,n}$ the phase of the n -th harmonic of the incoming and reflected wave

Only the first harmonic is used in the Refreg program. Therefore, Equation B1 and B2 become:

$$\eta(x_1, t) = a_i \cos(kx_1 - \omega t + \phi_i) + a_r \cos(kx_1 + \omega t + \phi_r) \quad [B.3]$$

$$\eta(x_2, t) = a_i \cos(kx_2 - \omega t + \phi_i) + a_r \cos(kx_2 + \omega t + \phi_r) \quad [B.4]$$

Equation B.3 can be rewritten in the following way:

$$\begin{aligned} \eta(x_1, t) = & a_i \{ \cos(kx_1 + \phi_i) \cos(\omega t) + \sin(kx_1 + \phi_i) \sin(\omega t) \} \\ & + a_r \{ \cos(kx_1 + \phi_r) \cos(\omega t) - \sin(kx_1 + \phi_r) \sin(\omega t) \} \end{aligned}$$

or

$$\eta(x_1, t) = A_1 \cos(\omega t) + B_1 \sin(\omega t) \quad [B.5]$$

The same holds for Equation B.4:

$$\eta(x_2, t) = A_2 \cos(\omega t) + B_2 \sin(\omega t) \quad [B.6]$$

In which

$$A_1 = a_i \cos(kx_1 + \phi_i) + a_r \cos(kx_1 + \phi_r) \quad [B.7]$$

$$B_1 = a_i \sin(kx_1 + \phi_i) - a_r \sin(kx_1 + \phi_r) \quad [B.8]$$

$$A_2 = a_i \cos(kx_2 + \phi_i) + a_r \cos(kx_2 + \phi_r) \quad [\text{B.9}]$$

$$B_1 = a_i \sin(kx_2 + \phi_i) - a_r \sin(kx_2 + \phi_r) \quad [\text{B.10}]$$

Equations B.7-B.10 can be rewritten into complex equations:

$$A_1 + iB_1 = a_i e^{ikx_1} e^{i\phi_i} + a_r e^{-ikx_1} e^{-i\phi_r} \quad [\text{B.11}]$$

$$A_2 + iB_2 = a_i e^{ikx_2} e^{i\phi_i} + a_r e^{-ikx_2} e^{-i\phi_r} \quad [\text{B.12}]$$

in which $i^2 = -1$.

Equations B.11 and B12 can be rewritten in the form of matrices:

$$\begin{pmatrix} e^{ikx_1} & e^{-ikx_1} \\ e^{ikx_2} & e^{-ikx_2} \end{pmatrix} \begin{pmatrix} a_i e^{i\phi_i} \\ a_r e^{-i\phi_r} \end{pmatrix} = \begin{pmatrix} A_1 + iB_1 \\ A_2 + iB_2 \end{pmatrix} \quad [\text{B.13}]$$

From a harmonic analysis of the water-surface elevation the A and B on the right hand side of Equation B.13 can be found by using a Fast Fourier Transform. At the beginning and end of the data-series two zero crossing with the same sign are used to determine the length of the series that will be analysed. If the wave period does not fit on the time step, there is a cut off error. The Fast Fourier Transform is used on two data series that is gathered by the two wave gauges. The number of point that is used fit to the time between two zero-crossings. The base period is the period with the maximum modulus of the FFT-coefficient.

Appendix D: Reference sheet wave gauge

- 2 -

1. Application.

The Wave-Height meter has been designed for dynamic fluid level measurements, e.g. wave-height measurements in hydraulic models.

2. Principle.

The instrument is composed of two parts:
- a gauge with integral pre-amplifier, and
- a separate main-amplifier (Figure 1).

The gauge consists of two parallel stainless steel rods, mounted underneath a small box, containing the pre-amplifier and the dc-dc converter.

The rods act as the electrodes of an electric resistance meter.

To eliminate the effect of the conductivity variations of the fluid, a platinum electrode is part of the system.

The main-amplifier contains a power-supply, a variable gain amplifier, a zero-shift and a panel-meter, indicating the instantaneous wave-height.

An analog output is available.

3. Features.

Wide range

Ranges of 5, 10, 20 and 50 cm can be selected at the main-amplifier.

Linearity.

Better than $\pm 0.5\%$ of the range selected.

Dynamic response.

The frequency characteristics of the system permit measurements from 0 up to 10 Hz..

Input/Output isolation.

The gauge circuit is powered by an isolating dc-dc coupled power-supply, minimizing electric interference problems when grounding the floating output.

- 3 -

4. Specifications.**a. Probe.**

Level-electrodes : rods, stainless steel, type 316,
 4 mm. diam., electrode spacing 23 mm,
 electrode length 59 cm.
 Ref. electrode : platinum, 5 x 2 mm diam..
 Non-linearity : 0.5% of selected range, b.s.l..
 Liquid medium : all liquids compatible with above-
 mentioned materials.
 Conductivity-
 influence : - minimum required conductivity 0.08 mS
 - sensitivity change <1% for variations
 between 0.1 and 2 mS.
 Dimensions : incl. electronics 70 x 8 x 9 cm.
 Weight : 0.7 kg.
 in container (12 x 73 x 14 cm), 3 kg.
 Output : 0.05 VDC/cm level-variation.
 Power : +/- 15 VDC, +/- 100 mA.

b. Control-unit.

Input : 0.05 VDC/cm.
 (+/- 15 VDC for probe electronics is
 supplied via input-connector.).
 Ranges : 5, 10, 20 and 50 cm.
 Output-shift : between + and - 10 VDC, within the
 limits of the standard output-voltage.
 Freq. response : 0 to 10 Hz.
 Output : +/- 10 VDC, 2 mA max. for the range
 selected.
 Power : 220 VAC, 50-60 Hz., 20 VA, incl. probe.
 Dimensions : portable case, 26 x 15 x 32 cm,
 (for 2 plug-in units Euro-frame)
 Weight : portable case 5 kg
 nett shipping weight per set 10 kg.

Figure C1 Specification wave gauges (Mellink, 2012)

Appendix E: Tables of Results

Test	Porosity	Width (m)	Arrangement	Orientation	Wave condition	H_I (m)	H_{R1} (m)	H_T (m)	H_{R2} (m)
1	0.80	0.35	Uniform	Vertical	H13T1	0.1116	0.0322	0.0900	0.0014
2	0.80	0.35	Uniform	Vertical	H13T1	0.1114	0.0328	0.0896	0.0014
3	0.80	0.35	Uniform	Vertical	H13T1.13	0.1204	0.0284	0.0940	0.0038
4	0.80	0.35	Uniform	Vertical	H13T1.13	0.1202	0.0288	0.0940	0.0038
5	0.80	0.35	Uniform	Vertical	H13T1.25	0.1228	0.0292	0.0958	0.0042
6	0.80	0.35	Uniform	Vertical	H13T1.25	0.1228	0.0290	0.0962	0.0044
7	0.80	0.35	Uniform	Vertical	H13T1.5	0.1204	0.0252	0.0998	0.0008
8	0.80	0.35	Uniform	Vertical	H13T1.5	0.1206	0.0256	0.1004	0.0004
9	0.80	0.35	Uniform	Vertical	H13T2	0.1212	0.0226	0.1024	0.0060
10	0.80	0.35	Uniform	Vertical	H13T2	0.1208	0.0240	0.1020	0.0044
Test	Porosity	Width (m)	Arrangement	Orientation	Wave condition	C_{R1}^2	C_T^2	C_{diss}^2	C_{R2}^2
1	0.80	0.35	Uniform	Vertical	H13T1	8.4%	65.0%	26.6%	0.0%
2	0.80	0.35	Uniform	Vertical	H13T1	8.6%	64.7%	26.7%	0.0%
3	0.80	0.35	Uniform	Vertical	H13T1.13	5.6%	61.0%	33.4%	0.1%
4	0.80	0.35	Uniform	Vertical	H13T1.13	5.7%	61.2%	33.1%	0.1%
5	0.80	0.35	Uniform	Vertical	H13T1.25	5.6%	60.9%	33.5%	0.1%
6	0.80	0.35	Uniform	Vertical	H13T1.25	5.7%	61.4%	33.0%	0.1%
7	0.80	0.35	Uniform	Vertical	H13T1.5	4.4%	68.7%	26.9%	0.0%
8	0.80	0.35	Uniform	Vertical	H13T1.5	4.5%	69.3%	26.2%	0.0%
9	0.80	0.35	Uniform	Vertical	H13T2	3.5%	71.4%	25.1%	0.2%
10	0.80	0.35	Uniform	Vertical	H13T2	4.0%	71.3%	24.7%	0.1%

Test	Porosity	Width (m)	Arrangement	Orientation	Wave condition	H_I (m)	H_{R1} (m)	H_T (m)	H_{R2} (m)
1	0.80	0.35	Uniform	Horizontal	H13T1	0.1174	0.0236	0.0726	0.0008
2	0.80	0.35	Uniform	Horizontal	H13T1	0.1186	0.0226	0.0726	0.0008
3	0.80	0.35	Uniform	Horizontal	H13T1.13	0.1224	0.0200	0.0802	0.0018
4	0.80	0.35	Uniform	Horizontal	H13T1.13	0.1222	0.0202	0.0802	0.0018
5	0.80	0.35	Uniform	Horizontal	H13T1.25	0.1230	0.0200	0.0804	0.0018
6	0.80	0.35	Uniform	Horizontal	H13T1.25	0.1218	0.0248	0.0846	0.0032
7	0.80	0.35	Uniform	Horizontal	H13T1.5	0.1216	0.0249	0.0846	0.0030
8	0.80	0.35	Uniform	Horizontal	H13T1.5	0.1212	0.0220	0.0910	0.0004
9	0.80	0.35	Uniform	Horizontal	H13T2	0.1218	0.0220	0.0912	0.0006
10	0.80	0.35	Uniform	Horizontal	H13T2	0.1212	0.0234	0.0964	0.0030
Test	Porosity	Width (m)	Arrangement	Orientation	Wave condition	C_{R1}^2	C_T^2	C_{diss}^2	C_{R2}^2
1	0.80	0.35	Uniform	Horizontal	H13T1	4.0%	38.2%	57.8%	0.0%
2	0.80	0.35	Uniform	Horizontal	H13T1	3.7%	37.5%	58.9%	0.0%
3	0.80	0.35	Uniform	Horizontal	H13T1.13	2.8%	43.1%	54.2%	0.0%
4	0.80	0.35	Uniform	Horizontal	H13T1.13	2.6%	42.7%	54.7%	0.0%
5	0.80	0.35	Uniform	Horizontal	H13T1.25	4.2%	48.2%	47.6%	0.0%
6	0.80	0.35	Uniform	Horizontal	H13T1.25	4.2%	48.4%	47.4%	0.1%
7	0.80	0.35	Uniform	Horizontal	H13T1.5	3.3%	56.4%	40.4%	0.1%
8	0.80	0.35	Uniform	Horizontal	H13T1.5	3.3%	56.1%	40.7%	0.0%
9	0.80	0.35	Uniform	Horizontal	H13T2	3.8%	63.3%	33.0%	0.0%
10	0.80	0.35	Uniform	Horizontal	H13T2	3.4%	63.1%	33.5%	0.1%

Test	Porosity	Width (m)	Arrangement	Orientation	Wave condition	H_I (m)	H_{R1} (m)	H_T (m)	H_{R2} (m)
1	0.94	0.35	Uniform	Vertical	H13T1	0.1148	0.0120	0.1058	0.0028
2	0.94	0.35	Uniform	Vertical	H13T1	0.1148	0.0124	0.1056	0.0032
3	0.94	0.35	Uniform	Vertical	H13T1.13	0.1192	0.0060	0.1098	0.0044
4	0.94	0.35	Uniform	Vertical	H13T1.13	0.1192	0.0064	0.1098	0.0042
5	0.94	0.35	Uniform	Vertical	H13T1.25	0.1208	0.0072	0.1136	0.0028
6	0.94	0.35	Uniform	Vertical	H13T1.25	0.1212	0.0076	0.1124	0.0026
7	0.94	0.35	Uniform	Vertical	H13T1.5	0.1206	0.0066	0.1134	0.0004
8	0.94	0.35	Uniform	Vertical	H13T1.5	0.1206	0.0066	0.1136	0.0004
9	0.94	0.35	Uniform	Vertical	H13T2	0.1202	0.0044	0.1130	0.0064
10	0.94	0.35	Uniform	Vertical	H13T2	0.1202	0.0053	0.1130	0.0052
Test	Porosity	Width (m)	Arrangement	Orientation	Wave condition	C_{R1}^2	C_T^2	C_{diss}^2	C_{R2}^2
1	0.94	0.35	Uniform	Vertical	H13T1	1.1%	84.9%	15.0%	0.1%
2	0.94	0.35	Uniform	Vertical	H13T1	1.2%	84.6%	14.2%	0.1%
3	0.94	0.35	Uniform	Vertical	H13T1.13	0.3%	84.9%	14.9%	0.1%
4	0.94	0.35	Uniform	Vertical	H13T1.13	0.3%	84.9%	14.9%	0.1%
5	0.94	0.35	Uniform	Vertical	H13T1.25	0.4%	85.5%	14.3%	0.1%
6	0.94	0.35	Uniform	Vertical	H13T1.25	0.4%	86.0%	13.6%	0.0%
7	0.94	0.35	Uniform	Vertical	H13T1.5	0.3%	88.4%	11.3%	0.0%
8	0.94	0.35	Uniform	Vertical	H13T1.5	0.3%	88.7%	11.0%	0.0%
9	0.94	0.35	Uniform	Vertical	H13T2	0.1%	88.4%	11.5%	0.3%
10	0.94	0.35	Uniform	Vertical	H13T2	0.2%	88.4%	11.4%	0.2%

Test	Porosity	Width (m)	Arrangement	Orientation	Wave condition	H_I (m)	H_{R1} (m)	H_T (m)	H_{R2} (m)
1	0.94	0.35	Uniform	Horizontal	H13T1	0.1098	0.0052	0.0934	0.0020
2	0.94	0.35	Uniform	Horizontal	H13T1	0.1098	0.0060	0.0942	0.0016
3	0.94	0.35	Uniform	Horizontal	H13T1.13	0.1162	0.0046	0.1018	0.0024
4	0.94	0.35	Uniform	Horizontal	H13T1.13	0.1156	0.0046	0.1018	0.0028
5	0.94	0.35	Uniform	Horizontal	H13T1.25	0.1188	0.0068	0.1066	0.0030
6	0.94	0.35	Uniform	Horizontal	H13T1.25	0.1190	0.0070	0.1066	0.0032
7	0.94	0.35	Uniform	Horizontal	H13T1.5	0.1152	0.0056	0.1070	0.0010
8	0.94	0.35	Uniform	Horizontal	H13T1.5	0.1154	0.0058	0.1072	0.0008
9	0.94	0.35	Uniform	Horizontal	H13T2	0.1184	0.0060	0.1104	0.0050
10	0.94	0.35	Uniform	Horizontal	H13T2	0.1190	0.0062	0.1110	0.0060
Test	Porosity	Width (m)	Arrangement	Orientation	Wave condition	C_{R1}^2	C_T^2	C_{diss}^2	C_{R2}^2
1	0.94	0.35	Uniform	Horizontal	H13T1	0.2%	72.4%	27.4%	0.0%
2	0.94	0.35	Uniform	Horizontal	H13T1	0.3%	73.6%	26.1%	0.0%
3	0.94	0.35	Uniform	Horizontal	H13T1.13	0.2%	76.8%	23.1%	0.0%
4	0.94	0.35	Uniform	Horizontal	H13T1.13	0.2%	77.5%	22.3%	0.1%
5	0.94	0.35	Uniform	Horizontal	H13T1.25	0.3%	80.5%	19.2%	0.1%
6	0.94	0.35	Uniform	Horizontal	H13T1.25	0.4%	80.3%	19.4%	0.1%
7	0.94	0.35	Uniform	Horizontal	H13T1.5	0.2%	86.3%	13.5%	0.0%
8	0.94	0.35	Uniform	Horizontal	H13T1.5	0.3%	86.3%	13.5%	0.0%
9	0.94	0.35	Uniform	Horizontal	H13T2	0.3%	87.0%	12.8%	0.2%
10	0.94	0.35	Uniform	Horizontal	H13T2	0.3%	87.0%	12.7%	0.3%

Test	Porosity	Width (m)	Arrangement	Orientation	Wave condition	H_I (m)	H_{R1} (m)	H_T (m)	H_{R2} (m)
1	0.90	0.35	Long.>lat.	Vertical	H13T1	0.1142	0.0202	0.0966	0.0018
2	0.90	0.35	Long.>lat.	Vertical	H13T1	0.1156	0.0196	0.0973	0.0020
3	0.90	0.35	Long.>lat.	Vertical	H13T1.13	0.1220	0.0152	0.1006	0.0032
4	0.90	0.35	Long.>lat.	Vertical	H13T1.13	0.1218	0.0156	0.1008	0.0030
5	0.90	0.35	Long.>lat.	Vertical	H13T1.25	0.1216	0.0160	0.1028	0.0028
6	0.90	0.35	Long.>lat.	Vertical	H13T1.25	0.1216	0.0162	0.1028	0.0026
7	0.90	0.35	Long.>lat.	Vertical	H13T1.5	0.1212	0.0166	0.1056	0.0002
8	0.90	0.35	Long.>lat.	Vertical	H13T1.5	0.1214	0.0166	0.1054	0.0004
9	0.90	0.35	Long.>lat.	Vertical	H13T2	0.1214	0.0158	0.1058	0.0054
10	0.90	0.35	Long.>lat.	Vertical	H13T2	0.1214	0.0157	0.1058	0.0062
Test	Porosity	Width (m)	Arrangement	Orientation	Wave condition	C_{R1}^2	C_T^2	C_{diss}^2	C_{R2}^2
1	0.90	0.35	Long.>lat.	Vertical	H13T1	3.1%	71.6%	25.3%	0.0%
2	0.90	0.35	Long.>lat.	Vertical	H13T1	2.9%	70.7%	26.5%	0.0%
3	0.90	0.35	Long.>lat.	Vertical	H13T1.13	1.5%	68.0%	30.5%	0.1%
4	0.90	0.35	Long.>lat.	Vertical	H13T1.13	1.6%	68.5%	29.9%	0.1%
5	0.90	0.35	Long.>lat.	Vertical	H13T1.25	1.7%	71.5%	26.8%	0.1%
6	0.90	0.35	Long.>lat.	Vertical	H13T1.25	1.8%	71.5%	26.8%	0.0%
7	0.90	0.35	Long.>lat.	Vertical	H13T1.5	1.9%	75.6%	22.5%	0.0%
8	0.90	0.35	Long.>lat.	Vertical	H13T1.5	1.9%	75.4%	22.8%	0.0%
9	0.90	0.35	Long.>lat.	Vertical	H13T2	1.7%	76.0%	22.3%	0.2%
10	0.90	0.35	Long.>lat.	Vertical	H13T2	1.7%	76.0%	22.4%	0.3%

Test	Porosity	Width (m)	Arrangement	Orientation	Wave condition	H_I (m)	H_{R1} (m)	H_T (m)	H_{R2} (m)
1	0.90	0.35	Long.>lat.	Horizontal	H13T1	0.1178	0.0168	0.0890	0.0008
2	0.90	0.35	Long.>lat.	Horizontal	H13T1	0.1176	0.0168	0.0892	0.0006
3	0.90	0.35	Long.>lat.	Horizontal	H13T1.13	0.1220	0.0152	0.0948	0.0016
4	0.90	0.35	Long.>lat.	Horizontal	H13T1.13	0.1220	0.0152	0.0950	0.0016
5	0.90	0.35	Long.>lat.	Horizontal	H13T1.25	0.1226	0.0184	0.0948	0.0026
6	0.90	0.35	Long.>lat.	Horizontal	H13T1.25	0.1220	0.0182	0.0978	0.0028
7	0.90	0.35	Long.>lat.	Horizontal	H13T1.5	0.1218	0.0152	0.1008	0.0010
8	0.90	0.35	Long.>lat.	Horizontal	H13T1.5	0.1218	0.0156	0.1010	0.0010
9	0.90	0.35	Long.>lat.	Horizontal	H13T2	0.1220	0.0150	0.1036	0.0058
10	0.90	0.35	Long.>lat.	Horizontal	H13T2	0.1216	0.0160	0.1034	0.0048
Test	Porosity	Width (m)	Arrangement	Orientation	Wave condition	C_{R1}^2	C_T^2	C_{diss}^2	C_{R2}^2
1	0.90	0.35	Long.>lat.	Horizontal	H13T1	2.1%	57.1%	40.9%	0.0%
2	0.90	0.35	Long.>lat.	Horizontal	H13T1	2.1%	57.5%	40.4%	0.0%
3	0.90	0.35	Long.>lat.	Horizontal	H13T1.13	1.6%	60.4%	38.1%	0.0%
4	0.90	0.35	Long.>lat.	Horizontal	H13T1.13	1.5%	60.6%	37.8%	0.0%
5	0.90	0.35	Long.>lat.	Horizontal	H13T1.25	2.3%	63.6%	34.1%	0.0%
6	0.90	0.35	Long.>lat.	Horizontal	H13T1.25	2.2%	64.3%	33.5%	0.1%
7	0.90	0.35	Long.>lat.	Horizontal	H13T1.5	1.6%	68.5%	30.0%	0.0%
8	0.90	0.35	Long.>lat.	Horizontal	H13T1.5	1.6%	68.8%	29.6%	0.0%
9	0.90	0.35	Long.>lat.	Horizontal	H13T2	1.5%	72.1%	26.4%	0.2%
10	0.90	0.35	Long.>lat.	Horizontal	H13T2	1.7%	72.3%	26.0%	0.2%

Test	Porosity	Width (m)	Arrangement	Orientation	Wave condition	H_I (m)	H_{R1} (m)	H_T (m)	H_{R2} (m)
1	0.90	0.68	Long.>lat.	Vertical	H13T1	0.1182	0.0104	0.0868	0.0024
2	0.90	0.68	Long.>lat.	Vertical	H13T1	0.1178	0.0108	0.0866	0.0026
3	0.90	0.68	Long.>lat.	Vertical	H13T1.13	0.1220	0.0204	0.0914	0.0026
4	0.90	0.68	Long.>lat.	Vertical	H13T1.13	0.1218	0.0202	0.0910	0.0028
5	0.90	0.68	Long.>lat.	Vertical	H13T1.25	0.1214	0.0149	0.0942	0.0032
6	0.90	0.68	Long.>lat.	Vertical	H13T1.25	0.1214	0.0148	0.0944	0.0032
7	0.90	0.68	Long.>lat.	Vertical	H13T1.5	0.1214	0.0200	0.0980	0.0040
8	0.90	0.68	Long.>lat.	Vertical	H13T1.5	0.1214	0.0198	0.0976	0.0040
9	0.90	0.68	Long.>lat.	Vertical	H13T2	0.1220	0.0212	0.0988	0.0058
10	0.90	0.68	Long.>lat.	Vertical	H13T2	0.1222	0.0214	0.0990	0.0058
Test	Porosity	Width (m)	Arrangement	Orientation	Wave condition	C_{R1}^2	C_T^2	C_{diss}^2	C_{R2}^2
1	0.90	0.68	Long.>lat.	Vertical	H13T1	0.8%	53.9%	45.3%	0.0%
2	0.90	0.68	Long.>lat.	Vertical	H13T1	0.5%	54.0%	45.2%	0.0%
3	0.90	0.68	Long.>lat.	Vertical	H13T1.13	2.8%	56.1%	41.1%	0.0%
4	0.90	0.68	Long.>lat.	Vertical	H13T1.13	2.8%	55.8%	41.4%	0.1%
5	0.90	0.68	Long.>lat.	Vertical	H13T1.25	1.5%	60.2%	38.3%	0.1%
6	0.90	0.68	Long.>lat.	Vertical	H13T1.25	1.5%	60.5%	38.1%	0.1%
7	0.90	0.68	Long.>lat.	Vertical	H13T1.5	2.7%	65.2%	32.2%	0.1%
8	0.90	0.68	Long.>lat.	Vertical	H13T1.5	2.7%	64.6%	32.7%	0.1%
9	0.90	0.68	Long.>lat.	Vertical	H13T2	3.0%	65.6%	31.4%	0.2%
10	0.90	0.68	Long.>lat.	Vertical	H13T2	3.1%	65.6%	31.3%	0.2%

Test	Porosity	Width (m)	Arrangement	Orientation	Wave condition	H_I (m)	H_{R1} (m)	H_T (m)	H_{R2} (m)
1	0.90	0.68	Long.>lat.	Horizontal	H13T1	0.1174	0.0114	0.0762	0.0010
2	0.90	0.68	Long.>lat.	Horizontal	H13T1	0.1182	0.0114	0.0764	0.0008
3	0.90	0.68	Long.>lat.	Horizontal	H13T1.13	0.1226	0.0120	0.0834	0.0024
4	0.90	0.68	Long.>lat.	Horizontal	H13T1.13	0.1206	0.0096	0.0836	0.0026
5	0.90	0.68	Long.>lat.	Horizontal	H13T1.25	0.1226	0.0162	0.0878	0.0102
6	0.90	0.68	Long.>lat.	Horizontal	H13T1.25	0.1224	0.0164	0.0878	0.0102
7	0.90	0.68	Long.>lat.	Horizontal	H13T1.5	0.1218	0.0200	0.0914	0.0004
8	0.90	0.68	Long.>lat.	Horizontal	H13T1.5	0.1218	0.0198	0.0918	0.0006
9	0.90	0.68	Long.>lat.	Horizontal	H13T2	0.1222	0.0210	0.0952	0.0048
10	0.90	0.68	Long.>lat.	Horizontal	H13T2	0.1226	0.0208	0.0958	0.0058
Test	Porosity	Width (m)	Arrangement	Orientation	Wave condition	C_{R1}^2	C_T^2	C_{diss}^2	C_{R2}^2
1	0.90	0.68	Long.>lat.	Horizontal	H13T1	1.0%	42.1%	56.9%	0.0%
2	0.90	0.68	Long.>lat.	Horizontal	H13T1	0.9%	41.8%	57.3%	0.0%
3	0.90	0.68	Long.>lat.	Horizontal	H13T1.13	1.0%	46.3%	52.8%	0.0%
4	0.90	0.68	Long.>lat.	Horizontal	H13T1.13	0.6%	48.1%	51.3%	0.0%
5	0.90	0.68	Long.>lat.	Horizontal	H13T1.25	1.8%	51.3%	47.0%	0.7%
6	0.90	0.68	Long.>lat.	Horizontal	H13T1.25	1.8%	51.5%	46.8%	0.7%
7	0.90	0.68	Long.>lat.	Horizontal	H13T1.5	2.7%	56.3%	41.0%	0.0%
8	0.90	0.68	Long.>lat.	Horizontal	H13T1.5	2.6%	56.8%	40.6%	0.0%
9	0.90	0.68	Long.>lat.	Horizontal	H13T2	2.9%	60.7%	36.4%	0.2%
10	0.90	0.68	Long.>lat.	Horizontal	H13T2	2.9%	61.1%	36.1%	0.2%

Test	Porosity	Width (m)	Arrangement	Orientation	Wave condition	H_I (m)	H_{R1} (m)	H_T (m)	H_{R2} (m)
1	0.90	0.35	Lat.>long.	Vertical	H13T1	0.1144	0.0204	0.1042	0.0032
2	0.90	0.35	Lat.>long.	Vertical	H13T1	0.1138	0.0214	0.1034	0.0036
3	0.90	0.35	Lat.>long.	Vertical	H13T1.13	0.1206	0.0150	0.1076	0.0048
4	0.90	0.35	Lat.>long.	Vertical	H13T1.13	0.1212	0.0154	0.1078	0.0048
5	0.90	0.35	Lat.>long.	Vertical	H13T1.25	0.1230	0.0140	0.1100	0.0040
6	0.90	0.35	Lat.>long.	Vertical	H13T1.25	0.1230	0.0138	0.1100	0.0040
7	0.90	0.35	Lat.>long.	Vertical	H13T1.5	0.1214	0.0114	0.1132	0.0004
8	0.90	0.35	Lat.>long.	Vertical	H13T1.5	0.1216	0.0112	0.1134	0.0004
9	0.90	0.35	Lat.>long.	Vertical	H13T2	0.1212	0.0084	0.1136	0.0062
10	0.90	0.35	Lat.>long.	Vertical	H13T2	0.1212	0.0096	0.1136	0.0046
Test	Porosity	Width (m)	Arrangement	Orientation	Wave condition	C_{R1}^2	C_T^2	C_{diss}^2	C_{R2}^2
1	0.90	0.35	Lat.>long.	Vertical	H13T1	3.2%	83.0%	13.9%	0.1%
2	0.90	0.35	Lat.>long.	Vertical	H13T1	3.5%	82.6%	13.9%	0.1%
3	0.90	0.35	Lat.>long.	Vertical	H13T1.13	1.6%	79.6%	18.9%	0.2%
4	0.90	0.35	Lat.>long.	Vertical	H13T1.13	1.6%	79.1%	19.3%	0.2%
5	0.90	0.35	Lat.>long.	Vertical	H13T1.25	1.3%	80.0%	18.7%	0.1%
6	0.90	0.35	Lat.>long.	Vertical	H13T1.25	1.2%	80.0%	18.8%	0.1%
7	0.90	0.35	Lat.>long.	Vertical	H13T1.5	0.9%	87.0%	12.2%	0.0%
8	0.90	0.35	Lat.>long.	Vertical	H13T1.5	0.9%	87.0%	12.2%	0.0%
9	0.90	0.35	Lat.>long.	Vertical	H13T2	0.5%	87.9%	11.7%	0.3%
10	0.90	0.35	Lat.>long.	Vertical	H13T2	0.6%	87.9%	11.5%	0.1%

Test	Porosity	Width (m)	Arrangement	Orientation	Wave condition	H_I (m)	H_{R1} (m)	H_T (m)	H_{R2} (m)
1	0.90	0.35	Lat.>long.	Horizontal	H13T1	0.1174	0.0118	0.0926	0.0020
2	0.90	0.35	Lat.>long.	Horizontal	H13T1	0.1174	0.0114	0.0928	0.0020
3	0.90	0.35	Lat.>long.	Horizontal	H13T1.13	0.1206	0.0042	0.0947	0.0036
4	0.90	0.35	Lat.>long.	Horizontal	H13T1.13	0.1212	0.0056	0.0976	0.0036
5	0.90	0.35	Lat.>long.	Horizontal	H13T1.25	0.1216	0.0086	0.1022	0.0044
6	0.90	0.35	Lat.>long.	Horizontal	H13T1.25	0.1216	0.0084	0.1022	0.0036
7	0.90	0.35	Lat.>long.	Horizontal	H13T1.5	0.1212	0.0078	0.1090	0.0010
8	0.90	0.35	Lat.>long.	Horizontal	H13T1.5	0.1210	0.0076	0.1088	0.0016
9	0.90	0.35	Lat.>long.	Horizontal	H13T2	0.1210	0.0076	0.1110	0.0060
10	0.90	0.35	Lat.>long.	Horizontal	H13T2	0.1212	0.0072	0.1114	0.0066
Test	Porosity	Width (m)	Arrangement	Orientation	Wave condition	C_{R1}^2	C_T^2	C_{diss}^2	C_{R2}^2
1	0.90	0.35	Lat.>long.	Horizontal	H13T1	1.0%	62.2%	36.8%	0.0%
2	0.90	0.35	Lat.>long.	Horizontal	H13T1	0.9%	62.5%	36.6%	0.0%
3	0.90	0.35	Lat.>long.	Horizontal	H13T1.13	0.1%	65.2%	34.7%	0.1%
4	0.90	0.35	Lat.>long.	Horizontal	H13T1.13	0.2%	64.9%	34.9%	0.1%
5	0.90	0.35	Lat.>long.	Horizontal	H13T1.25	0.5%	70.6%	28.9%	0.1%
6	0.90	0.35	Lat.>long.	Horizontal	H13T1.25	0.5%	70.6%	28.9%	0.1%
7	0.90	0.35	Lat.>long.	Horizontal	H13T1.5	0.4%	80.9%	18.7%	0.0%
8	0.90	0.35	Lat.>long.	Horizontal	H13T1.5	0.4%	80.9%	18.8%	0.0%
9	0.90	0.35	Lat.>long.	Horizontal	H13T2	0.4%	84.2%	15.4%	0.2%
10	0.90	0.35	Lat.>long.	Horizontal	H13T2	0.4%	84.5%	15.2%	0.3%

Test	Porosity	Width (m)	Arrangement	Orientation	Wave condition	H_I (m)	H_{R1} (m)	H_T (m)	H_{R2} (m)
1	0.90	0.68	Lat.>long.	Vertical	H13T1	0.1154	0.0078	0.0970	0.0030
2	0.90	0.68	Lat.>long.	Vertical	H13T1	0.1146	0.0080	0.0968	0.0030
3	0.90	0.68	Lat.>long.	Vertical	H13T1.13	0.1194	0.0104	0.1018	0.0032
4	0.90	0.68	Lat.>long.	Vertical	H13T1.13	0.1196	0.0104	0.1020	0.0030
5	0.90	0.68	Lat.>long.	Vertical	H13T1.25	0.1212	0.0128	0.1046	0.0026
6	0.90	0.68	Lat.>long.	Vertical	H13T1.25	0.1212	0.0128	0.1052	0.0024
7	0.90	0.68	Lat.>long.	Vertical	H13T1.5	0.1196	0.0168	0.1076	0.0012
8	0.90	0.68	Lat.>long.	Vertical	H13T1.5	0.1200	0.0170	0.1082	0.0008
9	0.90	0.68	Lat.>long.	Vertical	H13T2	0.1208	0.0138	0.1094	0.0060
10	0.90	0.68	Lat.>long.	Vertical	H13T2	0.1206	0.0148	0.1090	0.0046
Test	Porosity	Width (m)	Arrangement	Orientation	Wave condition	C_{R1}^2	C_T^2	C_{diss}^2	C_{R2}^2
1	0.90	0.68	Lat.>long.	Vertical	H13T1	0.5%	70.7%	28.9%	0.1%
2	0.90	0.68	Lat.>long.	Vertical	H13T1	0.5%	71.4%	28.2%	0.1%
3	0.90	0.68	Lat.>long.	Vertical	H13T1.13	0.8%	72.7%	26.6%	0.1%
4	0.90	0.68	Lat.>long.	Vertical	H13T1.13	0.8%	72.7%	26.5%	0.1%
5	0.90	0.68	Lat.>long.	Vertical	H13T1.25	1.1%	74.5%	24.4%	0.0%
6	0.90	0.68	Lat.>long.	Vertical	H13T1.25	1.1%	75.3%	23.5%	0.0%
7	0.90	0.68	Lat.>long.	Vertical	H13T1.5	2.0%	80.9%	17.1%	0.0%
8	0.90	0.68	Lat.>long.	Vertical	H13T1.5	2.0%	81.3%	16.7%	0.0%
9	0.90	0.68	Lat.>long.	Vertical	H13T2	1.3%	82.0%	16.7%	0.2%
10	0.90	0.68	Lat.>long.	Vertical	H13T2	1.5%	81.7%	16.8%	0.1%

Test	Porosity	Width (m)	Arrangement	Orientation	Wave condition	H_I (m)	H_{R1} (m)	H_T (m)	H_{R2} (m)
1	0.90	0.68	Lat.>long.	Horizontal	H13T1	0.1178	0.0080	0.0802	0.0010
2	0.90	0.68	Lat.>long.	Horizontal	H13T1	0.1170	0.0088	0.0804	0.0010
3	0.90	0.68	Lat.>long.	Horizontal	H13T1.13	0.1204	0.0038	0.0876	0.0030
4	0.90	0.68	Lat.>long.	Horizontal	H13T1.13	0.1202	0.0046	0.0876	0.0030
5	0.90	0.68	Lat.>long.	Horizontal	H13T1.25	0.1222	0.0092	0.0928	0.0042
6	0.90	0.68	Lat.>long.	Horizontal	H13T1.25	0.1220	0.0092	0.0926	0.0044
7	0.90	0.68	Lat.>long.	Horizontal	H13T1.5	0.1212	0.0106	0.1014	0.0008
8	0.90	0.68	Lat.>long.	Horizontal	H13T1.5	0.1212	0.0108	0.1012	0.0010
9	0.90	0.68	Lat.>long.	Horizontal	H13T2	0.1214	0.0120	0.1068	0.0044
10	0.90	0.68	Lat.>long.	Horizontal	H13T2	0.1212	0.0122	0.1058	0.0042
Test	Porosity	Width (m)	Arrangement	Orientation	Wave condition	C_{R1}^2	C_T^2	C_{diss}^2	C_{R2}^2
1	0.90	0.68	Lat.>long.	Horizontal	H13T1	0.5%	46.4%	53.2%	0.0%
2	0.90	0.68	Lat.>long.	Horizontal	H13T1	0.6%	47.2%	52.2%	0.0%
3	0.90	0.68	Lat.>long.	Horizontal	H13T1.13	0.1%	52.9%	47.0%	0.1%
4	0.90	0.68	Lat.>long.	Horizontal	H13T1.13	0.2%	53.1%	46.7%	0.1%
5	0.90	0.68	Lat.>long.	Horizontal	H13T1.25	0.6%	57.7%	41.8%	0.1%
6	0.90	0.68	Lat.>long.	Horizontal	H13T1.25	0.6%	57.6%	41.8%	0.1%
7	0.90	0.68	Lat.>long.	Horizontal	H13T1.5	0.8%	70.0%	29.2%	0.0%
8	0.90	0.68	Lat.>long.	Horizontal	H13T1.5	0.8%	69.7%	29.5%	0.0%
9	0.90	0.68	Lat.>long.	Horizontal	H13T2	1.0%	76.0%	23.1%	0.1%
10	0.90	0.68	Lat.>long.	Horizontal	H13T2	1.0%	76.2%	22.8%	0.1%

Test	Porosity	Width (m)	Arrangement	Orientation	Wave condition	H_I (m)	H_{R1} (m)	H_T (m)	H_{R2} (m)
1	0.90	0.35	Staggered	Vertical	H13T1	0.1156	0.0188	0.1020	0.0036
2	0.90	0.35	Staggered	Vertical	H13T1	0.1150	0.0198	0.1022	0.0032
3	0.90	0.35	Staggered	Vertical	H13T1.13	0.1226	0.0164	0.1056	0.0042
4	0.90	0.35	Staggered	Vertical	H13T1.13	0.1224	0.0162	0.1058	0.0042
5	0.90	0.35	Staggered	Vertical	H13T1.25	0.1230	0.0112	0.1080	0.0036
6	0.90	0.35	Staggered	Vertical	H13T1.25	0.1232	0.0118	0.1084	0.0032
7	0.90	0.35	Staggered	Vertical	H13T1.5	0.1222	0.0110	0.1104	0.0002
8	0.90	0.35	Staggered	Vertical	H13T1.5	0.1225	0.0114	0.1106	0.0002
9	0.90	0.35	Staggered	Vertical	H13T2	0.1206	0.0100	0.1090	0.0068
10	0.90	0.35	Staggered	Vertical	H13T2	0.1212	0.0112	0.1094	0.0046
Test	Porosity	Width (m)	Arrangement	Orientation	Wave condition	C_{R1}^2	C_T^2	C_{diss}^2	C_{R2}^2
1	0.90	0.35	Staggered	Vertical	H13T1	2.7%	77.9%	19.5%	0.1%
2	0.90	0.35	Staggered	Vertical	H13T1	2.9%	79.0%	18.1%	0.1%
3	0.90	0.35	Staggered	Vertical	H13T1.13	1.8%	74.2%	24.0%	0.1%
4	0.90	0.35	Staggered	Vertical	H13T1.13	1.8%	74.7%	23.5%	0.1%
5	0.90	0.35	Staggered	Vertical	H13T1.25	0.8%	77.1%	22.1%	0.1%
6	0.90	0.35	Staggered	Vertical	H13T1.25	0.9%	77.4%	21.7%	0.1%
7	0.90	0.35	Staggered	Vertical	H13T1.5	0.8%	81.6%	17.6%	0.0%
8	0.90	0.35	Staggered	Vertical	H13T1.5	0.9%	81.7%	17.5%	0.0%
9	0.90	0.35	Staggered	Vertical	H13T2	0.7%	81.7%	17.6%	0.3%
10	0.90	0.35	Staggered	Vertical	H13T2	0.8%	81.5%	17.7%	0.1%

Test	Porosity	Width (m)	Arrangement	Orientation	Wave condition	H_I (m)	H_{R1} (m)	H_T (m)	H_{R2} (m)
1	0.90	0.35	Staggered	Horizontal	H13T1	0.1172	0.0142	0.0902	0.0012
2	0.90	0.35	Staggered	Horizontal	H13T1	0.1174	0.0138	0.0904	0.0012
3	0.90	0.35	Staggered	Horizontal	H13T1.13	0.1206	0.0102	0.0960	0.0034
4	0.90	0.35	Staggered	Horizontal	H13T1.13	0.1208	0.0104	0.0958	0.0036
5	0.90	0.35	Staggered	Horizontal	H13T1.25	0.1210	0.0116	0.1102	0.0020
6	0.90	0.35	Staggered	Horizontal	H13T1.25	0.1216	0.0112	0.1000	0.0024
7	0.90	0.35	Staggered	Horizontal	H13T1.5	0.1214	0.0110	0.1050	0.0006
8	0.90	0.35	Staggered	Horizontal	H13T1.5	0.1216	0.0110	0.1050	0.0006
9	0.90	0.35	Staggered	Horizontal	H13T2	0.1222	0.0120	0.1078	0.0046
10	0.90	0.35	Staggered	Horizontal	H13T2	0.1224	0.0112	0.1080	0.0058
Test	Porosity	Width (m)	Arrangement	Orientation	Wave condition	C_{R1}^2	C_T^2	C_{diss}^2	C_{R2}^2
1	0.90	0.35	Staggered	Horizontal	H13T1	1.5%	59.2%	39.3%	0.0%
2	0.90	0.35	Staggered	Horizontal	H13T1	1.4%	59.3%	39.3%	0.0%
3	0.90	0.35	Staggered	Horizontal	H13T1.13	0.7%	63.4%	35.9%	0.1%
4	0.90	0.35	Staggered	Horizontal	H13T1.13	0.7%	62.9%	36.4%	0.1%
5	0.90	0.35	Staggered	Horizontal	H13T1.25	0.9%	68.6%	30.5%	0.0%
6	0.90	0.35	Staggered	Horizontal	H13T1.25	0.9%	67.6%	31.5%	0.0%
7	0.90	0.35	Staggered	Horizontal	H13T1.5	0.8%	74.8%	24.4%	0.0%
8	0.90	0.35	Staggered	Horizontal	H13T1.5	0.8%	74.6%	24.6%	0.0%
9	0.90	0.35	Staggered	Horizontal	H13T2	1.0%	77.8%	21.2%	0.1%
10	0.90	0.35	Staggered	Horizontal	H13T2	0.8%	77.9%	21.3%	0.2%

Test	Porosity	Width (m)	Arrangement	Orientation	Wave condition	H_I (m)	H_{R1} (m)	H_T (m)	H_{R2} (m)
1	0.90	0.68	Staggered	Vertical	H13T1	0.1160	0.0096	0.0938	0.0034
2	0.90	0.68	Staggered	Vertical	H13T1	0.1160	0.0096	0.0934	0.0036
3	0.90	0.68	Staggered	Vertical	H13T1.13	0.1212	0.0118	0.0988	0.0038
4	0.90	0.68	Staggered	Vertical	H13T1.13	0.1214	0.0118	0.0988	0.0036
5	0.90	0.68	Staggered	Vertical	H13T1.25	0.1230	0.0124	0.1016	0.0034
6	0.90	0.68	Staggered	Vertical	H13T1.25	0.1226	0.0124	0.1014	0.0032
7	0.90	0.68	Staggered	Vertical	H13T1.5	0.1218	0.0170	0.1046	0.0004
8	0.90	0.68	Staggered	Vertical	H13T1.5	0.1214	0.0166	0.1044	0.0012
9	0.90	0.68	Staggered	Vertical	H13T2	0.1218	0.0172	0.1042	0.0036
10	0.90	0.68	Staggered	Vertical	H13T2	0.1224	0.0168	0.1048	0.0058
Test	Porosity	Width (m)	Arrangement	Orientation	Wave condition	C_{R1}^2	C_T^2	C_{diss}^2	C_{R2}^2
1	0.90	0.68	Staggered	Vertical	H13T1	0.7%	65.4%	33.9%	0.1%
2	0.90	0.68	Staggered	Vertical	H13T1	0.7%	65.8%	34.5%	0.1%
3	0.90	0.68	Staggered	Vertical	H13T1.13	1.0%	66.5%	32.6%	0.1%
4	0.90	0.68	Staggered	Vertical	H13T1.13	0.9%	66.2%	32.9%	0.1%
5	0.90	0.68	Staggered	Vertical	H13T1.25	1.0%	68.2%	30.7%	0.1%
6	0.90	0.68	Staggered	Vertical	H13T1.25	1.0%	68.4%	30.6%	0.1%
7	0.90	0.68	Staggered	Vertical	H13T1.5	1.9%	73.8%	24.3%	0.0%
8	0.90	0.68	Staggered	Vertical	H13T1.5	1.9%	74.0%	24.2%	0.0%
9	0.90	0.68	Staggered	Vertical	H13T2	2.0%	73.2%	24.8%	0.1%
10	0.90	0.68	Staggered	Vertical	H13T2	1.9%	73.3%	24.8%	0.2%

Test	Porosity	Width (m)	Arrangement	Orientation	Wave condition	H_I (m)	H_{R1} (m)	H_T (m)	H_{R2} (m)
1	0.90	0.68	Staggered	Horizontal	H13T1	0.1174	0.0108	0.0788	0.0014
2	0.90	0.68	Staggered	Horizontal	H13T1	0.1180	0.0098	0.0790	0.0012
3	0.90	0.68	Staggered	Horizontal	H13T1.13	0.1216	0.0098	0.0862	0.0032
4	0.90	0.68	Staggered	Horizontal	H13T1.13	0.1218	0.0096	0.0864	0.0030
5	0.90	0.68	Staggered	Horizontal	H13T1.25	0.1232	0.0116	0.0912	0.0026
6	0.90	0.68	Staggered	Horizontal	H13T1.25	0.1230	0.0116	0.0908	0.0024
7	0.90	0.68	Staggered	Horizontal	H13T1.5	0.1218	0.0144	0.0972	0.0008
8	0.90	0.68	Staggered	Horizontal	H13T1.5	0.1218	0.0142	0.0972	0.0006
9	0.90	0.68	Staggered	Horizontal	H13T2	0.1218	0.0158	0.1008	0.0046
10	0.90	0.68	Staggered	Horizontal	H13T2	0.1220	0.0158	0.1010	0.0048
Test	Porosity	Width (m)	Arrangement	Orientation	Wave condition	C_{R1}^2	C_T^2	C_{diss}^2	C_{R2}^2
1	0.90	0.68	Staggered	Horizontal	H13T1	0.8%	45.1%	54.1%	0.0%
2	0.90	0.68	Staggered	Horizontal	H13T1	0.7%	44.8%	54.5%	0.0%
3	0.90	0.68	Staggered	Horizontal	H13T1.13	0.7%	50.3%	49.1%	0.1%
4	0.90	0.68	Staggered	Horizontal	H13T1.13	0.6%	50.3%	49.1%	0.1%
5	0.90	0.68	Staggered	Horizontal	H13T1.25	0.9%	54.8%	44.3%	0.0%
6	0.90	0.68	Staggered	Horizontal	H13T1.25	0.9%	54.5%	44.6%	0.0%
7	0.90	0.68	Staggered	Horizontal	H13T1.5	1.4%	63.7%	34.9%	0.0%
8	0.90	0.68	Staggered	Horizontal	H13T1.5	1.4%	63.7%	34.9%	0.0%
9	0.90	0.68	Staggered	Horizontal	H13T2	1.7%	68.5%	29.8%	0.1%
10	0.90	0.68	Staggered	Horizontal	H13T2	1.7%	68.5%	29.8%	0.2%

Appendix F: Results correlation wave dissipation and dimensionless wave parameters

The results of the correlation between the wave dissipation and the wave parameters are shown for each effect in Figures F1-F4. Each of the effects is looked at for both the vertical (shown left) and horizontal orientation (shown right).

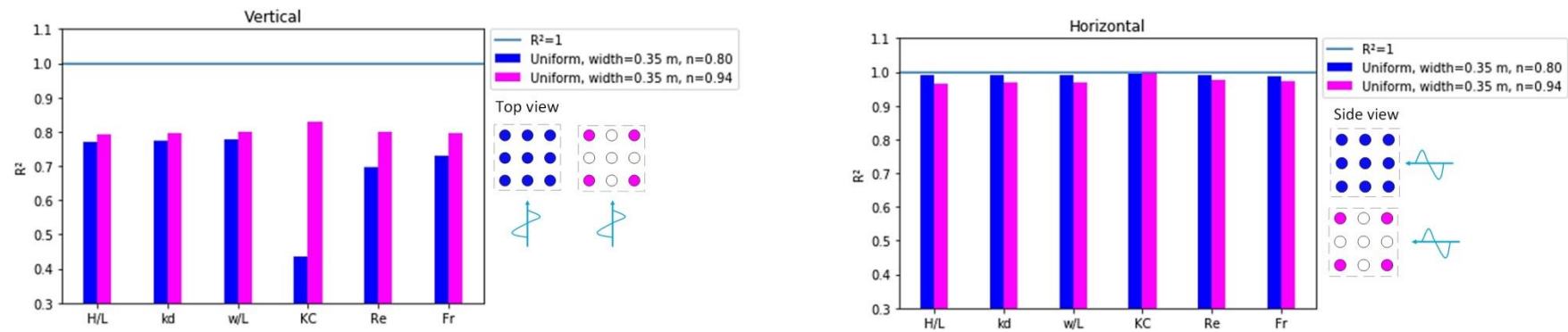


Figure F1 Porosity effect

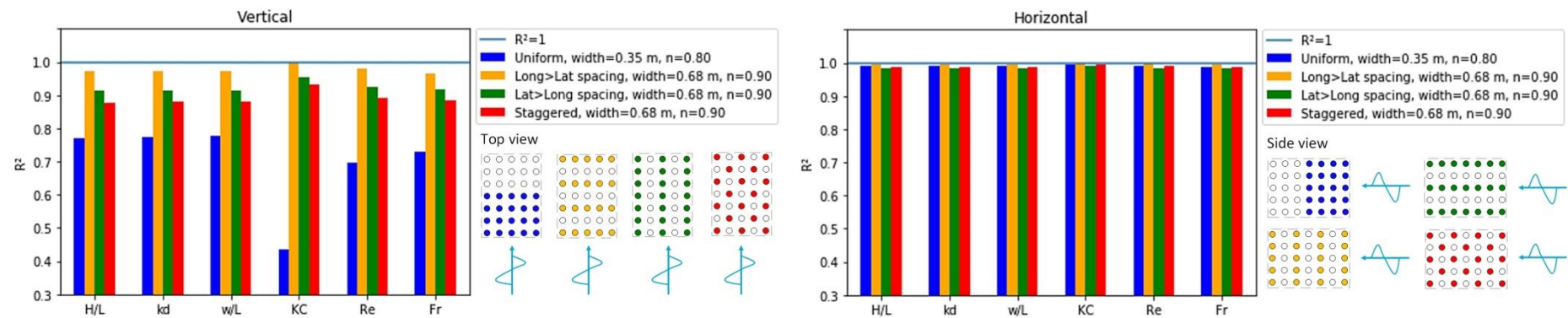


Figure F2 Effect of spreading out the elements

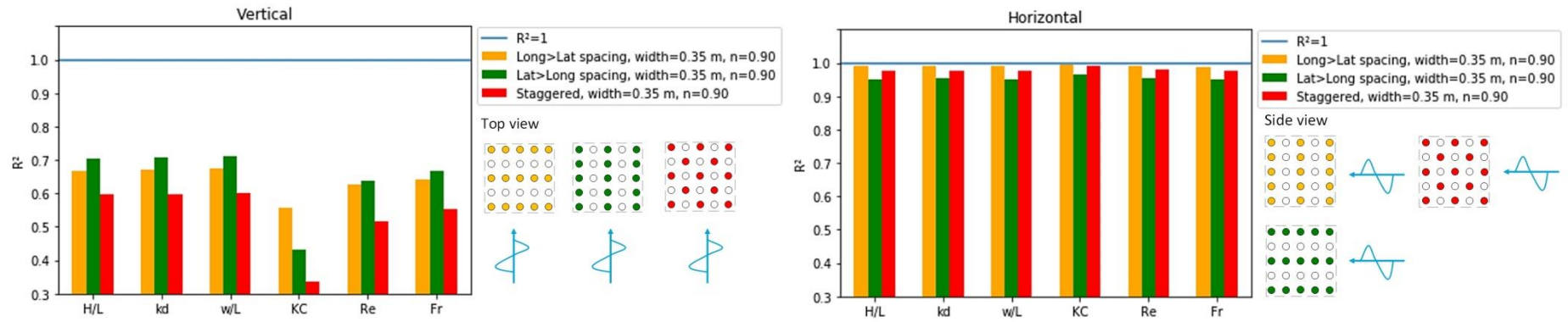


Figure F3 Effect of arrangement for width=0.35 m

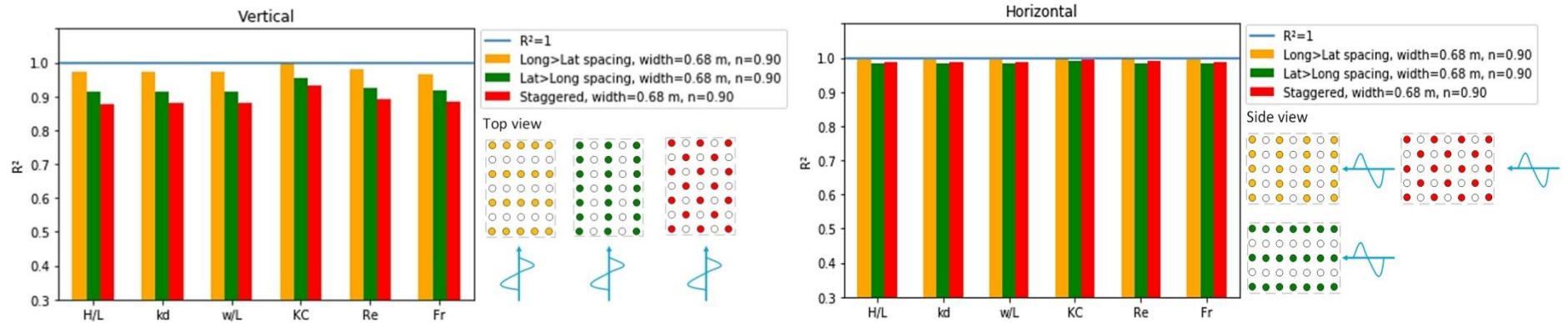


Figure F4 Effect of arrangement for width=0.68 m

